Surface Registration and Indexing for Brain Morphometry Analysis with Conformal Geometry

by

Jie Shi

A Dissertation Presented in Partial Fulfillment
of the Requirements for the Degree
Doctor of Philosophy

Approved April 2016 by the
Graduate Supervisory Committee:

Yalin Wang, Chair
Richard Caselli
Guoliang Xue
Baoxin Li

ARIZONA STATE UNIVERSITY

May 2016

ABSTRACT

In brain imaging study, 3D surface-based algorithms may provide more advantages over volume-based methods, due to their sub-voxel accuracy to represent subtle subregional changes and solid mathematical foundations on which global shape analyses can be achieved on complicated topological structures, such as the convoluted cortical surfaces. On the other hand, given the enormous amount of data being generated daily, it is still challenging to develop effective and efficient surface-based methods to analyze brain shape morphometry. There are two major problems in surface-based shape analysis research: correspondence and similarity. This dissertation covers both topics by proposing novel surface registration and indexing algorithms based on conformal geometry for brain morphometry analysis.

First, I propose a surface fluid registration system, which extends the traditional image fluid registration to surfaces. With surface conformal parameterization, the complexity of the proposed registration formula has been greatly reduced, compared to prior methods. Inverse consistency is also incorporated to drive a symmetric correspondence between surfaces. After registration, the multivariate tensor-based morphometry (mTBM) is computed to measure local shape deformations. The algorithm was applied to study hippocampal atrophy associated with Alzheimer's disease (AD).

Next, I propose a ventricular surface registration algorithm based on hyperbolic Ricci flow, which computes a global conformal parameterization for each ventricular surface without introducing any singularity. Furthermore, in the parameter space, unique hyperbolic geodesic curves are introduced to guide consistent correspondences across subjects, a technique called geodesic curve lifting. Tensor-based morphometry (TBM) statistic is computed from the registration to measure shape changes. This algorithm was applied to study ventricular enlargement in mild cognitive impatient (MCI) converters.

Finally, a new shape index, the hyperbolic Wasserstein distance, is introduced. This algorithm computes the Wasserstein distance between general topological surfaces as a shape similarity measure of different surfaces. It is based on hyperbolic Ricci flow, hyperbolic harmonic map, and optimal mass transportation map, which is extended to hyperbolic space. This method fills a gap in the Wasserstein distance study, where prior work only dealt with images or genus-0 closed surfaces. The algorithm was applied in an AD vs. control cortical shape classification study and achieved promising accuracy rate.

DEDICATION

TO MY FAMILY

ACKNOWLEDGMENTS

First of all, I would like to express my deepest gratitude to my PhD dissertation advisor, Dr. Yalin Wang. Dr. Wang is an expert in geometric modeling, human brain mapping and statistical shape analysis. He is very creative in generating novel ideas and is quite experienced in experimental details as well. Without his guidance and support, I would not be able to accomplish the exciting research achievements and my degree here in Arizona State University. Furthermore, his enthusiasm for work, meticulous attitude for research, and great patience for teaching students have established a good model for my future career development.

I would like to thank Dr. Richard J. Caselli, Dr. Baoxin Li, and Dr. Guoliang Xue to serve on my dissertation committee. Their suggestions have greatly improved the quality of this thesis. I also thank Dr. Paul M. Thompson and Dr. Natasha Leporé of University of Southern California, Dr. Kewei Chen of Banner Alzheimer's Institute and Banner Good Samaritan PET center, and Dr. Leslie C. Baxter of Barrow Neurological Institute for instructions and suggestions on experiments and paper writings.

I would like to thank all the members of our Geometric Systems Laboratory. I thank Duyan Ta, Wen Zhang, NUR SHAZWANI KAMARUDIN, Yonghui Fan, Bolun Li, Liang Xu, and Xing Gao for kindness and friendship. The experience of studying and working with them will be a precious memory of all my life.

Last but not least, I am very grateful to my family for their love and encouragement.

TABLE OF CONTENTS

Page

CHAPTER

CHAPTER Page

APPENDIX

LIST OF TABLES

LIST OF FIGURES

Figure Page

Figure Page

Figure Page

CHAPTER 1

INTRODUCTION

1.1 Surface Registration

Surface registration is the process to find an optimal and meaningful correspondence between two surfaces. It has extensive applications in computer vision [1] and medical imaging [2, 3]. Given two 3D surfaces S_1 and S_2, which are represented as point clouds or triangular meshes, surface registration tries to find a map f between them, such that $f(S_1) = S_2$, and provides both global and local information for shape comparisons. The surface S_1 is usually called the source or deforming surface and S_2 the target or template surface. Surface-based shape analysis usually pursues a diffeomorphic, i.e., smooth and one-to-one, map between two surfaces which are homotopic to each other under certain constraints such as landmark curve matching [4, 5].

Many surface registration algorithms have been proposed, as summarized in [6, 7]. The iterative closest point (ICP) method [8, 9] is based on minimizing the difference between two clouds of points. At the beginning, an initial estimation of the transformation to align the two surfaces is computed. Then the initial mapping is refined to best match the source surface to the target surface. In each iteration, the initial mapping is updated to the refined registration and used as the initial mapping for the next iteration, until the two surfaces are close enough to each other given a predefined measure of similarity. The ICP method can be used to register surfaces that are related by rigid transformations [10] or non-rigid deformations [11, 12]. However, the diffeomorphism of the resulting registration is not guaranteed and a good estimation of the initial mapping is usually required to succeed with the ICP method. Another kind of methods start with a sparse set of point correspondences and then extend them to obtain dense point-to-point mappings between the surfaces [13-16]. Due to the discrete property of the sparse point mappings, these methods often require the preservation of certain measures between two sets of points, such as geodesic distance [13] or spectral quantities [15, 17, 18], etc., to enforce the consistent global alignment. The large deformation diffeomorphic metric mapping (LDDMM) [19] implements the surface registration by controlling the diffeomorphism group and deformation shape spaces to obtain an optimal correspondence between surfaces. This method has been widely applied in brain imaging field [20, 21]. Another type of methods starts by embedding the 3D surfaces to a higher spectral space [17, 22, 23], which is usually spanned by the eigen-system, i.e., eigenvalues and eigen-functions, of the Laplace-Beltrami operator. The registration of surfaces is then obtained by directly warping the higher-dimensional embeddings with rigid or non-rigid transformations to minimize the distance between surfaces, or by gradually changing the metric on the original surfaces to minimize the differences between the embeddings. The resulting surface registration of the latter optimization method is conformal [24].

Recently, based on the development of various surface parameterization methods [25, 26], surface registration can also be done by first mapping the surfaces to be matched onto a canonical parameter space, such as a unit sphere [26], a planar rectangle [27, 28], or a 2D hyperbolic disk [1], and then registering them in the simpler parameter domain. The correspondence field computed in the parameter domain also induces a registration of the original 3D surfaces [29, 30]. The surface registration algorithms that will be presented in this dissertation is based on this framework, as illustrated in figure 1.1. Given two 3D homotopic surfaces S_1 and S_2, their parameterizations to a canonical space are computed by the maps ϕ_1 and ϕ_2, respectively. Then a mapping $\bar{f}$ is computed to match the surfaces in the parameter domain, which also induces the correpondence f between the original surfaces, with $f = \phi_2^{-1} \circ \bar{f} \circ \phi_1 : S_1 \to S_2$. Specifially, the parameterizations ϕ_1, ϕ_2 are conformal maps, as will be introduced in Sec. 1.4.

$$\begin{tikzcd}
\boxed{S_1} \arrow[r, "f"] \arrow[d, "\phi_1"'] & \boxed{S_2} \arrow[d, "\phi_2"] \\
\boxed{\phi_1(S_1)} \arrow[r, "\bar{f}"] & \boxed{\phi_2(S_2)}
\end{tikzcd}$$

Figure 1.1. The surface registration framework used in this dissertation.

1.2 Shape Indexing

With the rapid development of 3D imaging and scanning techniques, 3D surface-based representations of real-life objects are becoming more popular. Many databases of 3D geometric models are emerging and expanding daily. Thus effective algorithms to store, classify, and retrieve the 3D models are highly demanded. Briefly speaking, shape indexing refers to the process to extract concise, refined, and meaningful shape descriptors from the

3D models to represent the geometric or topological features that are able to accurately describe the similarities and dissimilarities between different shapes.

Many shape indexing algorithms have been proposed and applied [31]. Given a function f defined on the sphere $\mathbb{S}^2$, if $f: \mathbb{S}^2 \to R$ is an eigen-function of the Laplace-Beltrami operator on $\mathbb{S}^2$, then f is a spherical harmonic. For any function defined on a surface that can be mapped to a sphere, its expansion in terms of the spherical harmonics is invariant under rotation [25]. Thus, spherical harmonics are widely used to compare and match surfaces that are homotopic to spheres [32, 33]. The heat kernel signature (HKS) describes each surface point's local and global geometric information using heat diffusion method [34]. The HKS is invariant to isometric transformations and has extensive applications in shape classification [35], matching [34], and retrieval [36]. The medial representations or m-reps [37] of surfaces encode rich information about local shape variants and are used in many shape analysis applications [38, 39].

Some shape indexing methods are related to surface conformal geometry [40]. The Gauss–Codazzi equations proved that, conformal factor and mean curvature together can uniquely determine a surface in $\mathbb{R}^3$, up to a rigid motion [41]. They are called the conformal representation of a surface and contain both intrinsic (conformal factor) and extrinsic (mean curvature) information and are invariant to rigid motions. The conformal representation will be used as automatically identified surface features and be matched across subjects in one of the proposed surface registration algorithms (Sec. 2.2.3). The histogram of the conformal factors was used in [42] to characterize different shapes and it is invariant to both rigid motions and pose changes. If two surfaces can be conformally mapped to each other, then they are conformal equivalent and share the same coordinate in the Teichmüller shape space [43]. Shape indices based on Teichmüller space coordinates are invariant to conformal mappings and have been widely applied in computer vision [1] and brain imaging [44-46] research.

Recently, the Wasserstein space, which is the space consists of all probability measures that are defined on a Riemannian manifold, is attracting more attention. It is an important part in the shape space theory [47]. The Wasserstein distance defines a Riemannian metric for the Wasserstein space and can intrinsically measure the similarities between different shapes. However, most existing Wasserstein distance computation algorithms only work with 2D images [48, 49]. Wasserstein distance on 3D surfaces is limited to genus-0 closed surfaces [50],

1.3 Surface-based Brain Morphometry Analysis

In brain imaging research, structural magnetic resonance imaging (MRI) plays an important role in studying brain shape morphometry in normal aging and neurodegenerative diseases. Most brain MRI scanning protocols have been designed to acquire volumetric data on the anatomy of a subject. To statistically compare or combine image data obtained from different people, or at different time-points, various non-linear brain volume-based registration methods [51-53] have been developed for brain image analysis. However, when registering structural MR images, the volume-based methods have much more difficulty with the highly convoluted cortical surfaces due to the complexity and variability of the sulci and gyri. Early research [26, 28, 54, 55] has demonstrated that surface-based brain mapping may offer advantages over volume-based brain mapping as a method to study the structural features of the brain, such as cortical gray matter thickness, as well as the complexity and change patterns in the brain due to disease or developmental processes. The surface registration framework in figure 1.1 can be easily applied to brain surfaces by first parameterizing them to spheres [26, 56, 57] or planar domain [28, 58, 59]. A flow, computed in the parameter domain, induces a correspondence field in 3D brain surfaces [29, 30]. This flow can be constrained using anatomic landmark points or curves [60-62], by subregions of interest [63], by constraining the mapping of surface regions represented implicitly using level sets [59], or by using currents to represent anatomical variation [19, 20, 64]. Feature correspondence between two surfaces can be optimized by using the ℓ_2-norm to measure differences in curvature profiles or convexity [26] or by using mutual information to align scalar fields of various differential geometric parameters defined on the surface [65]. Artificial neural networks may also be used to rule out or favor certain types of feature matches [66]. Finally, correspondences may be determined by using a minimum description length (MDL) principle, based on the compactness of the covariance of the resulting shape model [67, 68]. After surface registration, the brain shape morphometry can be statisically analyzed with surface deformation meausres [32, 69, 70].

The various shape indexing algorithms have also been applied to analyze brain shape morphometry. For example, in [38], the m-rep has been used to study hippocampal shape variability in a population of schizophrenia patients. By parameterizing a cortical surface to a sphere, the spherical harmonics can be applied for surface smoothing, matching, and comparison [32]. With conformal parameterization, conformal-invariant shape indices can also be defined on brain surfaces. Conformal invariants are able to quantitatively measure local and global shape changes and may provide a powerful tool for brain morphometry analysis [44-46]. In [50], the Wasserstein distance was computed on cortical surfaces, by using the conformal spherical domain [25] as a canonical space. The Wasserstein distance was applied in cortical shape classification and experimental results demonstrated its potential to be a brain shape index.

1.4 Brain Surface Parameterization

As discussed above, parameterization of brain surfaces to a canonical space is a fundamental problem for surface-based morphometry study. Sometimes, it is also called brain surface flattening. The goal of surface parameterization is to find some mappings between brain surfaces and some common flattened surfaces, that it, some surfaces with constant Gaussian curvature, such as a sphere [26, 56, 57] with positive Gaussian curvature, a Euclidean plane [28, 58, 59] with zero Guassian curvature, or the hyperbolic space [1] with negave Gaussian curvature. Brain surface parameterization has been studied extensively. A good surface parameterization preserves the geometric features and facilitates the following registration process between surfaces. Some research focus on isometry-based algorithms. An isometric mapping between two surfaces requires that their first fundamental forms be equivalent. However, it is impossible to compute a mapping from an irregular and complicated brain surface to regular canonical space that preserves all the distances. As proved by the theorema egregium [71], brain surfaces usually have variant Gaussian curvature on most of its surface areas, while the canonical surface has constant Gaussian curvature everywhere, these two surfaces cannot be isometric. Therefore, many isometry-based algorithms try to compute the quasi-isometric parameterization, i.e., an approximation of the isometric mapping [72-74]. Area-preserving mappings were also introduced and applied to brain surface parameterization [75, 76]. Another branch of research used concepts from conformal geometry to compute brain surface conformal parameterization [77, 78]. In addition to the angle-preserving property, conformal parameterization provides a rigorous framework for representing, splitting, matching, and measuring brain surface deformations. Particularly, conformal mappings have an appealing property for surface registration. As shown in figure 1.1, let ϕ_1 and ϕ_2 be conformal mappings, then if $\bar{f}$ is conformal, so is f; if $\bar{f}$ is diffeomorphic, so is f [1]. Thus, surface conformal parameterization methods have been extensively applied and validated in the registration problem of brain surfaces [2, 25, 27, 79, 80]. Furthermore, as discussed above, many useful shape indices, such as conformal factor [42], mean curvature, and conformal invariants [45], can also be computed from surface conformal structure.

Another advantage of conformal parameterization is its generality. All oriented surfaces have conformal structures. The uniformization theorem states that all surfaces can be conformally mapped to one of three canonical spaces: the unit sphere $\mathbb{S}^2$, the Euclidean plane $\mathbb{E}^2$, and the hyperbolic space $\mathbb{H}^2$. For a closed genus-0 surface, the spherical conformal mapping method [25] can conformally map it to a sphere by minimizing the harmonic energy, as shown in figure 1.2 (a). For brain surface analysis, landmarks curves are usually introduced to annotate important anatomical or functional regions. After slicing the surfaces open along these landmark curves, they become genus-0 surfaces with multiple open boundaries. The Euclidean Ricci flow [2] method or holomorphic 1-form [80] method can conformally map them to the Euclidean plane, as shown in figure 1.2 (b) and (c), respectively. Their conformal parameterization can also be computed under the hyperbolic geometry [4, 5, 81], as shown in figure 1.2 (d). These conformal parameterization methods are technically sound and numerically stable. They may increase computational accuracy and efficiency when solving the partial differential equations on surfaces. In this dissertation, surface conformal parameterization is chosen to solve the registration and indexing problems of brain surfaces.

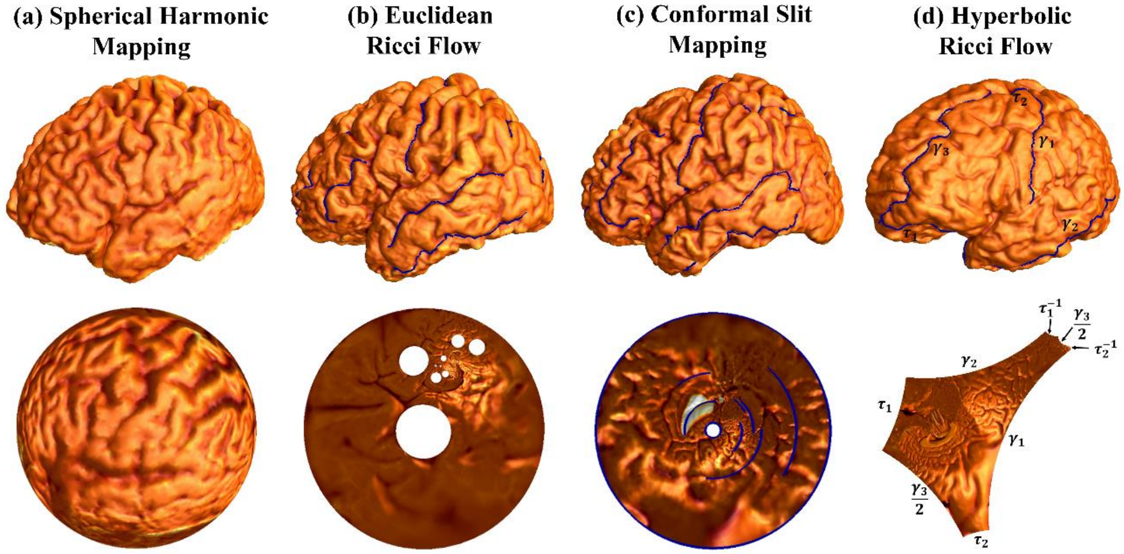

Figure 1.2. Illustration of different brain surface conformal parameterization methods. (a) is the spherical harmonic mapping for closed genus-0 surfaces [25]; for genus-0 surfaces with multiple boundaries, their conformal parameterization can be computed by the Euclidean Ricci flow (b) [2], the holomorphic 1-form method (c) [80], or the hyperbolic Ricci flow (d) [81].

1.5 Organization of the Dissertation

This dissertation will introduce three new surface-based shape analysis algorithms for brain imaging study, including two surface registration methods and one shape indexing method. The proposed methods are based on surface conformal geometry, thus they are stable, efficient, and general. Applications of these algorithms to study brain shape morphometry in Alzheimer's disease (AD) will also be described.

In Chapter 2, a surface fluid registration algorithm will be introduced, which is based on surface conformal parameterization with holomorphic 1-forms [27], inverse consistent surface fluid registration, and multivariate tensor-based morphometry (mTBM) [69, 82]. Traditional image fluid registration algorithm [83] is extended to 3D surfaces. By utilizing conformal parameterization, the complexity of the resulting registration formula is greatly reduced, when compared with prior work [28]. The algorithm was applied on the Alzheimer's Disease Neuroimaging Initiative (ADNI) baseline dataset to study atrophy in hippocampal surfaces that is associated with AD. The proposed method successfully detected significant difference between different diagnostic groups (AD, MCI, and control) and outperformed other two publically available subcortical shape analysis tools. The genetic influence of the Apolipoprotein E $\epsilon 4$ allele (ApoE4) on hippocampal shape morphometry was also studied. The proposed method successfully detected statistically significant difference in hippocampal shape between ApoE4 carriers and noncarriers in both MCI patients and healthy control subjects.

In Chapter 3, a ventricular surface registration algorithm will be introduced, which is based on hyperbolic Ricci flow [1] and tensor-based morphometry (TBM) [32]. Lateral ventricle is a fluid-filled structure deep in human brain, which is usually abnormally enlarged in neurodegenerative diseases. Ventricular enlargement often reflects atrophy of surrounding brain tissues and may give indirect information about brain morphometry in normal aging and cognitive diseases [84-86]. However, surface-based ventricular morphometry analysis is challenging. The surface registration framework in figure 1.1 is not easily applicable to ventricular surfaces. Due to its branchy and complicated topology, it is difficult to find a global parameterization of a ventricular surface without introducing distortions or singularity points. The proposed algorithm computes the ventricular surface conformal parameterization with hyperbolic Ricci flow [1]. The resulting parameterization has minimal angle distortion and no singularities. With geodesic curve lifting, a diffeomorphic registration with consistent boundary conditions is computed between different ventricular surfaces. Then the TBM statistic [32] is computed from the registration to measure surface deformations. The algorithm was applied on MRI scans of two groups of MCI patients from the ADNI baseline dataset, with one group of MCI converters and one group of MCI non-converters. The proposed method detected significant difference in ventricular shapes between the two groups. The correlations between ventricular morphometry, neuropsychological measures, and a previously introduced brain functional index [87], were also analyzed, as both a validation of the correctness of the proposed method and an exploration of the relationship between brain structural and functional changes.

In Chapter 4, a novel shape index, the hyperbolic Wasserstein distance, will be introduced. Unlike prior studies [48-50], the proposed method computes the Wasserstein distance between general surfaces with hyperbolic Ricci flow [1], hyperbolic harmonic map [4], TBM statistic [32], and optimal mass transportation map [88, 89], which is extended to the hyperbolic space. The proposed hyperbolic Wasserstein distance was applied to study cortical shape morphometry with data from the ADNI baseline dataset and achieved a higher rate in the AD vs. control classification study, when compared with other standard brain shape measures.

In Chapter 5, the proposed algorithms and their applications in this dissertation are summarized.

CHAPTER 2

SURFACE FLUID REGISTRATION

This chapter presents a new automated surface registration algorithm based on surface conformal parameterization with holomorphic 1-forms, inverse consistent surface fluid registration, and multivariate tensor-based morphometry (mTBM). First, a surface is conformally mapped onto a planar rectangle with holomorphic 1-forms. Second, the conformal representation of the surface is computed by combining its local conformal factor and mean curvature. Then the dynamic range of the conformal representation is linearly scaled to form the feature image of the surface. Third, the feature image is matched to a chosen template image via the fluid image registration algorithm, which has been extended into the curvilinear coordinates to adjust for the distortion introduced by surface parameterization. The inverse consistent image registration algorithm is also incorporated to jointly estimate the forward and inverse transformations between the study and template images. This alignment induces a corresponding deformation on the surface. The algorithm was tested on the Alzheimer's Disease Neuroimaging Initiative (ADNI) baseline dataset to study AD symptoms on hippocampus. By modeling the hippocampus as a 3D parametric surface, we nonlinearly registered each surface with a selected template surface. Then mTBM was used to analyze the morphometry difference between diagnostic groups. Experimental results show that the new method has better performance than two publically available subcortical surface registration tools: FIRST and SPHARM. The genetic influence of the Apolipoprotein E $\epsilon 4$ allele (ApoE4), which is considered as the most prevalent risk factor for AD, was also studied. The proposed method successfully detected statistically significant hippocampal difference between ApoE4 carriers and noncarriers in the non-demented cohort of ADNI baseline dataset, which consists of mild cognitive impairment (MCI) patients and healthy control subjects. The results demonstrate that the ApoE4 genotype may be associated with accelerated brain atrophy so that this work provides a new MRI analysis tool that may help presymptomatic AD research.

2.1 Introduction

In brain imaging study, although most subcortical structure analysis work use volume as the atrophy measurement [84, 90-95], recent research [85, 96-105] has demonstrated that surface-based subcortical structure analysis may offer advantages over volume measure. For example, the surface-based methods have studied patterns of hippocampal subfield atrophy and detailed point-wise correlation between atrophy and cognitive functions/biological markers. There are several methods that match surfaces of subcortical structures using parametric surfaces, such as contour parameterization [85, 106, 107], SPHARM (spherical harmonic) methods [96], large deformation diffeomorphism metric matching (LDDMM) [103, 108, 109], Laplacian-Beltrami eigen-features [110], multi-resolution geodesic construction on Riemannian manifolds [111] and Beltrami holomorphic flow [112]. In recent years, a set of parametric surfaces have been introduced using concepts from conformal geometry which provide a rigorous framework for representing, splitting, parameterizing, matching and measuring subcortical surfaces [79]. They have been successfully applied to study HIV/AIDS [79] and AD [27]. Even so, an automated substructure surface registration system that uses complete surface geometric features for a diffeomorphic mapping is still highly advantageous.

Using holomorphic 1-forms, a global conformal parameterization can be developed to map a surface to a rectangular domain in the Euclidean plane [70]. On the other hand, fluid registration has been widely used to drive a large-deformation diffeomorphic flow for image correspondence. By adjusting the viscous fluid method to parametrically match scalar-valued signals representing surface geometry, I derive a method for landmark-free surface registration. Since both kinds of mappings are diffeomorphic, their composition leads to diffeomorphic shape correspondence (i.e., a smooth, one-to-one correspondence). Wang et. al [65] proposed an automated surface fluid registration method based on conformal mapping and image fluid registration, and applied it to register human faces and hippocampal surfaces. Here, the Navier-Stokes equation in [65, 113] is extended into general surface space using covariant derivatives. Due to the simple Riemannian metric induced by conformal parameterization, the general Navier-Stokes equation can be easily adjusted for area distortion. As pointed out in [114], inverse consistent registration method is more robust than the traditional unidirectional registration. Leow et al. [114] presented a novel inverse consistent image registration scheme with linear elastic regularization. Chiang et al. [115] extended the method in [114] with viscous fluid regularization to enable large deformations, and applied the method to diffusion tensor images. I extend the method proposed in [115] to surfaces. By solving the Navier-Stokes equation on the surface and matching geometrically-informed scalar functions, an inverse consistent surface registration algorithm is developed.

In general, in order to study structural features of the brain, such as cortical gray matter thickness, complexity, and deformation over time, etc., there are roughly two different approaches, deformation-based morphometry (DBM) [116-119] and tensor-based morphometry (TBM) [29, 32, 120]. DBM tends to analyze 3D displacement vector fields encoding relative positional differences across subjects, while TBM tends to examine spatial derivatives of the deformation maps registering brains to a common template, constructing morphological tensor maps such as the Jacobian determinant, torsion or vorticity. One advantage of TBM for surface morphometry is that TBM can make use of the intrinsic Riemannian surface metric to characterize local anatomical changes. Chung et al. [32] showed that the single value of the determinant of Jacobian can reliably detect surface morphometry due to autism. In the proposed algorithm, multivariate statistics based on surface deformation tensors are used to study brain surface morphometry as proposed in [69, 82]. The multivariate tensor-based morphometry (mTBM) computes statistics from the Riemannian metric tensors that retain the full information in the deformation tensor fields, thus may be more powerful in detecting surface difference than many other statistics [2, 27, 70, 79]. The hypothesis is that, together with mTBM as the surface statistics, the proposed surface fluid registration method may help boost statistical power to detect disease burden and genetic influence on hippocampal morphometry compared with some existing researches in the literature. Here I set out to validate the algorithm in the Alzheimer's Disease Neuroimaging Initiative (ADNI) baseline dataset. In AD research, magnetic resonance imaging (MRI) based measures in several brain structures, including whole-brain [121-123], entorhinal cortex [124], hippocampus [84, 85, 92, 93, 105], and temporal lobe volumes [125], as well as ventricular enlargement [84, 85], correlate closely with changes in cognitive performance, supporting their validity as markers of disease progression [97, 104]. Of all the MRI markers of AD, hippocampal atrophy assessed on high-resolution T1-weighted MRI is the best established and validated. One of the key research topics for clinical assessment in diagnosis and monitoring of progression of patients with suspected Alzheimer dementia is to establish and validate efficient biomarkers based on subcortical structures including hippocampus.

Figure 2.1 summarizes the overall step sequence in the system. The brain MR image is from ADNI baseline dataset. The hippocampal regions and surfaces are segmented and constructed automatically. We then compute hippocampal surface conformal parameterization with holomorphic 1-forms and obtain their feature images that consist of conformal factor and mean curvature. With the inverse consistent surface fluid registration method, symmetric displacements in both surfaces are enforced ($\boldsymbol{h}(\boldsymbol{x})$ denotes the forward mapping and $\boldsymbol{g}(\boldsymbol{x})$ denotes the inverse mapping, where $\boldsymbol{g}(\boldsymbol{x}) = \boldsymbol{h}^{-1}(\boldsymbol{x})$). Multivariate statistics are computed to study differences between diagnostically different groups and the genetic influence on hippocampal morphometry.

2.2 Surface Fluid Registration System

2.2.1 Image Segmentation and Preprocessing

The FIRST software (http://fsl.fmrib.ox.ac.uk/fsl/fslwiki/FIRST) is used to automatically segment the hippocampal volume from T1-weighted MRI scans. FIRST is an integrated surface registration and segmentation tool developed as part of the FSL library, which is written mainly by members of the Analysis Group, FMRIB, Oxford, UK. FIRST is able to extract subcortical structures and assign the image voxels with different numerical labels. Then the binary image segmentation can be obtained by a simple threshold process. After obtaining the binary segmentation, a topology-preserving level set method [126] is used to build surface models. Based on that, the marching cubes algorithm [127] is applied to obtain triangular surface meshes.

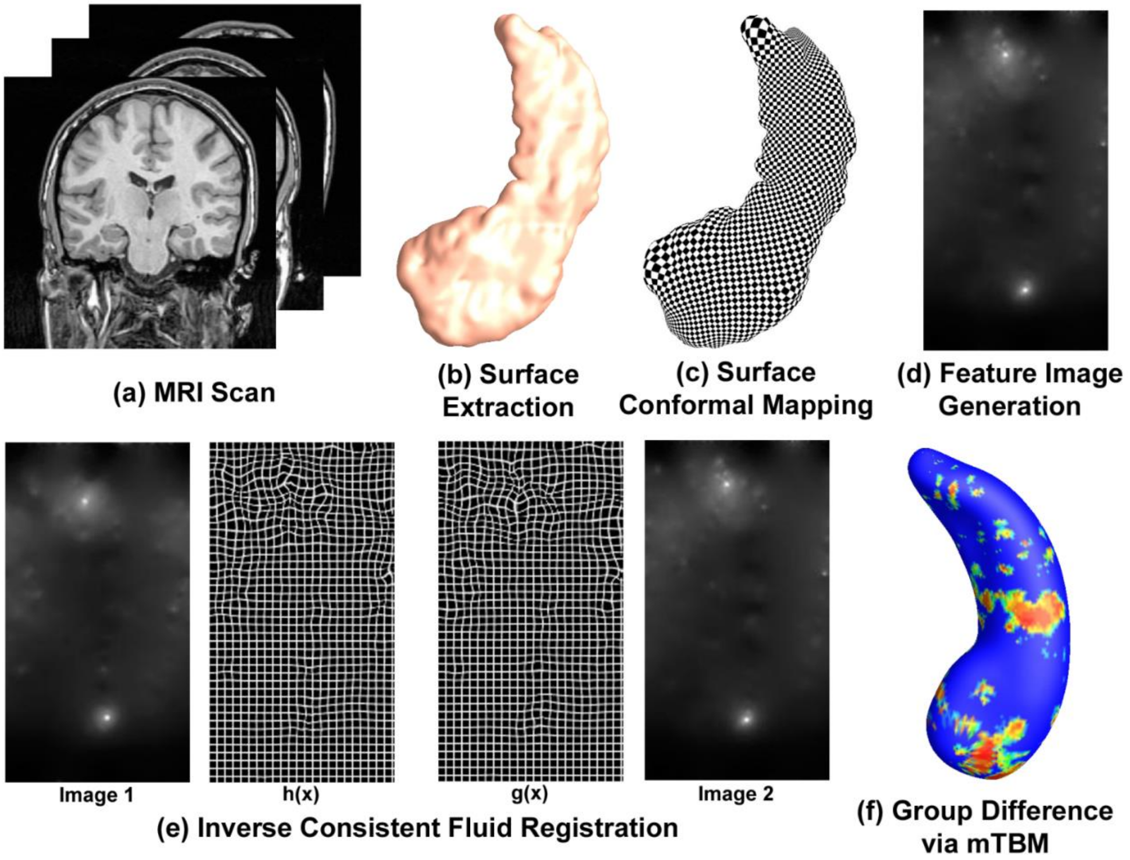

Figure 2.1. A segmentation and surface construction chart showing the key steps in the system. After the hippocampal surfaces are extracted from MRI scans automatically with FIRST, we compute their conformal parameterizations with holomorphic 1-forms. Then feature images are generated by combining the local conformal factor and mean curvature that are computed from the conformal parameterizations. After the inverse consistent fluid registration is done in the feature image domain, we deform the surfaces using the obtained displacements. The statistics of mTBM are computed at each point on the resulting matched surface. Then the Hotelling T^2 test is applied to compute differences between two different groups.

However, the surface models constructed from medical image data, which has limited resolution and noise from scanning, may contain much noise. Surface smoothing may help restore the original shape and overcome partial volume effects. Furthermore, the triangular meshes obtained by the marching cubes algorithm [127] often contain obtuse angles, which make the meshes inappropriate for direct use in conformal parameterization. Here, to compute the conformal parameterization, we need firstly compute harmonic forms and they require solving a linear system to minimize the harmonic energy [27]. In the finite element formulation, there is a cotangent weight term [25] which should be positive. The formulation becomes unsolvable if there are too many obtuse angles (negative cotangent weight terms). Thus mesh smoothing is needed before any further processing. Here a two-step mesh smoothing method is applied to the hippocampal surfaces. The smoothing process consists of mesh simplification using “progressive meshes” [128] and mesh refinement by Loop subdivision surface [129]. All the meshes were smoothed by several iterations of mesh simplification using “progressive meshes” and Loop subdivision. Later all the smoothed meshes were normalized into a standard space using affine transformation with a 9-parameter (3 parameters for translation, 3 parameters for rotation, and 3 parameters for scaling) matrix that was computed by FIRST.

2.2.2 Surface Conformal Parameterization with Holomorphic 1-Forms

Let S be a surface in $\mathbb{R}^3$ with an atlas $\{(U_\alpha, z_\alpha)\}$, where (U_α, z_α) is a coordinate chart defined on S. The atlas thus is a set of consistent charts with smooth transition functions between overlapping charts. Here $z_\alpha: U_\alpha \to \mathbb{C}$ maps an open set $U_\alpha \subset S$ to a complex plane $\mathbb{C}$. If on any chart (U_α, z_α) in the atlas, the Riemannian metric or the first fundamental form can be formulated as $ds^2 = \lambda(z_\alpha)^2 dz_\alpha d\bar{z}_\alpha$, and the transition maps $z_\beta \circ z_\alpha^{-1}: z_\alpha(U_\alpha \cap U_\beta) \rightarrow z_\beta(U_\alpha \cap U_\beta)$ are holomorphic, the atlas could be called conformal. Given a conformal atlas, a chart is compatible with the atlas if adding this chart still generates a conformal atlas. A conformal structure is obtained by adding all possible compatible charts to a conformal atlas. A Riemann surface is a surface with a conformal structure. All metric oriented surfaces are Riemann surfaces. One coordinate chart in the conformal structure introduces a conformal parameterization between a surface patch and the image plane. The conformal parameterization is angle-preserving and intrinsic to the surface geometry [71, 130].

For a Riemann surface S with genus g > 0, its conformal structure can always be represented in terms of a holomorphic 1-form basis, which is a set of 2g functions $\tau_i: K_1 \rightarrow \mathbb{C}, i = 1, \ldots, 2\text{g}$ [131]. Here, K_1 represents the simplicial 1-complex (In mathematics, a simplicial complex is a topological space that is constructed by gluing together points, line segments, triangles, and their n-dimensional counterparts. A simplicial k-complex K_k is a slimplicial complex where the largest dimension of any component in K_k equals to k. In discrete settings, a simplicial 1-complex is an edge.). Any holomorphic 1-form τ is a linear combination of these functions. This finite-dimensional linear space generates all possible conformal parameterizations of surface S and the quality of a global conformal parameterization is fundamentally determined by the choice of the holomorphic 1-form [27, 131]. By considering the holomorphic 1-form as an $\mathbb{R}^2$ function, the conformal parameterization $\phi: S \rightarrow \mathbb{R}^2$ at point p can be computed by integrating the holomorphic 1-form:

$$\phi(p) = \int_{\gamma} \tau. \tag{2.1}$$

where γ is an arbitrary path joining p to a fixed point p_0 on the surface. The details of the holomorphic 1-form based conformal parameterization algorithms were reported in prior work [27, 131]. Figure 2.2 illustrates a pair of hippocampal surfaces and their conformal parameterizations to a rectangular domain.

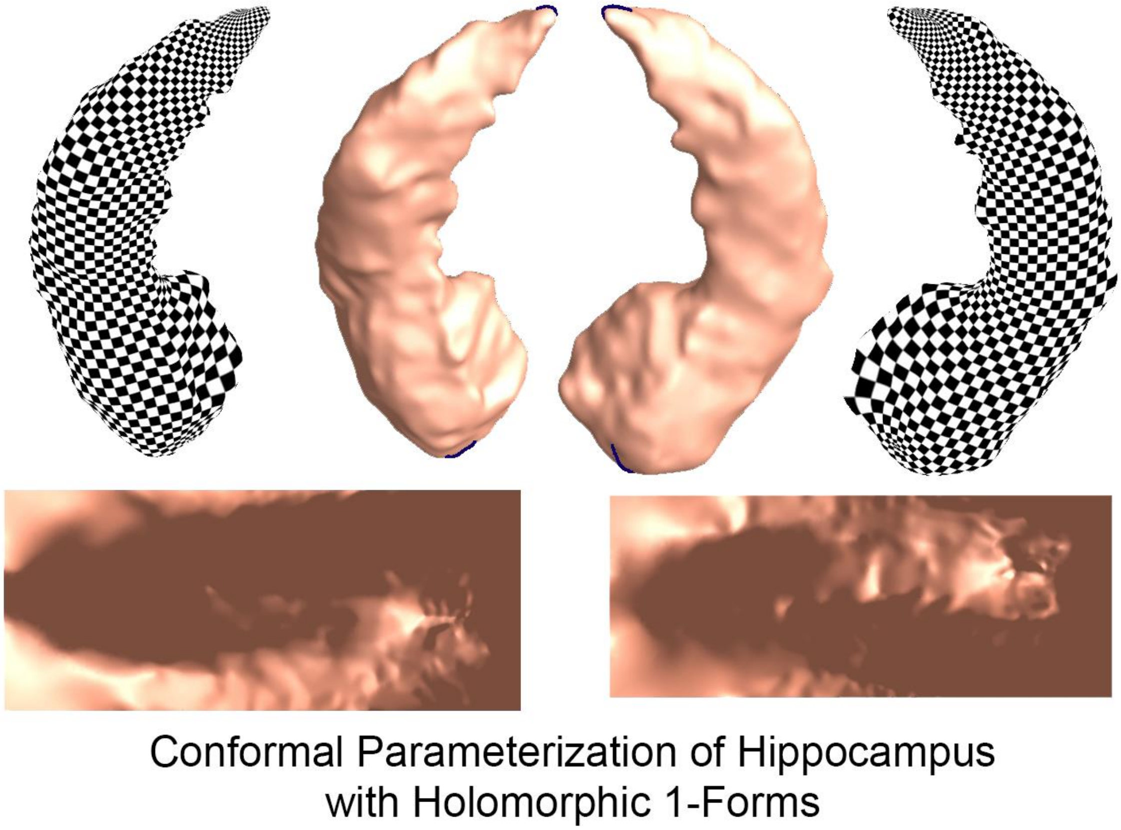

Figure 2.2. Illustration of surface conformal parameterization. The boundaries generated in the topology optimization step (Sec. 2.3.2) are labeled in blue color. Each side of the hippocampal surfaces is conformally mapped to a rectangle in the parameter domain. The overlaid checkboard texture is used to demonstrate angle-preserving property; the shading effect on the parameter space is generated by rendering the normal direction on each point of the original 3D surface.

2.2.3 Surface Conformal Representation

It has been known that surface registration requires defining a lot of landmarks in order to align corresponding functional regions. Labeling features could be accurate but time-consuming. Here we show that surface conformal parameterization could represent surface geometric features, thus avoiding the manual definition of landmarks.

For a general surface and its conformal parameterization $\phi: S \to \mathbb{R}^2$, the conformal factor at a point p can be determined by the formula:

$$\lambda(p) = \frac{\text{Area}(B_\epsilon(p))}{\text{Area}(\phi(B_\epsilon(p)))} \tag{2.2}$$

where $B_\epsilon(p)$ is an open ball around p with a radius ϵ. The conformal factor λ encodes a lot of geometric information about the surface and can be used to compute curvatures and geodesic. In this work, the surface mean curvatures are computed only from the derivatives of the conformal factors as proposed in [132], instead of the three coordinate functions and the normal, which are generally more sensitive to digitization errors. Mathematically, the mean curvature is defined as:

$$H = \frac{1}{2\lambda}\text{sign}(\phi)|\Delta\phi| \tag{2.3}$$

where $\text{sign}(\phi) = \frac{<\Delta\phi, \vec{N}>}{|\Delta\phi|}$. Using this formulation of H, the surface normal $\vec{N}$ is only used when computing $\text{sign}(\phi)$, which takes the value 1 or -1. Thus, the surface normal does not need to be accurately estimated and still we can get more accurate mean curvatures. Using the Gauss and Codazzi equations, one can prove that the conformal factor and mean curvature uniquely determine a closed surface in $\mathbb{R}^3$, up to a rigid motion [41]. We call them the conformal representation of the surface. Figure 2.3 shows the computed conformal factor (left) and mean curvature (right) on a pair of hippocampal surfaces with color indices according to the values. Since conformal factor and mean curvature encode both surface intrinsic structure and 3D embedding information, they are complete surface features to be used for solving surface registration problems [113, 133].

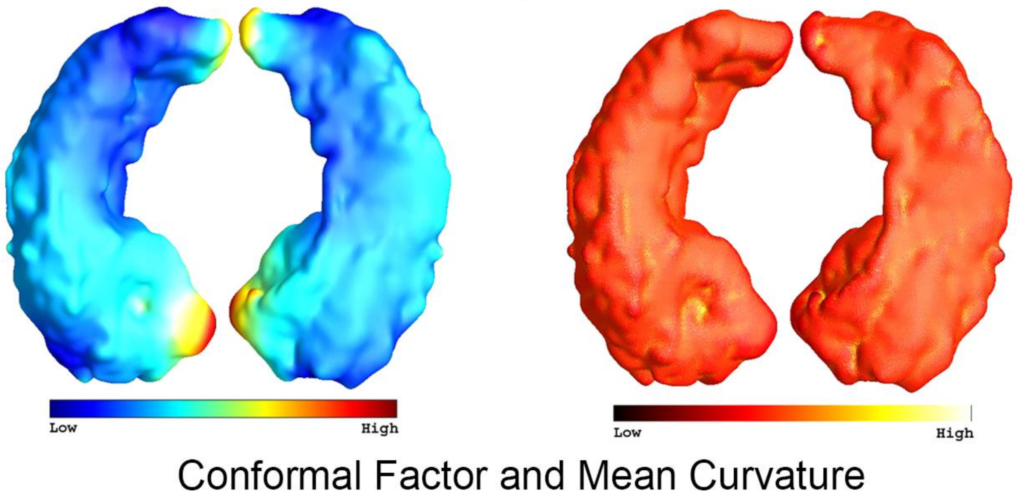

Figure 2.3. Illustration of surface geometric features, which are color-coded on a pair of hippocampal surfaces. The geometric features are used for surface registration and morphometric analysis.

2.2.4 Inverse Consistent Surface Fluid Registration

After computing surface geometric features, the surfaces are aligned in the parameter domain with a fluid registration technique to maintain smooth, one-to-one topology [51]. Using conformal mapping, the surface registration problem has essentially been converted to an image registration problem. Prior work [113] proposed an automated surface fluid registration method combining conformal mapping and image fluid registration [134] with mutual information [135-139] as the driving force of the viscous fluid. In [113], the mutual information between two surface feature images, i.e., the conformal representations of the two surfaces that need to be registered, was maximized by the viscous fluid flow as in [134]. On $\mathbb{R}^2$, fluid flow is governed by the Navier-Stokes equation. For compressible fluid flow, we have

$$\mu\Delta\boldsymbol{v}(\boldsymbol{x}) + (\mu+\tau)\nabla\big(\nabla\cdot\boldsymbol{v}(\boldsymbol{x})\big) = \boldsymbol{f}\big(\boldsymbol{x},\boldsymbol{u}(\boldsymbol{x})\big) \tag{2.4}$$

Here $\boldsymbol{v}(\boldsymbol{x})$ is the deformation velocity, μ and τ are the viscosity constants. $\boldsymbol{f}(\boldsymbol{x},\boldsymbol{u}(\boldsymbol{x}))$ is the force field that is used to drive the fluid flow, which was defined as the mutual information in [113].

To simulate fluid flow on Riemann surfaces, Eq. 2.4 needs to be extended into surface space by the manifold version of Laplacian and divergence [140-142]. By covariant derivatives, the Navier-Stokes equation for Riemann surface can be defined as:

$$\frac{\mu}{\lambda}\Delta\boldsymbol{v} + \frac{\mu+\tau}{\lambda}\nabla(\nabla\cdot\boldsymbol{v}) = \boldsymbol{f} \tag{2.5}$$

where λ is the conformal factor as introduced in Sec. 2.2.3. Please refer the appendix A for the derivation of Eq. 2.5. It is well known that area distortion is an inevitable problem in conformal parameterization. However, considering the definition of conformal factor λ as Eq. 2.2, we can see that conformal factor is a smooth function which describes the stretching effect of conformal parameterization [143]. In Eq. 2.5, by factoring out the conformal factor λ, the flow induced in the parameter domain is adjusted for the area distortion introduced by the conformal parameterization. As a result, Eq. 2.5 is now governing fluid flow on the manifolds. Considering that hippocampi across the population should have similar shapes, we assume the conformal representations of different hippocampi have similar intensity range and distribution. Thus, the body force $\boldsymbol{f}$ in Eq. 2.5 driving the fluid flow in this study is defined as the sum of squared intensity differences (SSD) between the deforming image and the template image. In the experiments, the SSD based energy formulation has similar performance with mutual information energy which was adopted in prior work [113] while significantly improves algorithm efficiency compared with the latter method. As shown in figure 2.4, the performance of the inverse consistent fluid registration driven by SSD and mutual information is illustrated, respectively, on the synthetic C-shape images. The figure shows that these two types of driving forces were able to obtain similar registration results while the time cost by SSD was 14.15 seconds. It was much more efficient than mutual information based energy formulation, which ran up to 1730.15 seconds. Both algorithms were executed on a 2.66GHz Intel Quad CPU Q8400 PC with Windows 7 64-bit operating system. Given the large number of surfaces to be registered, we chose to adopt SSD based energy formulation for improved efficiency [83, 144]. Since conformal mapping and fluid registration generate diffeomorphic mappings, a diffeomorphic surface-to-surface mapping is then recovered that matches surfaces in 3D.

As pointed out in [114], image registration problem should be symmetric, i.e., the correspondences established between the two images should not depend on the order people use to compare them. However, traditional non-linear image registration algorithms are not symmetric, thus the deformation field depends on which image is assigned as the deforming image and which image the non-deforming target image. Furthermore, the asymmetric algorithms tend to penalize the expansion of image regions more than the shrinkage [145], making these methods problematic in applications where the Jacobian of the mappings is interpreted as measuring anatomical tissue loss or expansion. Many inverse consistent registration algorithms [110, 146-148] have been proposed to overcome the shortcomings of conventional inverse non-consistent methods. Leow et al. [114] proposed a novel inverse consistent image registration method. Instead of enforcing inverse consistency using an additional penalty that penalizes inconsistency error as in [146], the method in [114] directly modeled the reverse mapping by inverting the forward mapping. Chiang et al. [115] replaced the linear elastic regularizer in [114] with the fluid regularization to enable large deformations and applied the inverse consistent fluid registration algorithm to diffusion tensor images. Here with the inverse consistent scheme proposed in [115], we extend Eq. 2.5 into an inverse consistent surface fluid registration method.

(a) Inverse consistent fluid registration driven by sum of squared difference

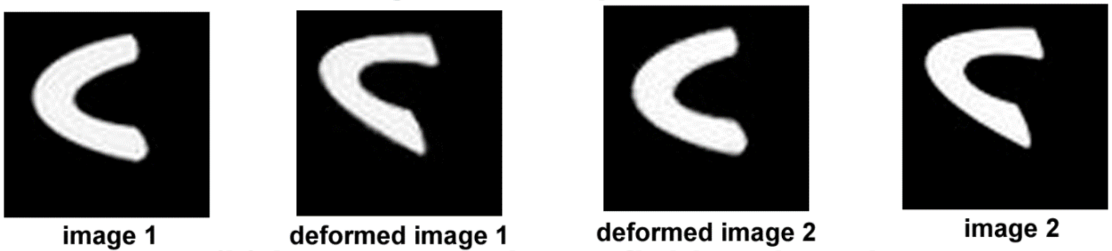

(b) Inverse consistent fluid registration driven by mutual information

Figure 2.4. Inverse consistent fluid registration driven by sum of squared intensity difference (SSD) (a) and mutual information (MI) (b) respectively on synthetic images to demonstrate the efficiency of SSD. Although the registration results were similar, the SSD based method took 14.15 seconds while the MI based method took 1730.15 seconds.

Let $I_1(\boldsymbol{x}), I_2(\boldsymbol{x})$ be two images, using the sum of squared intensity differences as the matching cost function, the inverse consistent image registration problem seeks two mappings $\boldsymbol{h}(\boldsymbol{x})$ and $\boldsymbol{g}(\boldsymbol{x})$ to minimize the following energy function:

$$\mathrm{E}\big(I_1(\boldsymbol{x}), I_2(\boldsymbol{x})\big) = \int_\Omega \big|I_1\big(\boldsymbol{h}(\boldsymbol{x})\big) - I_2(\boldsymbol{x})\big|^2 d\boldsymbol{x} + \alpha R\big(\boldsymbol{h}(\boldsymbol{x})\big) + \int_\Omega \big|I_2\big(\boldsymbol{g}(\boldsymbol{x})\big) - I_1(\boldsymbol{x})\big|^2 d\boldsymbol{x} + \alpha R(\boldsymbol{g}(\boldsymbol{x})) \quad (2.6)$$

where $\boldsymbol{h}(\boldsymbol{x}) = \boldsymbol{x} - \boldsymbol{u}_f(\boldsymbol{x})$ is the mapping from image I_1 to image I_2 (forward direction) and $\boldsymbol{u}_f(\boldsymbol{x})$ is the forward displacement field. $\boldsymbol{g}(\boldsymbol{x}) = \boldsymbol{x} - \boldsymbol{u}_b(\boldsymbol{x})$ is the mapping from image I_2 to image I_1 (backward direction) and $\boldsymbol{u}_b(\boldsymbol{x})$ is the backward displacement field, $\boldsymbol{g}(\boldsymbol{x}) = \boldsymbol{h}^{-1}(\boldsymbol{x})$. α is a positive scalar weighting of the regularization terms applied to the forward and backward mappings. Following prior work in fluid registration [114, 115], we let $\alpha = 1$ to achieve a fast and stable convergence. Eq. 2.6 is symmetric and does not depend on the order of I_1 and I_2, i.e., $E(I_1, I_2) = E(I_2, I_1)$. Suppose given two surfaces S_1, S_2 and their conformal representation I_1, I_2in $\mathbb{R}^2$. With fluid regularization scheme, $R(\boldsymbol{h}(\boldsymbol{x}))$ is defined as $\int_0^1 \int_\Omega \big\|L\boldsymbol{v}_f(\boldsymbol{x})\big\|^2 d\boldsymbol{x}dt$ and $R(\boldsymbol{g}(\boldsymbol{x}))$ is defined as $\int_0^1 \int_\Omega \|L\boldsymbol{v}_b(\boldsymbol{x})\|^2 d\boldsymbol{x}dt$ with the forward and backward velocities $\boldsymbol{v}_f(\boldsymbol{x})$ and $\boldsymbol{v}_b(\boldsymbol{x})$, respectively. $L = \frac{\mu}{\lambda}\Delta + \frac{\mu+\tau}{\lambda}\nabla(\nabla\,\cdot)$ is the surface linear operator as in Eq. 2.5. Then the energy function in Eq. 2.6 can be minimized by solving for the velocities $\boldsymbol{v}_f(\boldsymbol{x})$ and $\boldsymbol{v}_b(\boldsymbol{x})$ in the following general Navier-Stokes equations:

$$\frac{\mu}{\lambda_{f,b}}\Delta\boldsymbol{v}_{f,b} + \frac{\mu+\tau}{\lambda_{f,b}}\nabla\big(\nabla\cdot\boldsymbol{v}_{f,b}\big) = \boldsymbol{f}_{f,b} \quad (2.7)$$

where the forward force field $\boldsymbol{f}_f = -\left[I_1\left(\boldsymbol{x} - \boldsymbol{u}_f(\boldsymbol{x})\right) - I_2(\boldsymbol{x})\right]\nabla I_1(\boldsymbol{x} - \boldsymbol{u}_f(\boldsymbol{x}))$ and backward force field $\boldsymbol{f}_b = -\left[I_2\left(\boldsymbol{x} - \boldsymbol{u}_b(\boldsymbol{x})\right) - I_1(\boldsymbol{x})\right]\nabla I_2(\boldsymbol{x} - \boldsymbol{u}_b(\boldsymbol{x}))$. λ_f is the conformal factor of surface S_1 and λ_b is the conformal factor of surface S_2.

With the mappings $\boldsymbol{h}(\boldsymbol{x}), \boldsymbol{g}(\boldsymbol{x})$ initialized as the identical mapping at $t = 0$, the forward and backward mappings at time t are given by the following equations as in [114]:

$$\begin{aligned} \boldsymbol{h}_t(\boldsymbol{x}) &= \boldsymbol{h}_{t-1}(\boldsymbol{x}) + \epsilon\boldsymbol{\eta}_1(\boldsymbol{x}) + \epsilon\boldsymbol{\eta}_2(\boldsymbol{x}) \\ \boldsymbol{g}_t(\boldsymbol{x}) &= \boldsymbol{g}_{t-1}(\boldsymbol{x}) + \epsilon\boldsymbol{\xi}_1(\boldsymbol{x}) + \epsilon\boldsymbol{\xi}_2(\boldsymbol{x}) \end{aligned} \tag{2.8}$$

Here, ϵ is an infinitesimally small positive time step. $\boldsymbol{\eta}_1, \boldsymbol{\eta}_2, \boldsymbol{\xi}_1, \boldsymbol{\xi}_2$ are computed as [115]:

$$\begin{aligned} \boldsymbol{\eta}_1(\boldsymbol{x}) &= -\left(\nabla\boldsymbol{h}_{t-1}(\boldsymbol{x})\right)\boldsymbol{v}_f^{t-1}(\boldsymbol{x}), \boldsymbol{\eta}_2(\boldsymbol{x}) = \boldsymbol{v}_b^{t-1}(\boldsymbol{h}_{t-1}(\boldsymbol{x})) \\ \boldsymbol{\xi}_1(\boldsymbol{x}) &= \boldsymbol{v}_f^{t-1}(\boldsymbol{g}_{t-1}(\boldsymbol{x})), \boldsymbol{\xi}_2(\boldsymbol{x}) = -\left(\nabla\boldsymbol{g}_{t-1}(\boldsymbol{x})\right)\boldsymbol{v}_b^{t-1}(\boldsymbol{x}) \end{aligned} \tag{2.9}$$

2.2.5 Multivariate Tensor-Based Morphometry Statistics

Suppose $\phi: S_1 \to S_2$ is a map from the surface S_1 to the surface S_2. To simplify the formulation, the isothermal coordinates of both surfaces are used as the arguments. Let (u_1, v_1) be the isothermal coordinates of S_1 and S_2. The Riemannian metric of S_i is represented as $\mathbf{g}_i = e^{2\lambda_i}(du_1^2 + dv_1^2), i = 1{,}2$. In the local parameters, the map ϕ can be represented as $\phi(u_1, v_1) = (\phi_1(u_1, v_1), \phi_2(u_1, v_1))$. The derivative map of ϕ is the linear map between the tangent spaces, $d\phi: TM(p) \to TM(\phi(p))$, induced by the map ϕ. In the local parameter domain, the derivative map is the Jacobian of ϕ:

$$d\phi = \begin{bmatrix} \frac{\partial\phi_1}{\partial u_1} & \frac{\partial\phi_1}{\partial v_1} \\ \frac{\partial\phi_2}{\partial u_1} & \frac{\partial\phi_2}{\partial v_1} \end{bmatrix}$$

Let the position vector of S_1 be $\mathrm{r}(u_1, v_1)$. Denote the tangent vector fields as $\frac{\partial}{\partial u_1} = \frac{\partial \mathrm{r}}{\partial u_1}, \frac{\partial}{\partial v_1} = \frac{\partial \mathrm{r}}{\partial v_1}$. Because (u_1, v_1) are isothermal coordinates, $\frac{\partial}{\partial u_1}$ and $\frac{\partial}{\partial v_1}$ only differ by a rotation of $\pi/2$. Therefore, an orthonormal frame on the tangent plane of S_1 can be constructed as $\{e^{-\lambda_1}\frac{\partial}{\partial u_1}, e^{-\lambda_1}\frac{\partial}{\partial v_1}\}$.

Similarly, an orthonormal frame on S_2 for its isothermal coordinates can be constructed. Since any two surfaces are locally conformal [149], we can have an orthonormal frame on S_2 as $\{e^{-\lambda_2}\frac{\partial}{\partial u_1}, e^{-\lambda_2}\frac{\partial}{\partial v_1}\}$. The derivative map under the orthonormal frames is represented as

$$d\phi = e^{\lambda_2 - \lambda_1}\begin{bmatrix} \frac{\partial \phi_1}{\partial u_1} & \frac{\partial \phi_1}{\partial v_1} \\ \frac{\partial \phi_2}{\partial u_1} & \frac{\partial \phi_2}{\partial v_1} \end{bmatrix}$$

In practice, smooth surfaces are approximated by triangle meshes. In the triangle mesh surface, the derivative map $d\phi$ is approximated by the linear map from one face $[v_1, v_2, v_3]$ to another $[w_1, w_2, w_3]$. First, the surfaces $[v_1, v_2, v_3]$ and $[w_1, w_2, w_3]$ are isometrically embedded onto the plane $\mathbb{R}^2$ (i.e., $\lambda_1 = \lambda_2 = 0$ in the above equation), the planar coordinates of the vertices v_i, w_i are denoted by the same symbol v_i, w_i. Then the Jacobian matrix for the derivative map $d\phi$ can be explicitly computed as [70]

$$J = d\phi = [w_3 - w_1, w_2 - w_1][v_3 - v_1, v_2 - v_1]^{-1}. \tag{2.10}$$

The deformation tensor can be defined as $S = (J^T J)^{\frac{1}{2}}$ [117, 125]. Instead of analyzing shape change based on the eigenvalues of the deformation tensor, a new family of metrics, the "Log-Euclidean metrics" [150] is considered in the multivariate tensor-based morphometry (mTBM). In this framework, Riemannian computations can be converted into Euclidean ones once tensors have been transformed into their matrix logarithms [150]. This conversion makes computations on tensors easier to perform, as they are chosen such that the transformed values form a vector space, and statistical parameters can then be computed easily using the standard formulae for Euclidean space [69, 82].

To compute group differences with mTBM, the Hotelling's T^2 test [151-154] is applied on sets of values in the log-Euclidean space of the deformation tensors. Given two groups of $n \times 1$-dimensional vectors, $S_i, i = 1,2, \dots, p, T_j, j = 1,2, \dots, q$, we use the Mahalanobis distance M to measure the group mean difference,

$$M = \frac{N_S N_T}{N_S + N_T} (\bar{S} - \bar{T})^T \textstyle\sum^{-1} (\bar{S} - \bar{T}). \tag{2.11}$$

where N_S and N_T are the number of subjects in the two groups, $\bar{S}$ and $\bar{T}$ are the means of the two groups and $\sum$ is the combined covariance matrix of the two groups [27, 69, 79]. In current study, S and T are the log-Euclidean metrics, e.g. $S_i = \log[(J_i^T J_i)^{\frac{1}{2}}], i = 1,2, \dots, p$ and $T_j = \log[\left(J_j^T J_j\right)^{\frac{1}{2}}], j = 1,2, \dots, q$. Since the statistic M is a uni-variate, the analysis does not introduce any bias because of the increase of the variable number.

2.3 Experimental Results

2.3.1 Synthetic Surface Registration

In order to validate the effectiveness of the proposed method, we generated two synthetic surfaces as shown in figure 2.5 (a) and (b). The two C shapes have different sizes and positions. This can also be seen from the corresponding feature images at the bottom of figure 2.5 (a) and (b). The feature images were generated by summing up the local conformal factor and the mean curvature, expressed in the conformal parameterization domain. The black lines drawn on the surfaces are used to show equal distances on the surfaces and represent the differences in their shapes. With the inverse consistent fluid registration, figure 2.5 (c) and (d) show that the feature image of surface 1 was successfully registered to the feature image of surface 2 and the feature image of surface 2 was also registered to the feature image of surface 1. With the forward and backward mappings obtained in the parameter domain, a forward deformation and a backward deformation in surface 1 and surface 2 were induced, respectively. As can be seen from figure 2.5 (c) and (d), without changing the shape of the surfaces, the features on them are well aligned to each other.

2.3.2 Hippocampal Surface Registration

An automatic algorithm is used to identify two landmark curves at the front and back of each hippocampal surface, representing its anterior junction with the amygdala, and its posterior limit as it turns into the white matter of the fornix (the hole boundaries are shown as blue curves in figure 2.2) [27]. They are biologically valid and consistent landmarks across subjects. Given the hippocampal tube-like shape, these landmark curves can be automatically detected by checking the extreme points by searching along the first principle direction of geometric moments of surface [27, 155, 156]. For consistency, we also make sure these landmark curves have the same length. Next the surface is cut open along the two landmark curves. The new surface still has the same geometry but becomes a genus-0 surface with two open boundaries. This operation is termed as topology optimization. The goal is to compute curvilinear coordinates by holomorphic 1-forms (as shown in figure 2.1 (c)) which introduce a planar surface conformal parameterization. To register hippocampal surfaces, the boundaries serve as landmark curves and are forced to match each other. The computed curvilinear coordinates help apply fluid registration method to align other geometric similar areas. The topology optimization method has been applied in a few of prior work [27, 46, 70] and the method can identify these consistent landmark curves. Besides, for quality control purpose, all the hole-labeled meshes were manually checked. Then the surfaces were conformally mapped to a rectangle plane using holomorphic 1-forms.

We chose to encode hippocampal surface features using a compound scalar function based on the local conformal factor and the mean curvature: $C(u,v) = \beta\lambda(u,v) + H(u,v)$, where (u,v) is the conformal coordinates of the surface and β is a constant scalar to control the ratio of conformal factor and mean curvature. In the current study, similar to prior work [65, 113], β was empirically set as 7 for both visualization and registration. Then the dynamic range of the conformal representation was linearly scaled into $[0,255]$. With a target image randomly selected, the deforming images were aligned to the target image with the inverse consistent fluid registration method as introduced in Sec. 2.2.4. The alignment induced displacements in both u and v directions in a deforming image. Then the corresponding surface was deformed with these displacement vectors. After the cross-subject registration was computed with a selected target surface, the Jacobian matrix J was computed as Eq. 2.10. The "Log-Euclidean metric" on the set of deformation tensors, S, was computed as the matrix logarithm $\log(S)$. Since S is a positive-definite matrix, the first 3 of the 4 vector elements, analyzed in mTBM, are the logarithm of the deformation tensor S. The multivariate surface morphometry statistic is defined as a 3×1 feature vector consisting of the logged deformation tensors (detailed in Section 2.2.5).

(a) Synthetic Surface 1 and Its Feature Image

(c) Deformed Surface 1 and Deformed Feature Image

(b) Synthetic Surface 2 and Its Feature Image

(d) Deformed Surface 2 and Deformed Feature Image

Inverse Consistent Fluid Registration on Synthetic Surfaces

Figure 2.5. Matching of geometric features in the 2D parameter domain with the inverse consistent fluid registration of two synthetic surfaces. With the forward and backward mappings obtained in the parameter domain, we induce a forward deformation and a backward deformation in surface 1 and surface 2, respectively. As can be seen from (c) and (d), without changing the shape of the surfaces, the features on them are well aligned to each other.

2.3.3 Subjects

The proposed method was tested on the ADNI baseline dataset (http://adni.loni.usc.edu/) to study AD symptoms on hippocampus. At the time of downloading (09/2010), the baseline dataset consisted of 843 adults, ages 55 to 90, including 233 elderly healthy controls, 410 subjects with MCI and 200 AD patients. In this study, 1 subject from the control group and 2 subjects from the MCI group were manually excluded because of name duplication. For subjects with duplicated names, the one which was the repeated scan was retained. All subjects underwent thorough clinical and cognitive assessment at the time of acquisition, including the Mini-Mental State Examination (MMSE) score [157], Clinical Dementia Rating (CDR) [158], and Delayed Logical Memory Test [159]. Furthermore, 1 subject from each group (AD, MCI, and control) failed the FIRST segmentation step (Sec. 2.2.1) probably due to the original images' resolution or contrast issues. We also manually checked all the constructed and smoothed meshes and excluded 5 AD, 5 MCI, and 3 control subjects due to wrong topologies. As a result, the baseline MR hippocampus image data of 194 AD (age: 76.1 ± 7.6 years), 402 MCI (age: 75.0 ± 7.3 years), and 228 controls (age: 76.0 ± 5.0 years) were studied using the new system.

2.3.4 Associating Hippocampal Morphometry and Clinical Characteristics

To check the group difference between any two groups (AD vs. MCI, AD vs. control, and control vs. MCI), we performed a group comparison with the Hotelling's T^2 test as Eq. 2.11 on the 3-dimensional mTBM feature vectors. Specifically, for each point on the hippocampal surface, given 0.05 as the significant level, we ran a permutation test with

10,000 random assignments of subjects to groups to estimate the statistical significance of the areas with group differences in surface morphometry. The probability was estimated as the ratio of the Mahalanobis distance for a random assignment larger than the group Mahalanobis distance with the true group membership. The probability was later color coded on each surface point as the statistical p-map of group difference. Figure 2.6 (a)-(c) shows the p-maps of group difference detected between AD and control, AD and MCI, control and MCI groups, respectively, using mTBM as a measure of local surface area change and the significance level at each surface point as 0.05. In figure 2.6, the non-blue color areas denote the statistically significant difference areas between two groups. All group difference p-maps were corrected for multiple comparisons using the widely-used false discovery rate method (FDR) [160]. The FDR method decides whether a threshold can be assigned to the statistical map that keeps the expected FDR below 5% (i.e., no more than 5% of the voxels are false positive findings). Figure 2.6 (d)-(f) are the cumulative distribution function (CDF) plots showing the uncorrected p-values (as in a conventional FDR analysis). The x value at which the CDF plot intersects the $y = 20x$ line represents the FDR-corrected p-value or q-value. It is the highest statistical threshold that can be applied to the data, for which at most 5% false positives are expected in the map. In general, a larger q-value indicates a more significant difference in the sense that there is a broader range of statistic threshold that can be used to limit the rate of false positives to at most 5%. The use of the $y = 20x$ line is related to the fact that significance is declared when the volume of suprathreshold statistics is more than 20 times that expected under the null hypothesis [27].

In this experiment, the 194 AD, 402 MCI, and 228 healthy control surfaces were successfully registered by the proposed system. The FDR-corrected *p*-values for AD vs. control, AD vs. MCI, and control vs. MCI are 0.049, 0.0244, and 0.0483, respectively.

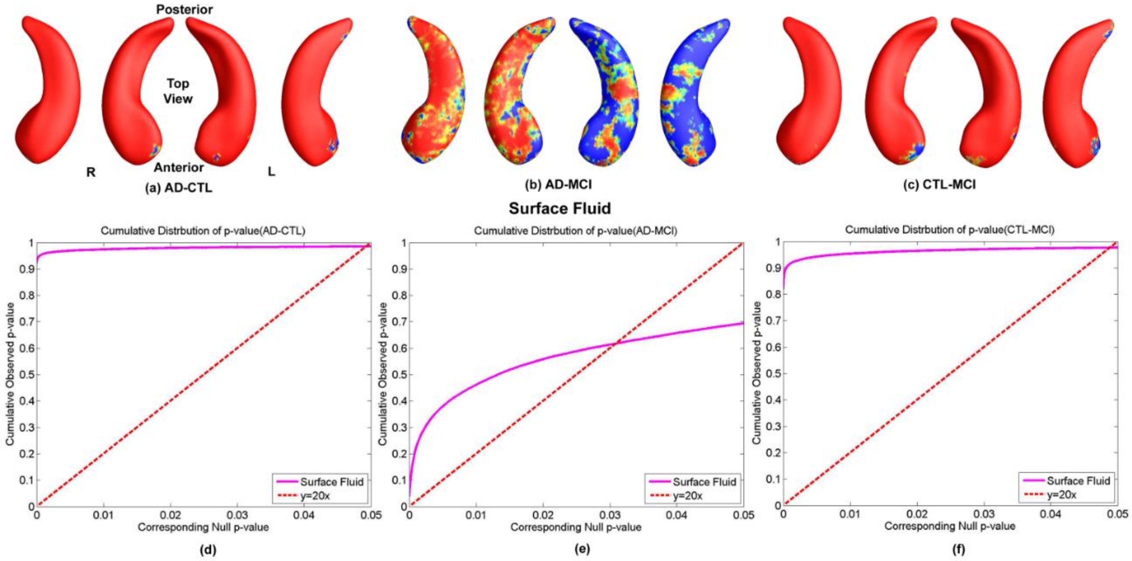

Figure 2.6. Illustration of inverse consistent surface fluid registration on map of local shape differences (*p*-values) between different diagnostic groups, based on the multivariate TBM method with hippocampal surfaces from ADNI baseline dataset, which were automatically segmented by FIRST. (a), (b), (c) are group difference *p*-maps between AD and control, AD and MCI, MCI and control, respectively, in 194 AD, 402 MCI, and 228 control subjects. The *p*-map color scale is the same as figure 2.8. (d), (e), (f) are the CDF plots.

2.3.5 Diagnostic Group Difference Comparison

In this experiment, the proposed method was compared with the popular surface registration tools FIRST and SPHARM [161] in diagnostic group difference detection.

FIRST is an integrated registration and segmentation tool [162]. Before segmentation, FIRST aligns all images onto the MNI152 template with FSL's integrated registration tool, FLIRT. This is a two-stage linear registration process. The first stage is an affine transformation of the whole head to the template with a standard 12 degrees of freedom registration and the second stage achieves a more accurate and robust 12 degrees of freedom registration to the template using a subcortical mask, which is defined in the MNI space. Following the registration, the inverse transformation will be applied to the surface models to get them into the native image space. The subsequent segmentation will be conducted in the native image space with the original non-interpolated voxel intensities [162]. With the default configuration, we obtained hippocampal surface models generated by FIRST, which are in their native image spaces. Then the surfaces were transformed into MNI standard space with the transformation matrices computed by FLIRT. As pointed out in [163], applying the original transformation to the mesh in the native image space is equivalent to reconstructing the mesh from the MNI space model. Thus all the surfaces have a common reference frame. The mTBM statistics were computed directly on these registered surfaces given that all the hippocampal surfaces have the same number of vertices and faces and the cross-subject vertex correspondence established by FIRST [162]. It is notable that some prior work [162-164] also took the established vertex correspondences across subjects by FIRST to study local subcortical structure shape difference between AD patients and healthy controls [162, 163] and between patients with learning disabilities and healthy controls [164].

SPHARM is another surface mapping tool which is extensively used in the literature [165-168]. It takes binary image segmentation as input and provides functions such as surface extraction, spherical harmonic mapping and surface registration; statistical tools are also included [161]. In the comparison experiments, the binary image segmentations processed by FIRST and thresholding, as described in Sec. 2.2.1, were resampled with FIRST to generate images with isotropic resolution of $1\text{mm} \times 1\text{mm} \times 1\text{mm}$. The generated isotropic images were used as the input of SPHARM. The parameters used with SPHARM package were set as recommended for hippocampus [161]. The template was chosen as the same template with the inverse consistent fluid registration. The registered surfaces obtained by SPHARM have the same number of vertices and faces and cross-subject vertex correspondence. The mTBM statistics were computed on these surfaces and the significance *p*-maps were generated. In the experiments, within the dataset that was processed in the fluid registration experiments, 4 AD and 6 MCI subjects failed in SPHARM system either due to segmentation failure or parameterization failure and they were excluded from these experiments. The details of the experiment with SPHARM are discussed in Appendix B.

For performance comparison purpose, figure 2.7 illustrates the experimental results showing group difference *p*-maps resulted from the inverse consistent surface fluid registration, FIRST, and SPHARM among the three diagnostic groups (AD, MCI and control) and the CDF plots. In this experiment, considering fairness, the 4 AD and 6 MCI subjects that failed in SPHARM were excluded from the dataset studied by surface fluid and FIRST methods. Thus, 190 AD, 228 controls, 396 MCI subjects were used to compare the surface fluid, FIRST, and SPHARM statistics. MCI is an intermediate stage between the expected cognitive decline of normal aging and the more pronounced decline of dementia. If MCI could be found and treated, the risk of AD will be significantly reduced. However, at MCI stage, changes in brain surface are not significant thus impose more difficulty on the detection. It can be seen from figure 2.6 and figure 2.7 that, in the experimental results, the most prominent results between the proposed method and other methods are in figure 2.6 (b) and figure 2.7 (b). Figure 2.6 (b) showed that the new method detected more significant different areas on right side of hippocampus between AD and MCI groups. On the left side, the significant areas are more on lateral zone proximal to the CA1 subfield and superior zone proximal to the combined CA2, CA3, CA4 subfields and gyrus dentaus (GD) [105, 169]. The results agree well with a prior discovery on morphology difference between AD and MCI groups [107], although these two methods use different hippocampal segmentation methods and different surface statistics. Comparing two results, the proposed method detected more significant areas. Table 2.1 gives the FDR corrected *p*-values comparison, which also shows that the proposed surface fluid registration system outperformed two other methods as the method achieved higher FDR corrected *p*-values.

	Surface Fluid	FIRST	SPHARM
AD-CTL	**0.0485**	0.0455	0.0461
AD-MCI	**0.0259**	0.0058	0.0134
CTL-MCI	**0.0479**	0.0408	0.0468

Table 2.1. FDR corrected *p*-values comparison. The proposed system generated stronger statistical power than two other subcortical morphometry systems.

(a) AD-CTL (b) AD-MCI (c) CTL-MCI

Surface Fluid

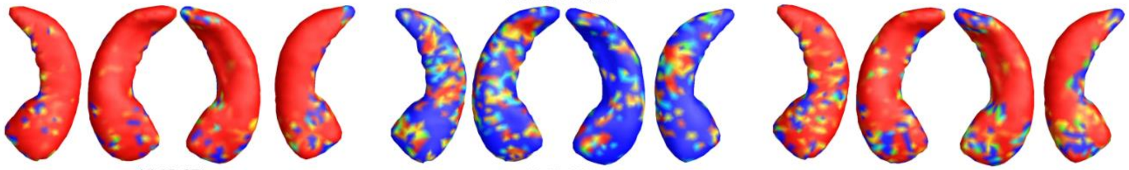

(d) AD-CTL (e) AD-MCI (f) CTL-MCI

FIRST

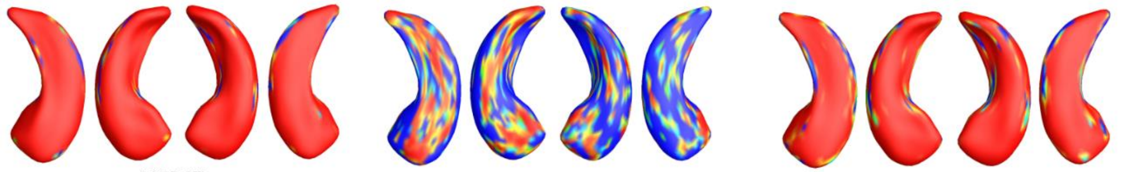

(g) AD-CTL (h) AD-MCI (i) CTL-MCI

SPHARM

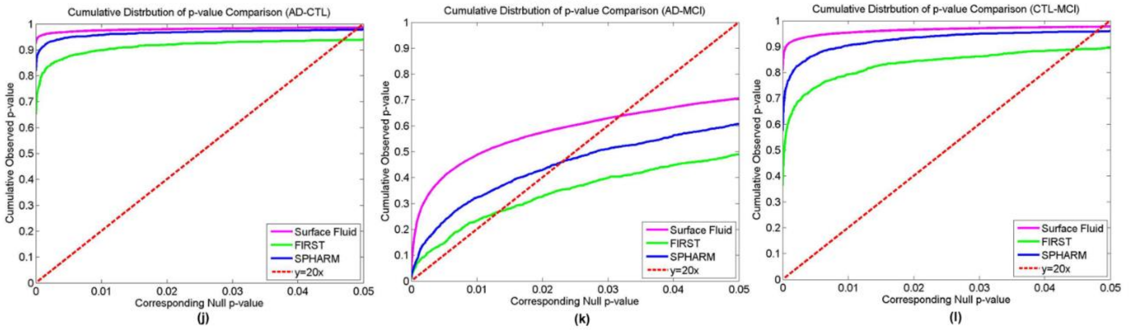

Figure 2.7. Illustration of comparisons of inverse consistent surface fluid registration with FIRST and SPHARM on map of local shape differences (*p*-values) between different diagnostic groups, based on the multivariate TBM method with hippocampal surfaces from ADNI baseline dataset, which were automatically segmented by FIRST. (a), (b), (c) are results of proposed method, (d), (e), (f) are result of FIRST, (g), (h), (i) are results of SPHARM on group difference between AD and control, AD and MCI, MCI and control, respectively, in 190 AD, 396 MCI, and 228 control subjects. The *p*-map color scale is the same as figure 2.8. (j), (k), (l) are the CDF plots showing the comparisons of the three methods.

2.3.6 Influence of Apolipoprotein E $\epsilon4$ Genotype on Hippocampal Morphometry

The Apolipoprotein E $\epsilon4$ allele (ApoE4) gene is of special interest in AD analysis as it is the major genetic risk for AD [170, 171]. It has been found that the presence of this allele is more frequent in AD patients than age-matching normal persons and is associated with a younger age of disease onset [170-174]. MRI studies have shown that this allele is associated with greater hippocampal atrophy [175-178] and one work [178] reported a significant correlation between hippocampal loss and memory deficits. However, only a few studies have investigated the local effect of ApoE4 on hippocampal atrophy in patients of AD/MCI or healthy control subjects [107, 179-181]. Morra et al. [107] discussed that in healthy elderly subjects, presence of ApoE4 may be correlated with future development of AD. In order to investigate this correlation, the authors designed two experiments: (1) group difference between ApoE4 carriers and noncarriers in all samples; (2) group difference between ApoE4 carriers and noncarriers in subjects that have not developed AD, i.e., MCI and control groups. The experiments are aimed to determine if the ApoE4 allele is linked with hippocampal atrophy in all subjects or in just the non-AD subjects. In their study [107], 400 subjects with 100 AD subjects, 200 MCI subjects, and 100 healthy controls from ADNI baseline dataset were analyzed with surfaces segmented by a prior work [99]. However, no significance was reported in [107]. Qiu et al. [180] studied ApoE4 effects on hippocampal volume and shape in 38 depressed patients without ApoE4, 14 depressed patients with one ApoE4 allele and 31 healthy controls without the ApoE4 allele. They found that the depressed patients with one ApoE4 showed more pronounced shape inward-compression in the anterior CA1 than the depressed patients without the ApoE4 when compared with the healthy controls without the ApoE4. Pievani et al. [181] designed more systematic experiments to study ApoE4 effects. Their studying subjects included 14 AD patients heterozygous for the ApoE4 allele and 14 patients not carrying the ApoE4 allele and 28 age-, sex-, and education-matched controls. Radial atrophy was analyzed by the same method that used in [107]. In the group difference study between AD patient ApoE4 carriers and AD noncarriers, they found statistically different atrophy on the left hippocampus but not on the right side. Neuropsychological studies also showed the accelerated decline of memory scores in a gene-dose pattern in ApoE4 carriers beginning between age 55 and 60 [182] that is further accelerated in ApoE4 homozygotes by cerebrovascular risk factors [183].

	ApoE Genotype	Number of Subjects	Gender (M/F)	Education	Age	MMSE at Baseline
AD	$\epsilon 2/\epsilon 2$	0	-	-	-	-
	$\epsilon 2/\epsilon 3$	4	1/3	15.00±2.24	74.25±8.26	22.00±1.58
	$\epsilon 2/\epsilon 4$	4	0/4	15.75±1.79	79.25±5.12	24.75±2.17
	$\epsilon 3/\epsilon 3$	52	27/25	15.15±2.05	76.96±8.58	23.23±2.05
	$\epsilon 3/\epsilon 4$	73	44/29	14.62±3.16	75.93±6.43	23.42±2.00
	$\epsilon 4/\epsilon 4$	34	20/14	14.71±2.67	71.92±7.17	23.44±1.83
Control	$\epsilon 2/\epsilon 2$	1	1/0	16	70	30
	$\epsilon 2/\epsilon 3$	24	12/12	15.83±3.14	76.13±5.68	28.83±1.14
	$\epsilon 2/\epsilon 4$	2	2/0	13.00±1.00	76.50±5.50	27.50±2.50
	$\epsilon 3/\epsilon 3$	125	69/56	16.20±2.71	76.29±4.83	29.18±0.89
	$\epsilon 3/\epsilon 4$	48	25/23	16.13±2.73	76.50±4.48	29.25±0.83
	$\epsilon 4/\epsilon 4$	4	2/2	16.75±1.92	73.75±3.34	29.00±0.71
MCI	$\epsilon 2/\epsilon 2$	0	-	-	-	-
	$\epsilon 2/\epsilon 3$	15	7/8	15.93±2.86	76.67±7.44	27.60±1.50
	$\epsilon 2/\epsilon 4$	10	7/3	16.50±2.33	74.20±8.58	28.00±1.26
	$\epsilon 3/\epsilon 3$	145	95/50	15.81±2.94	76.20±7.71	27.23±1.77
	$\epsilon 3/\epsilon 4$	141	91/50	15.61±3.06	74.82±6.63	26.94±1.76
	$\epsilon 4/\epsilon 4$	43	25/18	15.81±2.57	71.81±5.91	26.84±1.95

Table 2.2. Demographic information of studied subjects in ADNI baseline dataset.

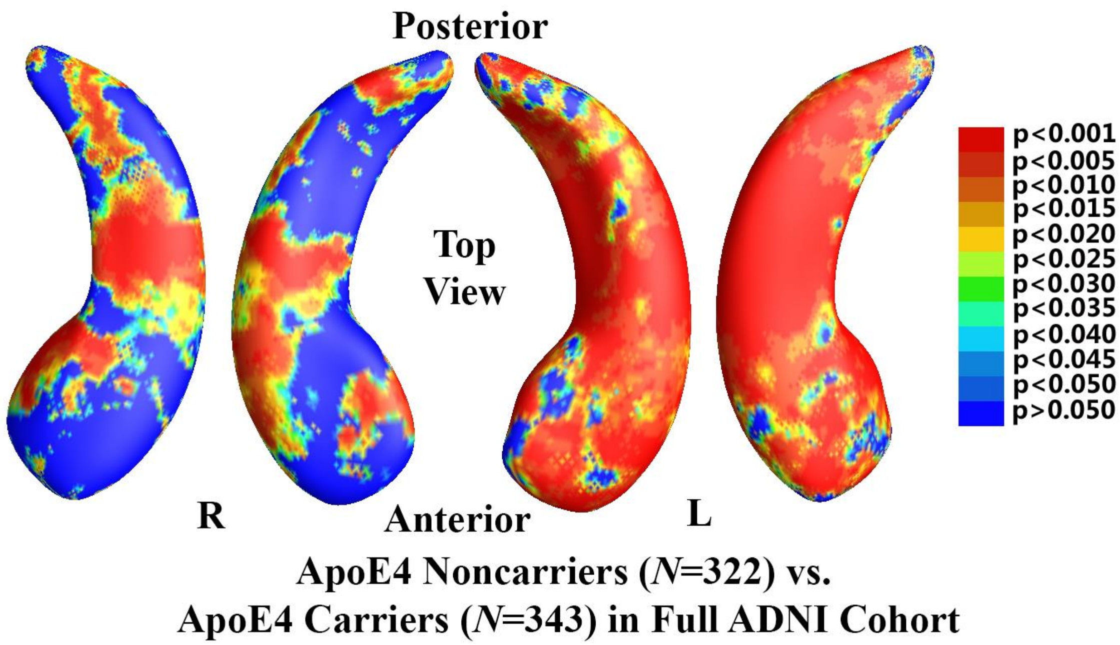

Figure 2.8. Illustration of local shape differences (*p*-values) between the ApoE4 noncarriers ($\epsilon 3/\epsilon 3$, $N = 322$) and carriers ($\epsilon 3/\epsilon 4$ and $\epsilon 4/\epsilon 4$, $N = 343$) in the full ADNI cohort. Non-blue colors show vertices with significant differences, at the predefined 0.05 level, uncorrected. The overall significance after multiple comparisons with permutation test is $p < 0.0002$.

Here the proposed system was applied to study the genetic influence of ApoE4 on hippocampal morphometry. Among the successfully processed hippocampal surfaces from the ADNI baseline dataset, 725 subjects with ApoE4 information, including 167 AD (age: 75.5±7.6 years), 354 MCI (age: 75.1±7.2 years), and 204 controls (age: 76.2±4.9 years) were studied in this experiment. Table 2.2 gives detailed demographic information of the subjects. Following prior work [99, 107], we pooled both the subjects who are heterozygous ApoE4 carriers ($\epsilon 3/\epsilon 4$) and homozygous ApoE4 carriers ($\epsilon 4/\epsilon 4$) together to form the ApoE4 carriers group and correlated presence of the ApoE4 allele with hippocampal morphometry, both (1) in the entire sample and (2) in non-demented (pooled MCI and controls) subjects. These two populations are termed as the full ADNI cohort and non-demented cohort, respectively.

This study applied the multivariate morphometry statistical analysis consists of mTBM (Sec. 2.2.5) and radial distance [85, 184]. As mTBM retains the full information in the deformation tensor fields, it is very sensitive to deformations such as rotation, dilation, and shear along the surface tangent direction, which is perpendicular to the surface normal. Given the hippocampal tube-like shape, its atrophy and enlargement directly affect the distance from each surface point to its medial core (analogous to the center line in a tube). This distance is called the radial distance of a hippocampal surface. Radial distance mainly describes morphometric changes along the surface normal direction and has been applied in many subcortical studies [85, 99, 184-186]. Thus, these two statistics are complementary to each other and their combination may boost the statistical power to study surface morphometry [27]. As introduced in Sec. 2.3.2, mTBM is a 3×1 vector on each surface point. Hippocampal radial distance is a scalar function. The new multivariate surface morphometry statistic was formed as a 4×1 vector on each surface vertex and the Hotelling's T^2 test (Sec. 2.2.5) was applied on the new statistic. Permutation test (Sec. 2.3.4) was used to perform group comparison and correct for multiple comparisons. The overall significance of the map is defined as the probability of finding, by chance alone, a statistical map with at least as large a surface area beating the predefined statistical threshold of $p = 0.05$. This omnibus p-value is commonly referred to as the overall significance of the map (or the features in the map), corrected for multiple comparisons. It basically quantifies the level of surprise in seeing a map with this amount of the surface exceeding a predefined threshold, under the null hypothesis of no systematic group differences. The permutation test on the overall rejection areas is used to evaluate the significance of overall experimental results and correct the overall significant *p*-values for multiple comparisons.

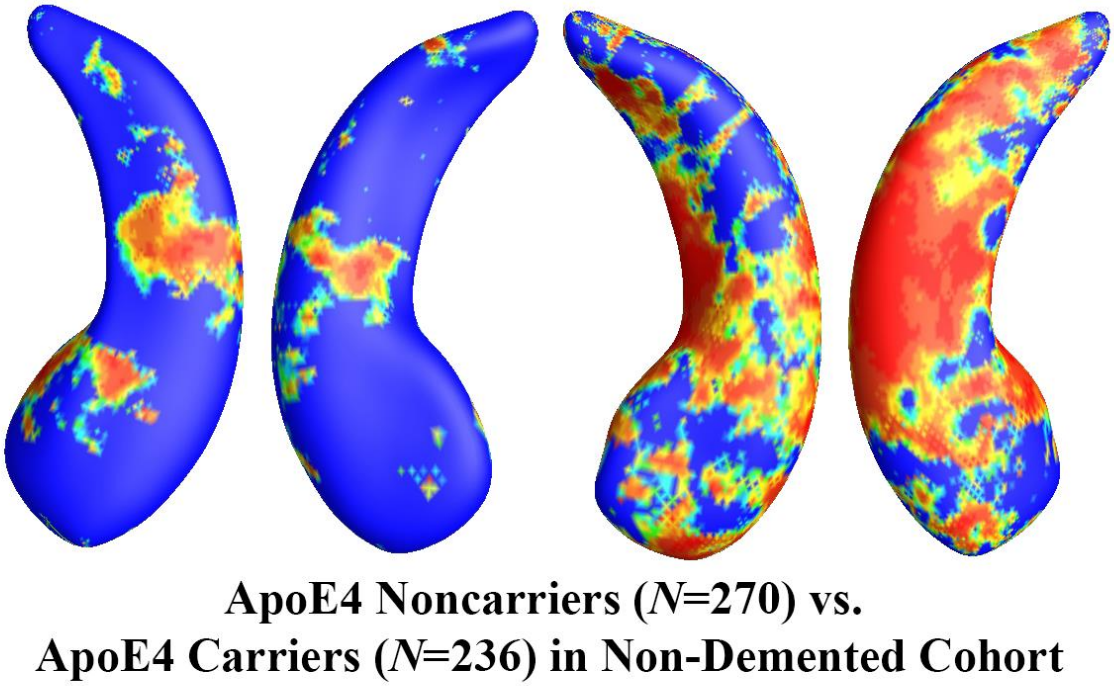

Figure 2.9. Illustration of local shape differences (*p*-values) between the ApoE4 noncarriers ($\epsilon 3/\epsilon 3$, $N = 270$) and carriers ($\epsilon 3/\epsilon 4$ and $\epsilon 4/\epsilon 4$, $N = 236$) in the non-demented cohort (MCI and controls). Non-blue colors show vertices with significant differences, at the predefined 0.05 level, uncorrected. The overall significance after multiple comparisons with permutation test is $p < 0.0027$.

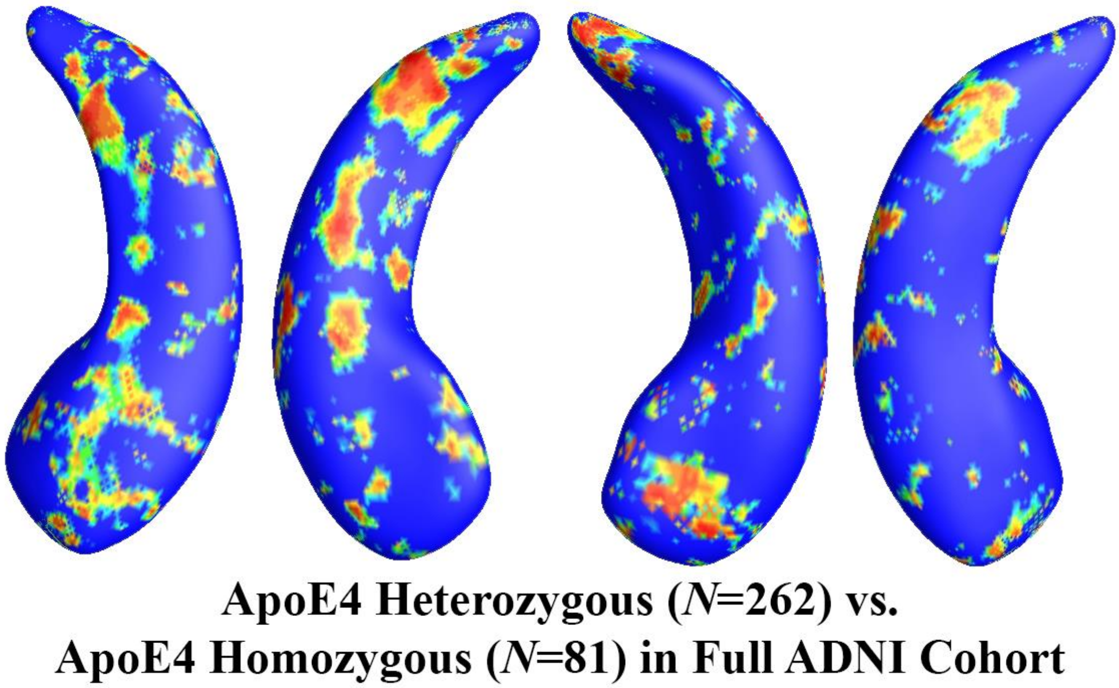

ApoE4 Heterozygous (*N*=262) vs.
ApoE4 Homozygous (*N*=81) in Full ADNI Cohort

Figure 2.10. Illustration of local shape differences (*p*-values) between the heterozygous ApoE4 carriers ($\epsilon3/\epsilon4$, $N = 262$) and the homozygous ApoE4 carriers ($\epsilon4/\epsilon4$, $N = 81$) in the full ADNI cohort. Non-blue colors show vertices with significant differences, at the predefined 0.05 level, uncorrected. The overall significance after multiple comparisons with permutation test is $p < 0.0129$.

Effects of ApoE4 Genotype. To explore whether the presence of the ApoE4 allele is associated with greater hippocampal atrophy, two experiments were conducted to study the effects of ApoE4 genotype on hippocampal morphometry in two populations:

(1). ApoE4 carriers versus noncarriers in the full ADNI cohort;

(2). ApoE4 carriers versus noncarriers in the non-demented cohort.

Here the ApoE4 noncarriers are those subjects who are homozygous noncarriers ($\epsilon3/\epsilon3$). Subjects with one $\epsilon2$ allele, i.e., $\epsilon2/\epsilon3$ and $\epsilon2/\epsilon4$ were excluded due to the possible protective effect of $\epsilon 2$ allele for AD [99]. In the 725 subjects of known ApoE4 genotype, there were 322 noncarriers (all homozygous for ApoE $\epsilon 3$) and 343 ApoE4 carriers. The non-demented cohort consisted of 506 subjects who were either MCI or control subjects, including 270 $\epsilon 4$ noncarriers and 236 $\epsilon 4$ carriers. Figure 2.8 shows the statistical p-map for the full ADNI cohort ($N = 665$; 322 noncarriers and 343 carriers). Non-blue colors show vertices with statistical differences at the predefined 0.05 level, uncorrected for multiple comparisons. As shown in figure 2.8, the ApoE4 carriers differed significantly from the noncarriers ($p < 0.0002$). Figure 2.9 shows the p-map for the non-demented cohort ($N = 506$; 270 noncarriers and 236 carriers). After correcting for multiple comparisons, the difference remained highly significant ($p < 0.0027$).

ApoE4 Dose Effects: Difference Comparison Between Heterozygous and Homozygous ApoE4 Carriers. To explore whether ApoE4 allele dose affects hippocampal surface morphometry and how this atrophy is related to normal aging, hippocampal morphometry between persons homozygous for the ApoE4 allele and those heterozygous for this allele was studied. The group differences between heterozygous and homozygous ApoE4 subjects in the full ADNI cohort, and in the non-demented ApoE4 carrier cohort, were analyzed. Among the ApoE4 carriers, 81 subjects were homozygous ($\epsilon 4/\epsilon 4$) and 262 were heterozygous ($\epsilon 3/\epsilon 4$) for ApoE4 allele. Figure 2.10 shows the statistical p-map for all ApoE4 subjects. The $\epsilon 4$ heterozygotes differed significantly from the $\epsilon 4$ homozygotes ($p < 0.0129$ after multiple comparisons correction with the permutation test). Excluding those ApoE4 carriers in the AD group, the non-demented ApoE4 carrier group consisted of 189 $\epsilon 4$ heterozygotes and 47 homozygotes. Figure 2.11 shows the statistical p-map for non-demented ApoE4 carriers. However, after correcting for multiple comparisons, the effect was not significant ($p < 0.142$). (There may be some subthreshold difference for the right hippocampus, but a larger sample size would be needed to detect it, if present.)

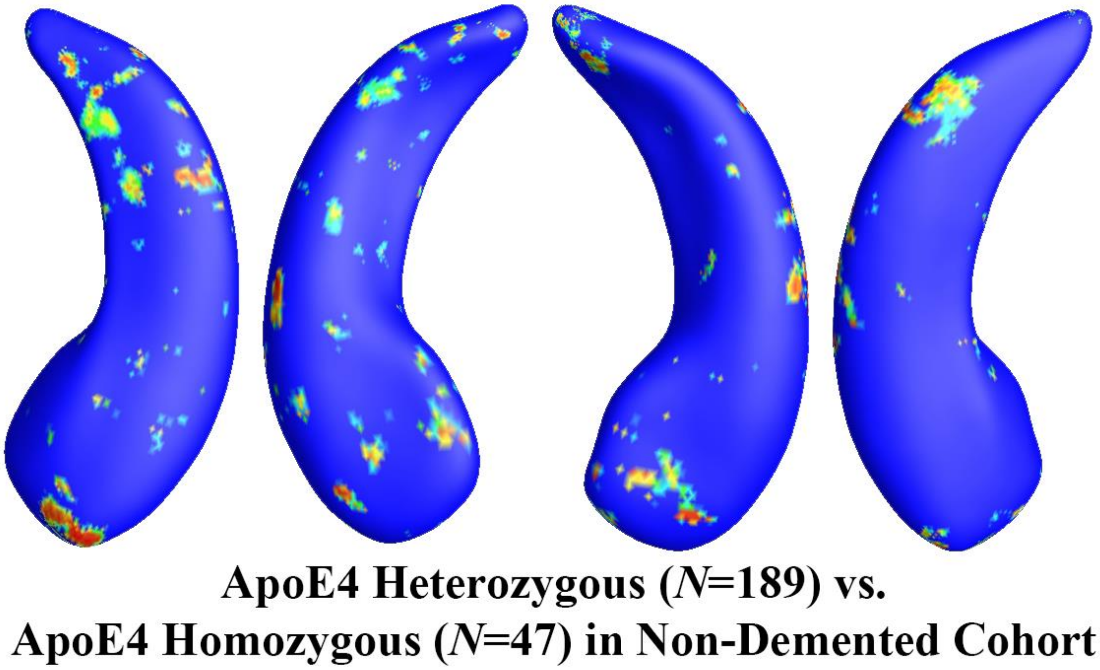

Figure 2.11. Illustration of local shape differences (p-values) between the heterozygous ApoE4 carriers ($\epsilon3/\epsilon4$, $N = 189$) and the homozygous ApoE4 carriers ($\epsilon4/\epsilon4$, $N = 47$) in the non-demented cohort. Non-blue colors show vertices with significant differences, at the predefined 0.05 level, uncorrected. The overall significance after multiple comparisons with permutation test is $p < 0.142$.

ApoE4 Dose Effects: Difference Comparison Between ApoE4 Noncarriers and Carriers with Different ApoE4 Dose. To further study the ApoE4 dose effects, the subjects were divided into three groups, ApoE4 homozygotes, heterozygotes, and noncarriers. We performed group difference analysis between two groups and compared the statistical power. The hypothesis was that morphometric differences would be greater in ApoE4 homozygotes than heterozygotes, who would in turn show greater deformities compared to $\epsilon 4$ noncarriers. Figures 2.12 and 2.13 show how ApoE4 noncarriers differ in hippocampal shape from ApoE4 heterozygotes and homozygotes in the full ADNI cohort and the non-demented cohort, respectively. Figure 2.12 shows the statistical *p*-map for the full ADNI cohort. Non-blue colors show vertices with statistical differences, at the predefined 0.05 level, uncorrected. As shown in figure 2.12 (a), the ApoE4 heterozygotes differed from $\epsilon 4$ noncarriers ($p < 0.0031$). Figure 2.12 (b) shows the statistical *p*-map for the full ADNI cohort and demonstrates that the ApoE4 homozygotes differed from $\epsilon 4$ noncarriers ($p < 0.0001$). Figure 2.12 (b) also shows more extensive statistically significant areas of difference than those in figure 2.12 (a), for both the left and right hippocampal surfaces. After excluding AD subjects from these three groups, the group difference analysis was repeated among ApoE4 noncarriers ($\epsilon 3/\epsilon 3$, $N = 270$), $\epsilon 4$ heterozygotes ($\epsilon 3/\epsilon 4$, $N = 189$), and $\epsilon 4$ homozygotes ($\epsilon 4/\epsilon 4$, $N = 47$). Figure 2.13 (a) shows the statistical *p*-map for the non-demented cohort [$N = 459$; 270 noncarriers ($\epsilon 3/\epsilon 3$) and 189 ApoE4 heterozygous carriers ($\epsilon 3/\epsilon 4$)]. The ApoE4 heterozygotes differed from the $\epsilon 4$ noncarriers ($p < 0.017$). Figure 2.13 (b) shows the *p*-map for the non-demented cohort [$N = 317$; 270 noncarriers ($\epsilon 3/\epsilon 3$) and 47 ApoE4 homozygous carriers ($\epsilon 4/\epsilon 4$)] and shows that the ApoE4 homozygotes differed from the $\epsilon 4$ noncarriers ($p < 0.006$). Similar to figure 2.12, the homozygous vs. noncarriers comparison showed more extensive areas of difference in the uncorrected *p*-maps. In figure 2.14, the CDFs of the *p*-values observed for the contrast of ApoE4 carriers versus noncarriers are plotted against the corresponding *p*-value that would be expected, under the null hypothesis of no group difference, for the four experiments shown in figures 2.12 and 2.13. For null distributions, the cumulative distribution of *p*-

values is expected to fall approximately along the dotted line. Large deviations from that curve are associated with significant signal, and greater effect sizes represented by larger deviations. Note that the deviation of the statistics from the null distribution generally increases from heterozygotes vs. noncarriers to homozygotes vs. noncarriers in both the full ADNI cohort and non-demented cohort studies. As such, although more rigorous statistical tests are certainly necessary, from the *p*-maps and CDF plots, the trend can be observed that in all groups, ApoE4 homozygotes appear to differ more from noncarriers than do $\epsilon 4$ heterozygotes, suggesting a clear ApoE4 dose effect.

2.4 Discussion

This study has two main contributions. First, a subcortical structure surface morphometry system was built with conformal parameterization and 2D inverse consistent image fluid registration. Pioneering work [28, 58] in brain surface registration proposed a cortical pattern matching algorithm to register cortical surfaces by computing a flow field in the cortical parameter space, which matches up corresponding sulci (represented as a set of landmark curves). With surface conformal parameterization [131], here we show how the image fluid registration method may be adjusted to enforce appropriate surface correspondences in the parameter domain. Novel surface features, surface conformal representation, were proposed to guide the fluid flow to register subcortical surfaces. The surface conformal representation captures both intrinsic surface feature, i.e. conformal factor and extrinsic surface feature, i.e. mean curvature. The surface conformal parameterization was computed by solving a linear system [131] so the system is computationally efficient and scalable. Furthermore, due to the simplicity of the

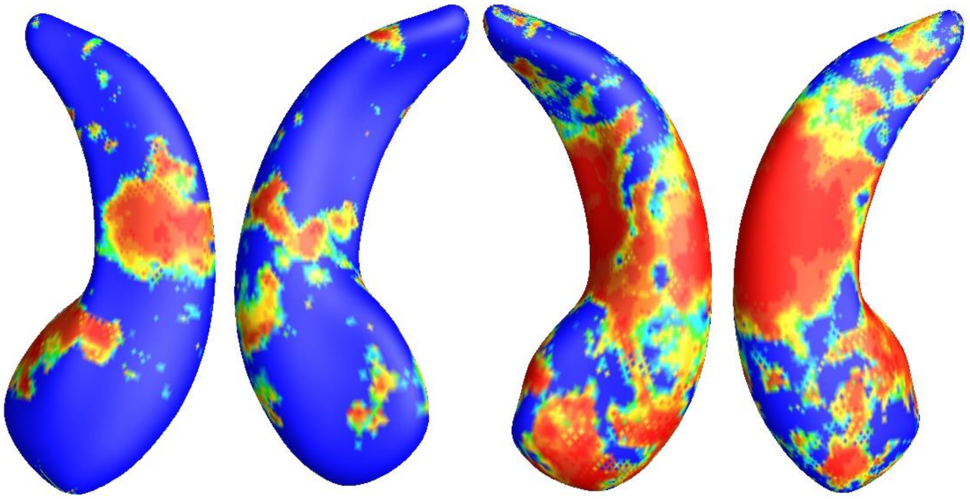

(a) ApoE4 Noncarriers (*N*=322) vs.
ApoE4 Heterozygous (*N*=262) in Full ADNI Cohort

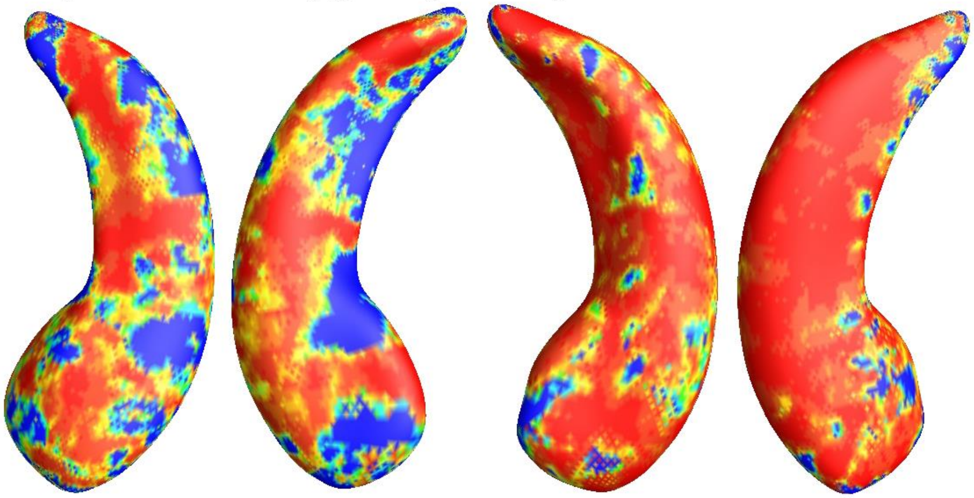

(b) ApoE4 Noncarriers (*N*=322) vs.
ApoE4 Homozygous (*N*=81) in Full ADNI Cohort

Figure 2.12. Illustration of local shape differences (p-values) between the ApoE4 noncarriers ($\epsilon3/\epsilon3$, $N = 322$) and heterozygous carriers ($\epsilon3/\epsilon4$, $N = 262$; a), between the ApoE4 noncarriers ($\epsilon3/\epsilon3$, $N = 322$) and homozygous carriers ($\epsilon4/\epsilon4$, $N = 81$; b), in the full ADNI cohort. Non-blue colors show vertices with significant differences, at the predefined 0.05 level, uncorrected. The overall significances after multiple comparisons with permutation test are $p < 0.0031$ for (a) and $p < 0.0001$ for (b).

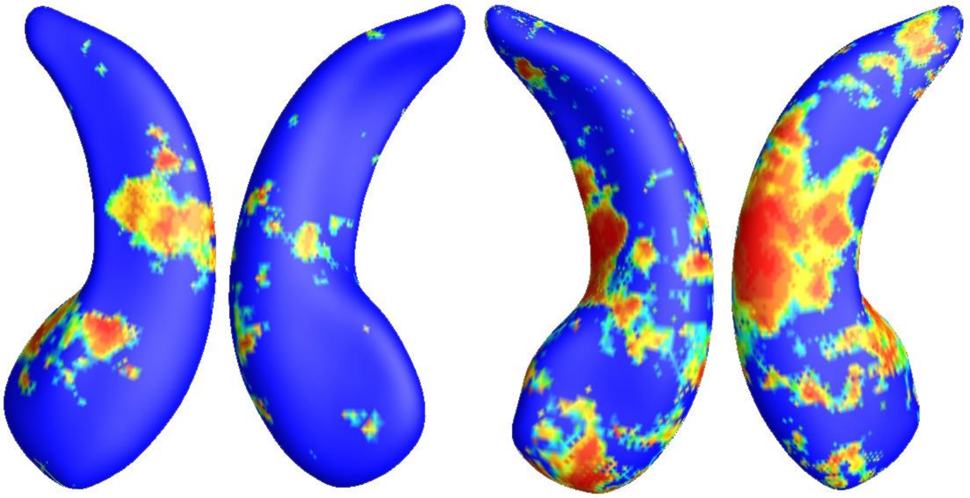

**(a) ApoE4 Noncarriers (*N*=270) vs.
ApoE4 Heterozygous (*N*=189) in Non-Demented Cohort**

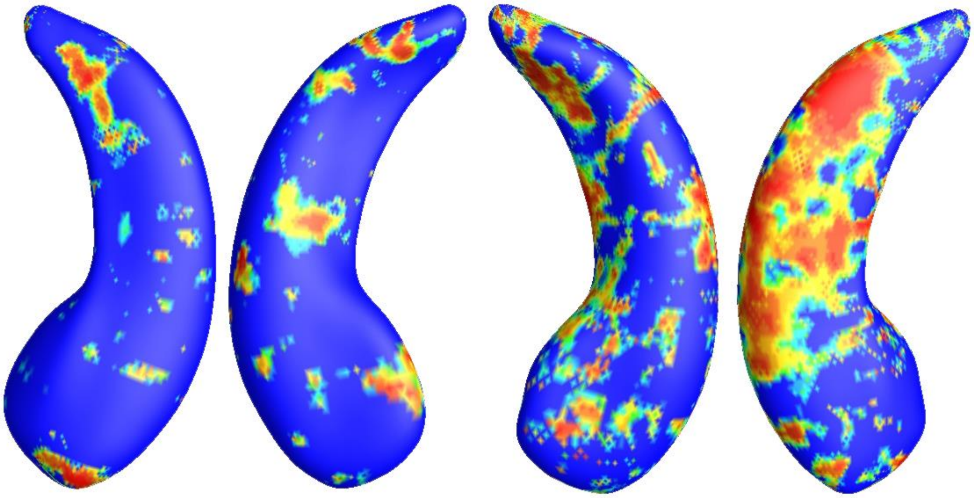

**(b) ApoE4 Noncarriers (*N*=270) vs.
ApoE4 Homozygous (*N*=47) in Non-Demented Cohort**

Figure 2.13. Illustration of local shape differences (p-values) between the ApoE4 noncarriers ($\epsilon 3/\epsilon 3$, $N = 270$) and heterozygous carriers ($\epsilon 3/\epsilon 4$, $N = 189$; a), between the ApoE4 noncarriers ($\epsilon 3/\epsilon 3$, $N = 270$) and homozygous carriers ($\epsilon 4/\epsilon 4$, $N = 47$; b), in the non-demented cohort. Non-blue colors show vertices with significant differences, at the predefined 0.05 level, uncorrected. The overall significances after multiple comparisons with permutation test are $p < 0.017$ for (a) and $p < 0.006$ for (b).

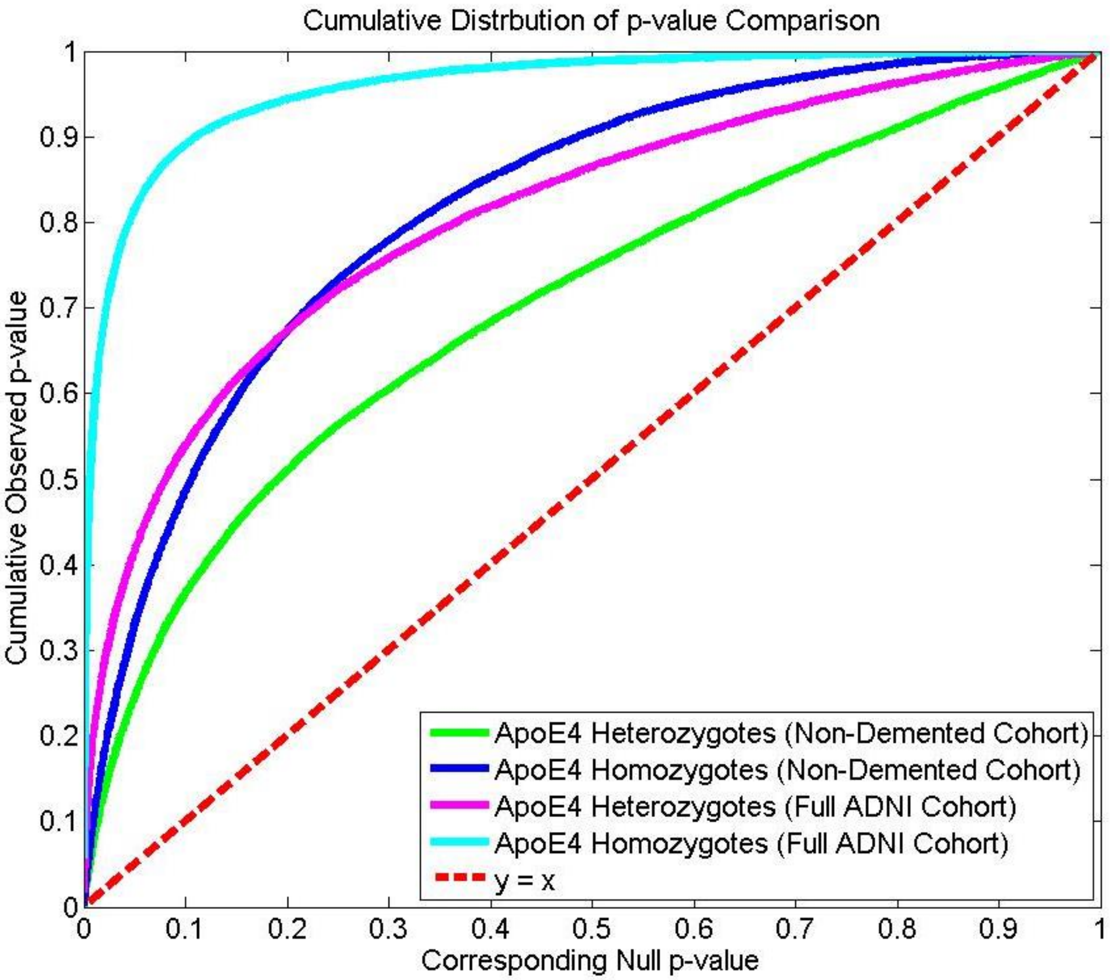

Figure 2.14. Illustration of cumulative distribution functions of the *p*-values observed for the contrast of ApoE4 carriers versus noncarriers, plotted against the corresponding *p*-value that would be expected under null hypothesis of no group difference, for the four experiments shown in figures 2.12 and 2.13. We note that the deviation of the statistics from the null distribution generally increases from heterozygotes vs. noncarriers to homozygotes vs. noncarriers in both the full ADNI cohort and non-demented cohort studies, suggesting that the ApoE4 allele dose may be associated with more accelerated atrophy of hippocampus.

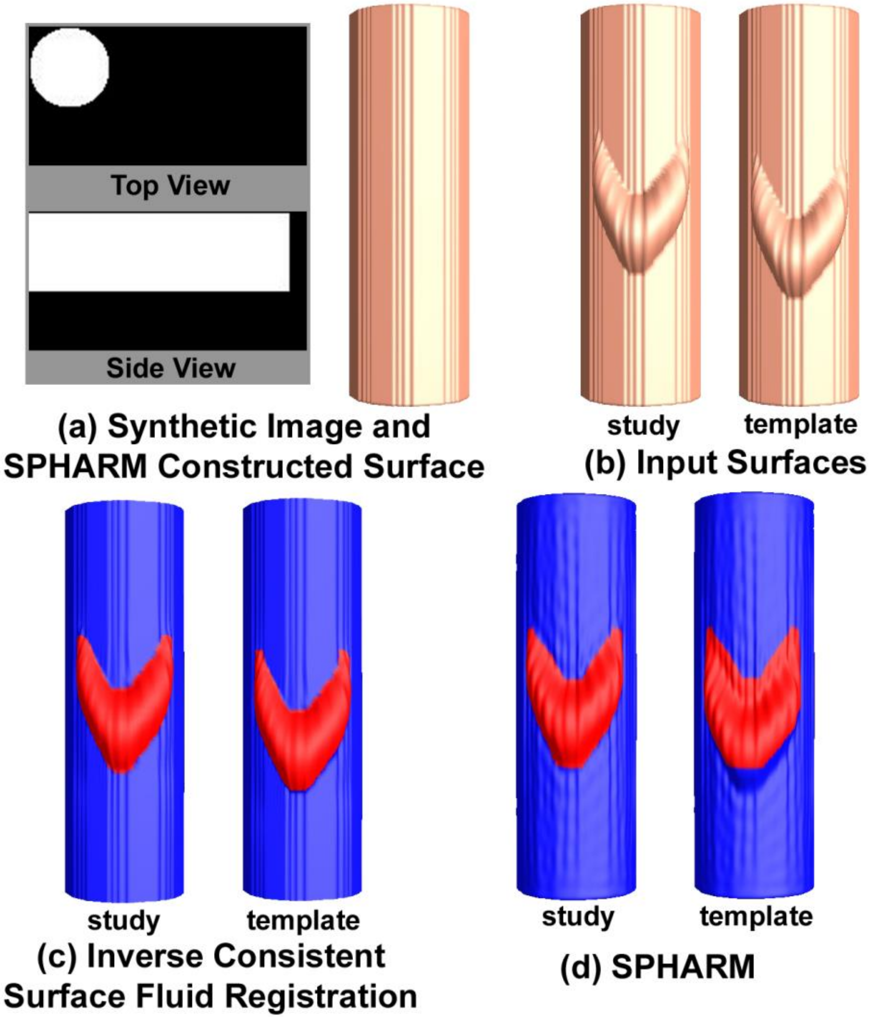

Figure 2.15. Comparison of surface fluid registration and SPHARM on synthetic surfaces. (a) is the synthetic volumetric image for a cylinder and its surface model constructed with SPHARM tools. (b) shows the surfaces on which two synthetic C-shapes were put at different locations. (c) and (d) illustrate the surface registration achieved by proposed method (c) and SPHARM method (d). To show the registered correspondence, the C-shape was drawn on the study surface with red color and the color was directly transferred to the template surface. In (c) the C-shape on template surface is in red while in (d), the red color does not totally cover the C-shape. This simple experiment shows that the new method registers surface by matching detailed surface features.

Riemannian metric introduced by conformal parameterization, extension of Navier-Stokes equation into general surface space is easy to implement and thus avoids rather complicated Christoffel symbol computation [28]. The registration software package together with the multivariate statistic package are publically available at [187]. Second, in an open brain imaging dataset, ADNI, we demonstrated ApoE4 is associated with greater atrophy of hippocampal formation in the non-demented baseline cohort. This work outperformed the results of a prior work [107] on the same dataset and also validated the observations in [181] in a much larger imaging dataset. The results are related to the preclinical stage AD, a concept that has been validated through autopsy studies [188-192], fluorodeoxyglucose positron emission tomography (FDG-PET) studies [193, 194] and amyloid ligand binding studies [195] based on the use of Pittsburgh Imaging Compound B (PiB). The proposed work may provide a structural MRI analysis tool that helps study large numbers of genetically at-risk individuals before the onset of symptomatic memory impairment.

Comparison with SPHARM on synthetic models. The main advantage of the new algorithm is the ability to register surface features via a diffeomorphic mapping while preserving the surface topology. To validate the idea, a synthetic experiment was conducted to compare the proposed method with SPHARM given that the source code of SPHARM is available online. First, a binary volumetric image of a cylinder (figure 2.15 (a)) was generated. The SPHARM image segmentation and surface construction tool generated the surface model (figure 2.15 (a)). Then, a C-shape was added on the cylinder model at two different locations to simulate the region of interests (ROI) on different surfaces (figure 2.15 (b)). The combination of the C-shape and the cylindrical surface did not change the vertex number, face number, and connectivity of the original cylindrical surface. Note some staircase effect on the surfaces in figure 2.15 (b) was introduced from the SPHARM surface construction tool. For a fair comparison, these two surfaces were applied as the input for both SPHARM and the inverse consistent surface fluid registration. As shown in figure 2.15 (c) and (d), the resulting SPHARM surfaces were reconstructed from the spherical harmonic coefficients, which were computed from the input surfaces and their spherical parameterizations. To show the registration results, we drew the ROI on the study surface with red color and the rest area with blue color. All the color setting was transferred to the template surface via the registration. Presumably, a good registration result will have a clear C-shape (i.e. the ROI) drawn in the red color. In figure 2.15 (d), it can be seen that the resulting C-shape is not totally in red, which indicates that the two ROIs were not well aligned. We also see that some surface features were lost or altered during the reconstruction. On the other hand, as shown in figure 2.15 (c), the C-shape on the template surface is clearly in red and the rest in blue, which indicates that the proposed method was able to well register the regions of interest and keep the surface topology as well. The staircase effect of the input surfaces was well retained in our results. This simple experiment may demonstrate that the new method can register surfaces by matching surface features, such as curvature or conformal factor.

Comparison of the inverse consistent fluid registration with/without area distortion correction on synthetic surfaces. The inverse consistent surface fluid registration method involves solving the Navier-Stokes equation on general manifold. It requires the comparison of vectors at different points on the surface. In general, these vectors are in different tangent planes and a way is needed to compare them in a common space [141]. On the other hand, parametric surfaces allow tangent vectors to be compared in their parameter domains. To do that, one needs formulate the distortions caused by the surface parameterizations and remedy them by some compensation terms, so we can achieve a set of coordinate invariant differential operators [28, 131, 140, 141]. Compared with the relatively complicated area distortion compensation terms adopted by some prior work [28, 141], the global conformal parameterization allows a simple formulation using the conformal factor [131, 140]. In computer graphics literature (e.g. [141]), it has been observed that the fluid simulation artifacts were drastically reduced when these compensation terms were applied. To validate if the compensation terms help improve surface registration quality, two experiments were performed on the synthetic surface models that have been used in figure 2.5. In this experiment, the inverse consistent surface fluid registration on both directions was applied to register surface 1 to surface 2 (the first row in figure 2.16) and surface 2 to surface 1 (the second row in figure 2.16). The registration has been performed with and without the parameterization compensation terms. The pull-back metrics were visualized by drawing equal-spaced black strips defined on the target surfaces back to the source surfaces based on the registration. It is obvious that the registration results with the area distortion correction ((c) and (d)) have more uniform strips than those without the area distortion correction ((e) and (f)). Similar to prior work [28, 131, 140, 141], this simple example may help justify the new formulation and demonstrate its efficacy to produce a good surface correspondence.

ϵ-Isometric parameterization vs. conformal parameterization. Mathematically speaking, an isometric mapping between two surfaces requires that the first fundamental forms to be equivalent throughout the surfaces whereas a conformal mapping only requires the first fundamental forms to be different by a scalar. As a result, the conditions for

conformal mapping are relatively loose. Similar to the cartography problems, it is impossible to compute a mapping from the hippocampal surface to a Euclidean plane that preserves all the geodesic distances. This is a consequence of the theorema egregium [71]: because the Gaussian curvature of the hippocampal surface is nonzero on most of surface areas, whereas the plane has zero curvature, these two surfaces cannot be isometric.

Figure 2.16. Comparison of the inverse consistent surface fluid registration with and without the area distortion correction term in Eq. 2.5. The pull-back metrics are visualized by drawing equal-spaced black strips defined on the target surfaces back to the source surfaces. Overall the registration results with the area distortion correction ((c) and (d)) are more uniform, i.e. less drastic area distortion strips, than the ones without the area distortion correction ((e) and (f)).

In computer graphics and computer vision fields, there are numerous methods proposed to compute the ϵ-isometric parameterization, i.e. an approximation of isometric mapping, e.g. some methods [72, 73] apply a multidimensional scaling method [196-199] to compute the near-isometry mapping to the plane for retinotopic mapping and 3D face recognition study.

On the other hand, conformal parameterization was adopted in various imaging and graphics applications to study surface registration [2, 200, 201]. Because of the uniformization theorem, conformal mappings to certain domains exist on every simply connected Riemann surface. The discrete conformal mapping has a rigorous theoretic definition and can be computed accurately. In this study, there exists a conformal mapping from a hippocampal surface with two introduced cuts to the Euclidean plane. Prior work [131] introduced a holomorphic 1-form based method to compute such a conformal mapping. Although there are area distortions on a conformal mapping, considering the definition of conformal factor λ as Eq. 2.2, it can be seen that conformal factor is a smooth function which describes the stretching effect of conformal parameterization. With the conformal factor as the compensation term, the major novelty of this work is to introduce the Navier-Stokes equation for Riemann surface by the covariant derivatives. Specifically, in Eq. 2.5, by dividing the conformal factor λ, the flow induced in the parameter domain is adjusted for the area distortion introduced by the conformal parameterization and one may achieve a coordinate invariant PDE solving formulation. The proposed formulation is simpler than prior work [28, 58] and may offer a numerically stable and efficient method for surface registration problem.

Comparison with isometry-based surface registration methods. Many existing isometry-based algorithms have focused on mappings of surfaces to their flattened ones on the Euclidean plane [202-205]. Some research also tried to enforce either distance preserving or near-isometry in the surface registration work [111, 206, 207]. Among them, Cho et al. [111] proposed a multi-resolution distortion-minimizing mapping scheme to compute surface correspondence between subcortical surfaces. The same research problem that we are trying to address may justify the effort to briefly compare this work with their work.

In [111], although they do not map a hippocampal surface to the Euclidean plane, they employ an area-preserving approximation spherical parameterization method [208] to establish an initial surface alignment and, in each iteration, generalize the mapping from the low resolution meshes to high resolution meshes. In the registration step, they formulate the matching problem as an energy minimization problem that is defined on a high-dimensional Riemannian manifold and penalizes the deviation from isometric mapping and triangle flippings. The surface deformation is constrained to move along the source surfaces. Our work formulates the surface registration as an image flow problem so that a 3D registration problem is converted to a 2D one via the conformal parameterization. Because of the nature of 2D image registration, this work is more intuitive and easier to be visualized. Due to the differential covariants, this work compares vector fields and deforms surfaces on their tangent planes and also deforms surfaces on surfaces themselves (both source and target surfaces). Furthermore, the inverse consistent registration framework helps maintain a symmetric correspondence and does not depend on the order people use to compare surfaces. Overall, these two systems take two different approaches, i.e. one projects the matching problem to a high-dimensional Riemannian manifold and pursues an approximated isometry deformation while the other converts the problem to the 2D image plane and solves it with some stable 2D image registration schemes. Although a quantitative comparison may be of interest for future work, two algorithms are comparable and complementary to each other. People may expect one method outperforms the other in some contexts but not others, or in some diseases but not others, depending on the type of surfaces to be registered.

Benefits of conformal parameterization. For surface morphometry study, one traditional way to do this is to set up parametric grids on surfaces, which are registered across subjects, and then use differential geometry to come up with useful descriptors of surface features of interest, or to summarize the geometry as a whole. Conformal maps help to induce particularly well-organized grids on surfaces. This simplifies a number of downstream computations of registration and surface metrics. The major benefits of conformal parameterization in the proposed method include: (1) a good initialization alignment. For two similar shapes, their conformal structures are also similar. As a result, the conformal parameterization provides good initial alignments between hippocampal surfaces which are similar in nature; (2) surface conformal representation. It represents both surface intrinsic and extrinsic geometry features; (3) an efficient numerical scheme to solve PDEs on general surfaces. It simplifies the extension of PDEs such as Navier-Stokes equation, to general surface and avoids complicated Christoffel symbol computation [28]. The proposed method pursues an inverse consistent registration so the PDEs need to be solved multiple times. Therefore, the computational efficiency introduced by the conformal parameterization may help achieve an efficient and stable solution for surface morphometry study.

System structure design. As a shape analysis software tool, the input to the proposed system is binary images, which are obtained either by some automatic image segmentation tools [162, 209] or manual segmentation results using some interactive graphic tools [210, 211]. In the current study, the input was chosen as the automatic segmentation results by FIRST [162]. The binary images were generated by thresholding the segmentation results and surface models were built for the subsequent surface morphometry analysis. Note other options are also available for such a morphometry system. For example, the FIRST software tool (http://fsl.fmrib.ox.ac.uk/fsl/fslwiki/FIRST) generated both images and surface models of subcortical structures. The surface models obtained by FIRST already had cross-subject correspondences and were used in this study as a comparison method. Whether or not the integrated system provides superior discrimination power than the one working with binary images still needs more validation. However, the benefit of current system design is the flexibility for users to adapt the system to different data sources. Furthermore, similar to some other work that used FIRST segmentation results to study relative pose information of subcortical nuclei [212], our software tool may also be interesting to FIRST users so that it may be appealing to a broader range of researchers in the neuroimaging community.

Alternative pipeline consideration. Since the initialization is affected by the mapping, so one may wonder whether it is possible to use a least metric distortion mapping for initialization and then conformal mapping for the fluid flow. The alternative pipeline is appealing but it has some difficulties. Firstly, in this work, similar to M-reps or *cm-rep* work [184, 213], a cylindrical parameterization for the hippocampus [27, 79] is used. Under this setting, it is rare to have two conformally equivalent hippocampal surfaces (i.e. there is a conformal mapping between them) because of the biological variety. As a result, the fluid flow does not generate a conformal mapping in general. Secondly, it is a common belief that a least metric distortion mapping, either defined by explicitly defined landmarks or implicit geometry features, could align anatomical surface for neuroanatomy analysis because functional and architectonic boundaries of the human brain have been linked to the brain structure shapes [214]. So for the current approach, to use conformal parameterization for initial alignment and refine it with least metric distortion mapping, is indeed a valid and practical approach.

Initial alignment computation. The initial alignment is important for the success of the proposed surface registration algorithm. Numerous efforts are taken to guarantee good initial alignments between surfaces to be registered. Firstly, all input data has been registered to the MNI standard space, where all the surfaces have the same orientation. Secondly, two consistent landmark curves are labeled at the front and back of the hippocampal surface, representing its anterior junction with the amygdala, and its posterior limit as it turns into the white matter of the fornix. They are biologically valid and consistent landmarks across subjects. Given the hippocampal tube-like shape, these landmark curves can be automatically detected by checking the extreme points by searching along the first principle direction of geometric moments of surface [27, 155, 156]. For the quality control purpose, the consistency of all landmark positions has been manually checked in this work. Lastly, the surfaces are parameterized to a rectangle by tracing a constant line (iso-u) on the parameter domain. The cutting curve is guaranteed to pass a geometrically consistent point, e.g. the extreme point on x direction in the MNI standard space. Because the conformal structure is surface intrinsic feature and all hippocampal surfaces have similar shapes, their conformal parametrizations are very similar on the 2D plane. Take the parameterization as the canonical space, the initial alignment is established between hippocampal surfaces.

Global affine normalization. In computational neuroanatomy research, brain images are usually transformed into a standardized stereotactic space via a global affine transformation followed by a nonlinear deformation to match the atlas or template, which is a fixed reference coordinate system of the brain. The global affine normalization removes most of the within- and between-subject global differences in brain size. Because global brain size difference does not provide much biological information, these global morphological variabilities should be removed before any localized shape analysis is performed [215]. It is a common practice for tensor-based morphometry (TBM) research [27, 29, 32, 79, 80, 120]. In this work, after segmentation, the segmented hippocampal models were transformed into MNI standard space with the transformation matrices computed by FLIRT. Since the parameterization space is used as a common space for registration, this global affine normalization does not affect the registration. The normalization is purely for the following mTBM analysis. It may affect the area or the deformation tensor computation but, by removing the global differences in brain sizes, it provides a stable reference space for hippocampal subfield analysis.

Area distortion compensation and registration regularization terms. There are several coefficients in the proposed formulation (Eqs. 2.6, 2.7 and 2.8). Among them, $\lambda_{f,b}$ are conformal factors and used as the area distortion compensation terms for parametric surface based PDE solving. α, μ and τ are registration regularization terms. Although they are all involved in surface registration, they have different functions. As discussed above,

$\lambda_{f,b}$ mainly help achieve coordinate invariant differential operators so that one may solve surface fluid PDEs with parametric surfaces. The benefits to have $\lambda_{f,b}$ are not to achieve an area preserving mapping between 3D surface and parameter domain, instead, they are used to define partial differential operators on manifolds and the covariant differentiation on tensor fields [71]. With conformal parameterization, their computation becomes very simple and is only related to conformal factors, $\lambda_{f,b}$. On the other hand, similar to prior work [114, 115], α, μ and τ are registration regularization terms which controls the distortion introduced during the fluid registration. With different settings on these parameters, one may penalize the induced area distortion or enforce smoothness. With these two different regularization terms, the surface fluid registration framework is aimed to achieve a surface registration framework which is both computationally efficient (induced by the conformal parameterization) and produces diffeomorphic surface mappings with controlled distortion (enforced by registration regularization terms).

Inverse consistency for a loss of alignment accuracy? In this work, inverse consistency is imposed as a constraint. At the initialization, both the forward and backward maps are set as identity maps. They are inverse consistent for sure. But the sum of squared intensity differences (SSD) between the two different images that to be registered will make the whole energy too large to be optimal. Then by changing the forward and backward maps, we gradually reduce the SSD while keeping the inverse consistency of the two maps until the energy cannot be decreased anymore. Here the inverse consistency constraint may even improve the accuracy of the alignment because the two images deform to each other, thus the driving force computed by SSD between them may lead the flows to get more accurate alignments. In summary, besides the fact that it helps a diffeomorphic and balanced surface registration, the inverse consistency does not necessarily sacrifice surface registration accuracy.

Conformal equivalence and conformal factor update. The final deformed map is obtained by first conformally mapping a surface to the parameter domain and second deforming to a template surface by the inverse consistent fluid registration. The former is a conformal mapping and the latter is not a conformal mapping. Since conformal mapping and fluid registration generate diffeomorphic mappings, the surface-to-surface mapping established by the proposed method is a deffeomorphic mapping but usually is not a conformal mapping. To achieve conformal mappings between hippocampal surfaces, the two surfaces have to be conformally equivalent. Generally speaking, two hippocampal surfaces may not be conformally equivalent after introducing the cuts so the conformal mappings do not always exist. However, subtle surface differences may be detected by studying the conformal structure quotient space - Teichmüller shape space as demonstrated in prior work [45, 46].

As a surface intrinsic feature, the conformal factor is computed after getting the parameterization of the surface and is not adjusted as the map changes. This correction term for fluid registration could make the flow computed in the parameter domain independent of underlying surface metrics, thus the flow directly establishes a mapping between surfaces.

Does the surface smoothing distort the original surfaces? To reduce the noise in MR image acquisition and overcome the partial volume effects, as well as reduce the number of obtuse triangles for surface parameterization, a smoothing process was applied on all the hippocampal surfaces. Many mesh smoothing algorithms have been proposed. In

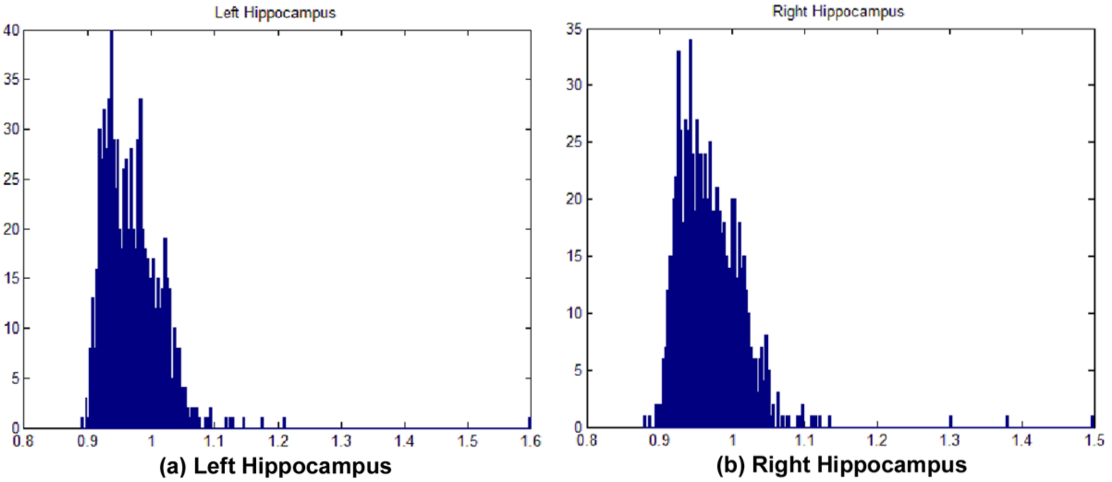

(a) Left Hippocampus **(b) Right Hippocampus**

Figure 2.17. Histogram showing the Hausdorff distances between the smoothed meshes and original meshes. The majority of the absolute distances fall into the range [0.9, 1.1] with the unit as millimeter. Given the volumes of hippocampus lie between 3000 and 4000 mm^3 [164, 216-218], the smoothed meshes can be regarded as accurate approximations of the original surfaces.

[219], Taubin proposed a simple, linear and isotropic method to improve the smoothness of a surface mesh. This method is fast because it does not rely on expensive functional minimizations. Some variants of this algorithm have also been developed [220, 221]. However, these techniques are isotropic, thus indiscriminately smooth noise and salient surface features. Recently, feature-preserving mesh smoothing methods [222-231] have also drawn more and more interests. In the proposed system, a two-step mesh smoothing method was applied to all the surfaces. The smoothing process consists of mesh simplification using “progressive meshes” [128] and mesh refinement by Loop subdivision surface [129]. All the hippocampal meshes were consistently smoothed by 5 iterations of mesh simplification using “progressive meshes” and Loop subdivision. In order to smooth

the surfaces while preserve surface features, the face numbers of the surfaces in each iteration were gradually increased. As a result, we obtained relatively smooth but accurate surfaces that are suitable for computing derivative maps. Figure 2.17 illustrates the histograms of the Hausdorff distances between the smoothed meshes and the original meshes for both the left and right hippocampi that were studied in this chapter. The figure shows that the majority of the absolute distances fall into the range [0.9, 1.1] with the unit as millimeter. Given the volumes of hippocampus lie between 3000 and 4000 mm^3 [164, 216-218], the smoothed meshes can be regarded as accurate approximations of the original surfaces. This method has been applied in many prior subcortical surface analysis studies [27, 79]. Empirically, a continuous subdivision and mesh simplification process will generally eliminate the obtuse angles and improve the mesh quality.

Does the cutting affect the statistics? To achieve an accurate registration between surfaces, we cut open two landmark curves and convert the landmark matching problem as an explicit boundary matching problem. This approach has been adopted in prior work on brain cortical surface registration [2] and subcortical surface registration [27]. The topology cuts do not change the overall surface geometry because the two sides of the cuts are still in the identical positions. So the cuts do not affect the surface registration and the following shape analysis work. Also since the conformal factor is used as the compensation term for the area distortion in the fluid registration framework, theoretically these cuts should not affect the statistical results on the neighboring regions. As shown in figure 2.18, the enlarged figures highlight the positions of the landmark curves and the insignificant regions on the *p*-map. It can be seen that the statistically insignificant area does not align exactly with the cutting positions. However, to achieve an accurate surface registration and morphometry analysis, the cut positions need to be consistent across subjects. Besides the automatic moment-based landmark curve identification method discussed in Sec. 2.3.2, we also applied a quality control step by manually checking all the cutting positions after the automatic landmark identification step. Although inconsistency was not found in this work, it is a recommended step when applying our pipeline for new analyses.

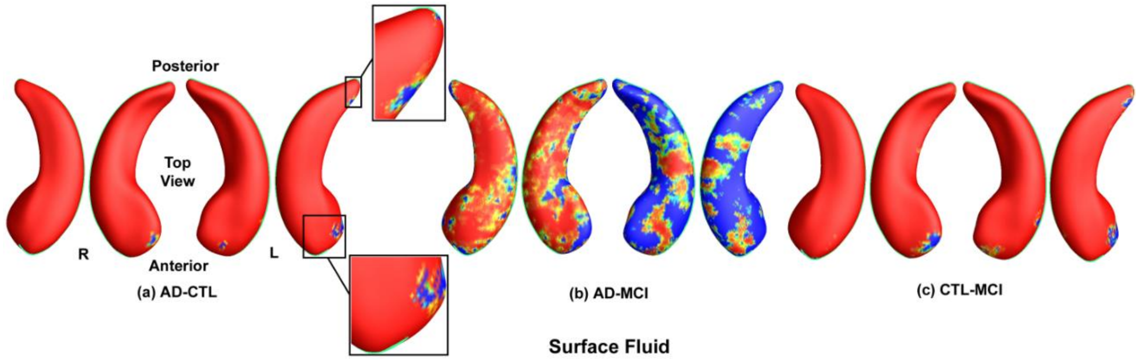

Figure 2.18. Positions of landmark curves and statistically insignificant regions on the *p*-maps of the inverse consistent surface fluid registration method. The statistically insignificant area does not align exactly with the cutting positions.

Visualization of the differences between groups. Here we mainly applied a nonparametric, multivariate permutation testing on Hotelling's T^2 statistics. Compared with the conventional Jacobian determinant [63, 103, 108, 109], the logarithmic transforms are applied to convert the tensors into vectors that are more tractable for Euclidean operations. On the other hand, standard multivariate random field theory may also be applicable to analyze the new multivariate statistics. For instance, in [232, 233], results based on random field theory for Roy's maximum root was proposed. The inference for Roy's maximum root is based on the Roy's union-intersection principle [234]. Recently, Chung et al. [235] used this statistic to quantify abnormal local shape variations of the amygdala in 22 high-functioning autistic subjects. Here since Hotelling T^2 test is used, the significant map results are like 2-sided tests and do not carry the direction information. To visualize the deformation directions, a new measurement [236] is defined at each vertex k as

$$R^k = \frac{\sum_i^{N_1} \det J_{1i}^k}{\sum_j^{N_2} \det J_{2j}^k} \frac{N_2}{N_1} \tag{2.12}$$

where J_{1i}^k and J_{2j}^k are the Jacobian matrices for the *i*th subject in one group and the *j*th subject in another group, respectively, and N_1 and N_2 are the number of subjects in one group and in another group. The determinant of Jacobian matrix indicates the difference in size of the region in the individual subject compared to the template. When registering the two groups of subjects to a common template, R^k with values greater than 1 indicating that the surface area at that vertex is larger in one group when compared to the other group and vice versa for values smaller than 1. Figure 2.19 shows that when comparing AD patients with healthy controls or MCI subjects and when comparing MCI subjects with healthy controls, as expected, the major area on the hippocampal surface shows atrophy, which is represented by the red color. This also matches the corresponding *p*-maps as shown in figure 2.6. Some enlargements are also observed at the anterior and the posterior sides of the surface, which are represented by blue color. As pointed out in [97], this is probably due to the tissue loss in the neighboring structures of hippocampus, as the anterior and posterior are the junctions with the amygdala and the white matter of the fornix, respectively. As a result, the enlargements may be caused by the shifting of the long axis of the hippocampus.

Clinical significance of surface-based morphometry statistics. Atrophy of brain structures is associated with cognitive impairment in normal aging and AD [86], and typically results from a combination of neuronal atrophy, cell loss, and impairments in myelin turnover and maintenance, and corresponding reductions in white matter volume. These cellular processes combine at the macroscopic level to induce observable differences on brain MRI. Several of processes (such as cellular atrophy) occur with normal aging, and others (including neuronal loss) are further promoted by amyloid plaque and neurofibrillary tangle deposition. This work applies mTBM, a surface-based morphometry feature, to study brain structure changes. Although surface expansion and contraction are less traditional measures of morphometry, it is likely that they simply reflect the same processes that cause progressive brain tissue loss. This work, as well as some approaches developed by other groups (e.g. [237, 238]), measure the extent and severity of cortical and hippocampal shape deformations as a proxy for cortical and hippocampal atrophy. The detected expansion or compression of the surface areas are associated with macrostructural and microstructural loss in different brain regions and their association with cognition and genetic influence makes them useful indices of the neurodegenerative process.

Integration of contextual information for hippocampal subfield analysis. Usually surface-based brain imaging approaches [26, 54, 55, 239] rely on segmented image to build surfaces. They solely use surface geometry information for image registration and shape analysis. Some contextual information is considered in the image segmentation stage and boundaries between two different tissues are determined based on some priors learned from the training data. In hippocampal subfield shape analysis work [27, 85, 107, 180, 240], the morphometry comparison usually only uses geometric information.

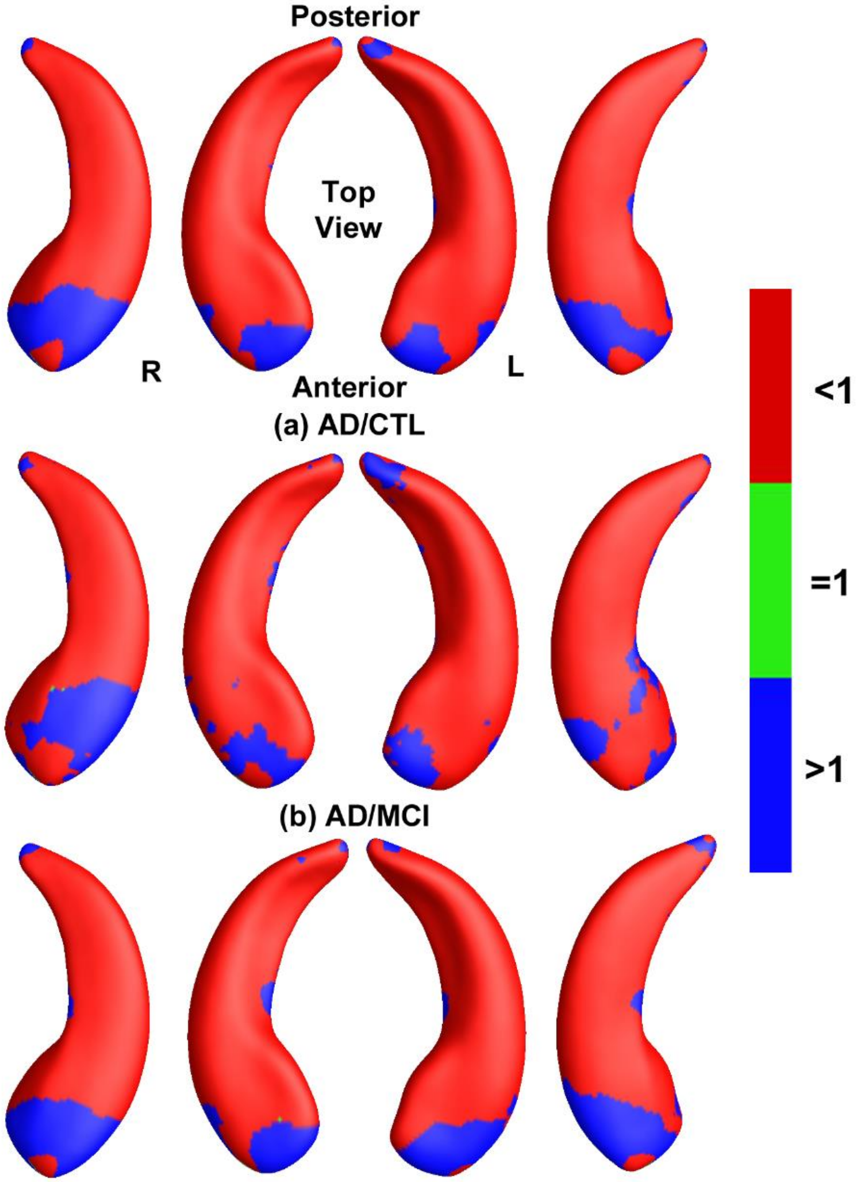

(a) AD/CTL

(b) AD/MCI

(c) MCI/CTL

Figure 2.19. Maps of the ratios of average determinants of the Jacobian matrices R^k, defined in Eq. 2.12. (a) AD over control, (b) AD over MCI, (c) MCI over control. The pictures illustrate the continuous increasing of the atrophy (red color) from control group to MCI and AD. There are also some enlargement areas (blue color). This is probably due to the tissue loss in the neighboring structures of hippocampus, which causes the shifting of the long axis of the hippocampus.

Some methods [105, 119, 241-243] segment hippocampus into different regions and analyze the volume and shape changes of these subfields. These methods compute volumetric image registration between template and individual subject and translate and visualize the deformation on surfaces. The contextual information, e.g. surface registration that considers neighboring image information, may improve the registration accuracy. Nonetheless, the integration has many challenges, such as different resolutions, high dimension, etc. How to combine the contextual information, e.g. considering the neighboring image information in the analysis, to improve statistical power still needs further investigation. Some recent work [244] has proposed new methods which integrate information of curves, surface and volumetric images. It could be a potential future work to improve hippocampal subfield analysis research.

The proposed algorithm is generic and may be useful for other subcortical structure analysis. There are two main caveats when applying the developed surface fluid registration method to study general subcortical surface registration problem. First, in the topology optimization step, the current algorithm requires two landmark cuts, which may restrict the applicability of the proposed method with other subcortical structures. Thus far, we have applied this algorithm to study putamen morphometry in prematurity study [245] and applied another similar algorithm (constrained harmonic map through flattening 3D surfaces [27]) to study morphometry of thalamus [236] and corpus collosum [246] on prematurity and achieved some limited success. Since the subcortical structures are normalized in a common stereotaxic coordinate system in a controlled manner, it is reasonable to assume some geometry extreme positions can serve as geometrically valid and consistent landmarks across subjects in these work. However, it deserves more careful validation on whether these landmarks are also biologically valid and one should be cautious about how consistent they are for a population based study. Second, to map a hippocampal surface to a 2D plane, a few cuts are introduced on the surfaces. Currently, by introducing the same length cuts on consistent surfaces, it is guaranteed that the induced boundaries are consistent across surfaces on the parameter domain and the flow computation is the same for vertices that are close to the boundaries as those in the internal areas. Although the cuts may not alter the geometry of the original surface, it could affect the quality of vertex correspondences near the two curves during the surface fluid registration. Even so, it is a logical conclusion from observing the maps in figure 2.18 that the introduced boundaries do not seem to introduce artifacts and affect the statistical results.

2.5 Conclusion and Future Work

With conformal parameterization, the inverse consistent image fluid registration method was extended to match general surfaces. This has numerous applications in medical imaging. The examples of matching various hippocampal surfaces are relevant for mapping how degenerative diseases affect the brain, as well as building statistical shape models to detect the anatomical effects of disease, aging, or development. The hippocampus is used as specific examples, but the method is general and is applicable in principle to other subcortical surfaces.

The surface-based fluid registration system automates the matching of surfaces by computing a correspondence field guided by the differences of features between the surfaces. This is a natural idea, in that it uses conformal parameterization to transform a surface matching problem into an image registration problem. Whether or not this approach provides a more relevant correspondence than those afforded by other criteria (mutual information, neural nets, or hand landmarking) requires careful validation for each application. Optimal correspondence depends more on utility for a particular application than on anatomical homology. Because different correspondence principles produce different shape models, one future work is to compare them for detecting group differences and genetic influence in brain structures.

As described in Sec. 2.3, the inverse consistent fluid flow that matches one surface to another was computed with the surface feature images and the images were computed by summing up local conformal factor and mean curvature and linearly scaling the dynamic range to [0, 255]. It is possible that some dynamic ranges in the features will be scaled into just one range in the image. Thus an improvement of the accuracy of the fluid registration is to compute the flow directly on the triangular surface coordinates with the original features and finite element method.

As discussed in the Sec. 2.3, results of the proposed method agree with some literature [107, 181]. Similar to other surface-based hippocampal subfield analysis work [85, 107, 180, 240], the proposed method is able to detect some specific significantly different regions. With the current statistical validation strategies, permutation test and false discovery rate, the results match with those from two other methods, SPHARM and FIRST. The spreading results, e.g. between controls and MCI/AD, do not indicate the differences are simply smoothed/averaged over the whole structure. One future work is to further investigate how to apply these detected statistical group differences with drug trials [247], classification [248], and progression [249].

The inverse consistent surface fluid registration framework can also be applied to work with other surface features, such as surface heat kernel signature [34], Beltrami coefficients [112], etc. The proposed multivariate measures may help in detection of degenerative effects, and may also benefit imaging genetics research [250]. In this work, group difference study was used as an application. With multivariate features, it is natural to apply machine learning methods to perform computer-assisted diagnosis and predict future clinical decline [251-253]. One future work is to incorporate the proposed system with some machine learning tools, such as support vector machine [254], sparse learning [255], etc., and build a system which may identify imaging biomarkers that are able to evaluate AD related disease burden and predict progression and response to interventions. The combined system may offer a surface-based subcortical structure morphometry tool to detect the anatomical effects on aging and disease.

CHAPTER 3

SURFACE REGISTRATION WITH HYPERBOLIC RICCI FLOW

Lateral ventricle is an important part in human brain. Its shape morphometry may be associated with many cognitively degenerative diseases, including Alzheimer's disease (AD). However, surface-based ventricular morphometry analysis remains challenging because of its complicated topological structure. This chapter describes a novel ventricular surface registration method based on the hyperbolic Ricci flow algorithm and tensor-based morphometry (TBM). Unlike prior ventricular surface parameterization methods, hyperbolic conformal parameterization is angle-preserving and does not introduce any singularities. The proposed algorithm generates a one-to-one diffeomorphic mapping between ventricular surfaces with consistent boundary matching conditions. The TBM statistics encode a great deal of surface deformation information that could be inaccessible or overlooked by other methods. The proposed method was applied to study ventricular enlargement in mild cognitive impairment (MCI) converters. The dataset consisted of baseline MRI scans of a set of MCI subjects from the Alzheimer's Disease Neuroimaging Initiative (ADNI: 71 MCI converters vs. 62 MCI stable). Although the combined ventricular area and volume features did not differ between the two groups, our fine-grained surface analysis revealed significant differences in the ventricular regions close to the temporal lobe and posterior cingulate, structures that are affected early in AD. Significant correlations were also detected between ventricular morphometry, neuropsychological measures, and a previously described imaging index based on fluorodeoxyglucose positron emission tomography (FDG-PET) scans. This novel ventricular surface registration method may offer a new and more sensitive approach to study preclinical and early symptomatic stage AD.

3.1 Introduction

Lateral ventricle is a fluid-filled structure in human brain, which usually enlarges in neurodegenerative diseases, such as Parkinson's disease [256], schizophrenia [257], AD [27], etc. Owing to the high contrast between the cerebrospinal fluid (CSF) and surrounding brain tissue on T1-weighted images, lateral ventricles can be measured more reliably than hippocampus or other structures, whose boundaries are difficult for experts to agree on [106]. Furthermore, lateral ventricles span a large area within the cerebral hemispheres. Changes in ventricular morphology, such as enlargement, often reflect atrophy of the surrounding cerebral hemisphere which itself may be regionally differentiated (for example, frontotemporal in contrast to posterior cortical atrophy). Regional differences in cerebral atrophy may be reflected in specific patterns of change in ventricular morphology, so accurate analysis of ventricular morphology has the potential to both sensitively and specifically characterize a neurodegenerative process. Particularly, lateral ventricles abut several structures that are relevant to AD, including the hippocampus, amygdala and posterior cingulate. Thus, they may provide an important and sensitive biomarker for AD study.

However, surface-based ventricular shape morphometry study is challenging. It is difficult to apply the surface registration framework as introduced in Chapter 1 to ventricular surfaces, due to their concave shape, complex branching topology and extreme narrowness of the inferior and occipital horns. Thus, surface-based subregional analysis of ventricular enlargement is notoriously difficult to assess, exemplified by the conflicting findings regarding genetic influences on ventricular volumes [258, 259]. Pioneering ventricular morphometry work [96, 168] used spherical harmonics to analyze ventricular surfaces where each ventricular surface was mapped to a sphere and registered to a common template. However, as demonstrated previously [79], this spherical parameterization method may result in significant shape distortion that affects the analysis. Prior work [27, 79, 131] computed the first global conformal parameterization of lateral ventricular surfaces based on holomorphic 1-forms (Sec. 2.2.2). However, this conformal parameterization method always introduces a singularity point (zero point, figure 3.9 (a)) in the resulting parameter domain. As a result, each ventricular surface had to be partitioned into three pieces with respect to the zero point, the superior horn, the inferior horn, and the occipital horn. These three pieces were mapped to three planar rectangles and registered across subjects separately. To model a topologically complicated ventricular surface, hyperbolic conformal geometry emerges naturally as a candidate method. Hyperbolic conformal geometry has an important property that it can induce conformal parameterizations on high-genus surfaces or surfaces with negative Euler numbers and the resulting parameterizations have no singularities [260]. Motivated by recent advances in hyperbolic conformal geometry based brain imaging research [5, 44, 45, 81, 261], here I propose to use the hyperbolic Ricci flow method to build the canonical parameter domain for ventricular surface registration. The resulting parameterizations are angle-preserving and have no singularity points. After surface registration across subjects, surface deformations are measured by the tensor-based morphometry (TBM) [29, 30, 32, 118], which quantifies local surface area expansions or shrinkages. The Ricci flow method is theoretically sound and computationally efficient [2, 262, 263]. In addition, TBM has been used extensively to detect regional differences in surface and volume brain morphology between groups of subjects [2, 27, 80, 118, 125, 264-267]. The hypothesis is that the hyperbolic Ricci flow together with TBM may offer a set of accurate surface statistics for ventricular morphometry study.

This chapter presents a ventricular surface registration system based on hyperbolic Ricci flow and TBM statistic. It was applied to study ventricular structural differences associated with baseline T1-weighted brain images from the ADNI dataset, including 71 MCI patients who developed incident AD during the subsequent 36 months (MCI converter group) and 62 MCI patients who did not convert during the same period (MCI stable group). These subjects were also selected based on the availability of fluorodeoxyglucose positron emission tomography (FDG-PET) data and cognitive assessment information. MCI is a transitional stage between normal aging and dementia and people with MCI are at high risk of progression to dementia. MCI is attracting increasing attention, as it offers an opportunity to target the disease process during an early symptomatic stage. As the paradigm in AD research shifts to a new stage, targeting earlier intervention and prevention [268, 269], there is a requirement for biologically grounded, highly objective biomarkers that can help to identify those high AD risk MCI individuals for whom early intervention may be most appropriate. Various neuroimaging techniques can track disease progression and therapeutic efficacy in MCI [87, 270-276] and others are beginning to identify abnormal anatomical or functional patterns and their rates of decline. Here I set out to test whether the new system can detect subtle MCI conversion related ventricular changes and whether the changes are correlated with FDG-PET biomarkers and other cognitive measures.

3.2 Ventricular Surface Registration with Hyperbolic Ricci Flow

3.2.1 Algorithm Overview

This section briefly overviews the processing procedures in the proposed method. Following sections are detailed explanations of each step.

Figure 3.1 summarizes the overall sequence of steps in the algorithm. First, from each MRI scan (a), the lateral ventricular volumes are automatically segmented with the multi-atlas fluid image alignment (MAFIA) method [106]. The MR image overlaid with the segmented ventricle is shown in (b). A ventricular surface built with marching cube algorithm [127] is shown in (c). Lateral ventricle segmentation and surface reconstruction will be introduced in Sec. 3.2.2. After the topology optimization, we apply hyperbolic Ricci flow method on the ventricular surface and conformally map it to the Poincaré disk. The concepts of topology optimization and Poincaré disk model will be introduced in Sec. 3.2.3. Details about conformal parameterization with hyperbolic Ricci flow and embedding in Poincaré disk are in Sec. 3.2.4 and 3.2.5, respectively. On the Poincaré disk, consistent geodesics are computed and projected back to the original ventricular surface, a method called geodesic curve lifting. The results are shown in (d). Further, the Poincaré model is converted to the Klein model, where the ventricular surfaces are registered by the constrained harmonic map [1]. The registration diagram is shown in (e). Geodesic curve lifting and surface registration will be detailed in Sec. 3.2.6. Next, we compute the TBM features and smooth them with the heat kernel method [277] (f). TBM computation and its smoothing are in Sec. 3.2.7. Finally, the smoothed TBM features are applied to analyze both group difference between the two MCI groups and correlation of ventricular shape morphometry with cognitive test scores and FDG-PET index. Significance *p*-maps are used to visualize local shape differences or correlations (g). Correction for multiple comparisons is used to estimate the overall significance (corrected *p*-values).

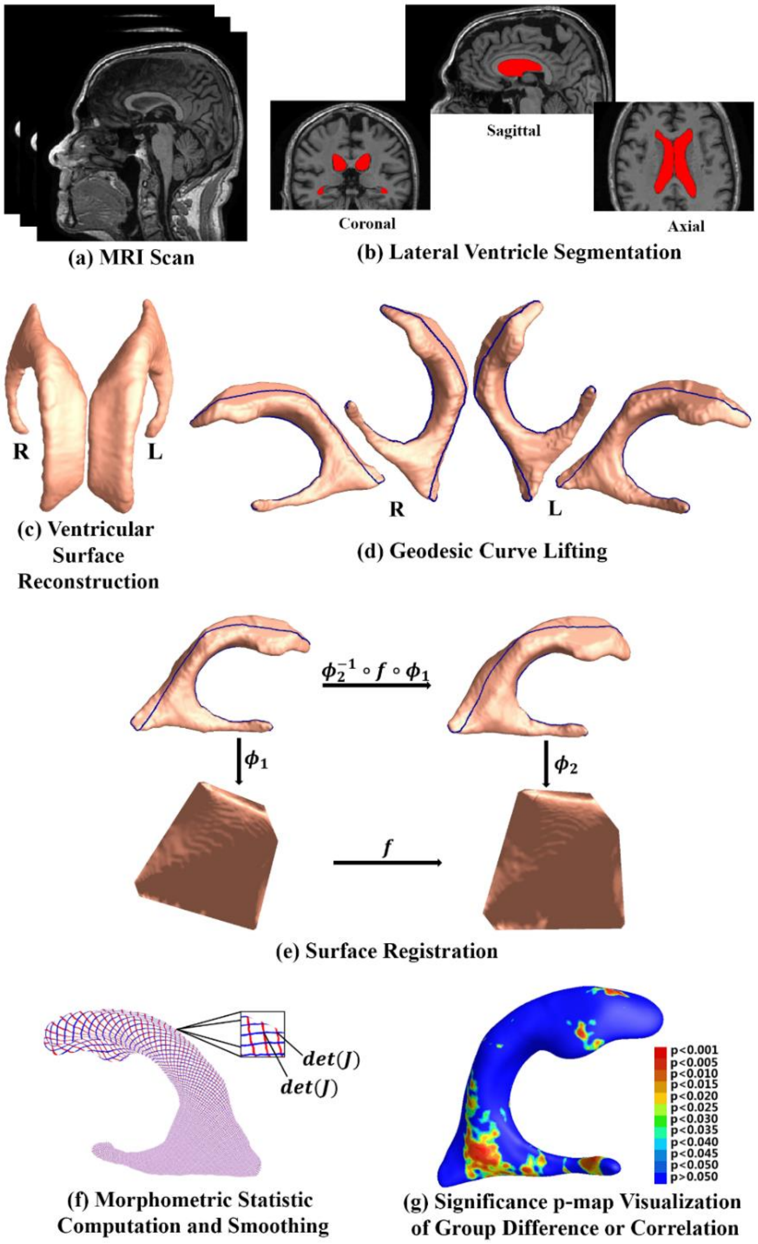

Figure 3.1. A chart showing the key steps in the ventricular surface registration method.

3.2.2 Image Segmentation and Preprocessing

The T1-weighted images from ADNI baseline dataset were automatically skull-stripped with the BrainSuite Extraction Software [210]. Then the imperfections in this automatic segmentation procedure were corrected manually. In order to adjust for global differences in brain positioning and scaling, the segmented images were normalized to the ICBM space with a 9-parameter (3 translations, 3 rotations, and 3 scales) linear transformation obtained by the Minctracc algorithm [278]. After resampling into an isotropic space of 220^3 voxels with the resolution $1\text{mm} \times 1\text{mm} \times 1\text{mm}$, the registered images were then histogram-matched to equalize image intensities across subjects. Finally, the lateral ventricular volumes were extracted using the multi-atlas fluid image alignment (MAFIA) method that combines multiple fluid registrations to boost accuracy [106]. Briefly, in the MAFIA method, 6 MRI scans (2 AD, 2 MCI, and 2 normal) after preprocessing were randomly chosen from the ADNI baseline dataset. The lateral ventricles were manually traced in these 6 images following the delineation protocol described in http://resource.loni.usc.edu/resources/downloads/research-protocols/segmentation/lateral-ventricle-delineation. These labeled images are called atlases and segmentation of lateral ventricles in other unlabeled images was done by fluidly registering the atlases to all other images. For details of this method, please refer to [106].

As introduced in Sec. 2.2.1, after obtaining the binary segmentations of the lateral ventricles, a topology-preserving level set method [126] was used to build surface models. Based on that, the marching cubes algorithm [127] was applied to construct triangular surface meshes. Then, in order to reduce the noise from MR image scanning and to overcome the partial volume effects, the two-step surface smoothing process introduced in

Sec. 2.2.1 was also applied consistently to all ventricular surfaces. As proved in Sec. 2.4, the smoothed meshes are accurate approximations to the original surfaces with higher signal-to-noise ratio (SNR).

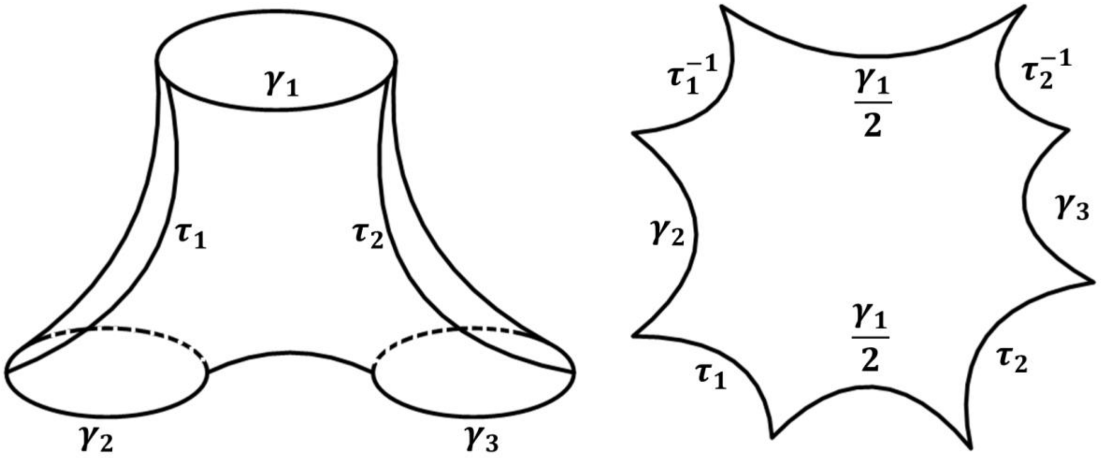

(a) A Pair of Topological Pants **(b) Topological Disk of Fundamental Domain**

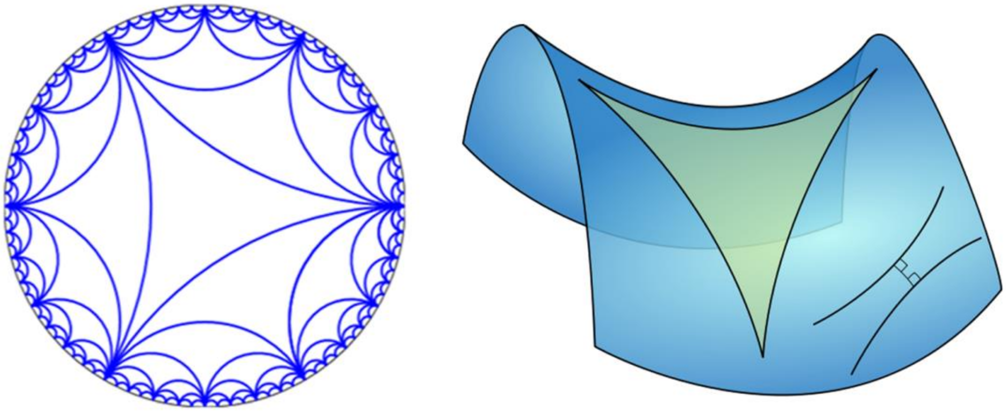

(c) Poincaré Disk **(d) Saddle Plane**

Figure 3.2. Illustration of hyperbolic geometry. (a) is a pair of topological pants with three boundaries $\gamma_1, \gamma_2, \gamma_3$. τ_1, τ_2 are automatically traced paths connecting γ_1 to γ_2, γ_1 to γ_3, respectively. After slicing along τ_1, τ_2, the topological pants can be conformally mapped to the hyperbolic space and isometrically embedded in the topological disk of fundamental domain, as shown in (b). (c) is an illustration of the Poincaré disk model. (d) is a saddle plane which has constant negative Gaussian curvatures with a hyperbolic triangle.

3.2.3 Theoretical Background

This section briefly introduces the theoretical background necessary for this work.

Conformal deformation. Let S be a surface in $\mathbb{R}^3$ with a Riemannian metric $\mathbf{g}$ induced from the Euclidean metric. Let $u: S \rightarrow \mathbb{R}$ be a scalar function defined on S. It can be verified that $\tilde{\mathbf{g}} = e^{2u}\mathbf{g}$ is also a Riemannian metric on S and angles measured by $\tilde{\mathbf{g}}$ are equal to those measured by $\mathbf{g}$, i.e. the induced mapping is angle-preserving. Thus, $\tilde{\mathbf{g}}$ is called a conformal deformation of $\mathbf{g}$ and u is called the conformal factor. Furthermore, when surface metrics change, the Gaussian curvature K of the surface will change accordingly and become $\widetilde{K} = e^{-2u}(-\Delta_{\mathbf{g}}u + K)$, where $\Delta_{\mathbf{g}}$ is the Laplace-Beltrami operator under the original metric $\mathbf{g}$. The geodesic curvature k_g will become $\widetilde{k_g} = e^{-u}(\partial_{\boldsymbol{r}}u + k_g)$, where $\boldsymbol{r}$ is the tangent vector orthogonal to the boundary. The total curvature of the surface is determined by its topology with the Gauss-Bonnet theorem [71]: $\int_S K\,dA + \int_{\partial S} k_g ds = 2\pi\chi(S)$, where dA is the surface area element, ∂S is the boundary of S, ds is the line element, and $\chi(S)$ is the Euler characteristic number of S.

Uniformization theorem. Given a surface S with Riemannian metric $\mathbf{g}$, there exist an infinite number of metrics that are conformal to $\mathbf{g}$. The uniformization theorem states that, among all conformal metrics, there exists a unique representative which induces constant Gaussian curvature everywhere. Moreover, the constant will be one of $\{+1, 0, -1\}$. Therefore, the universal covering space of any closed surface can be embedded onto one of the three canonical spaces using its uniformization metric: the unit sphere $\mathbb{S}^2$ for genus-0 surfaces with positive Euler characteristic numbers; the plane $\mathbb{E}^2$ for genus-1 surfaces with zero Euler characteristic numbers; the hyperbolic space $\mathbb{H}^2$ for high-genus surfaces with negative Euler characteristic numbers. Accordingly, we can say that surfaces with positive Euler numbers admit spherical geometry; surfaces with zero Euler numbers admit Euclidean geometry; and surfaces with negative Euler numbers admit hyperbolic geometry.

Topology optimization. Due to the concave and branching shape of the ventricular surfaces, it is difficult to find a conformal grid for the entire structure without introducing significant area distortions. Here, as in prior studies [27, 79], three cuts were automatically located and introduced on each ventricular surface, with one cut on the superior horn, one cut on the inferior horn, and one cut on the occipital horn. The locations of the cuts are motivated by examining the topology of the lateral ventricles, in which several horns are joined together at the ventricular "atrium" or "trigone". Meanwhile, the locations of the cuts were guaranteed to be consistent across subjects. This operation is called topology optimization [27, 79] of ventricular surfaces. After being modeled in this way, each ventricular surface becomes a genus-0 surface with 3 boundaries and is homotopic to a pair of topological pants, as shown in figure 3.2 (a). Figure 3.4 (a) shows two different views of a ventricular surface with the three boundaries, which are denoted as $\gamma_1, \gamma_2, \gamma_3$. As a result, each ventricular surface has the Euler characteristic number -1, which means that it admits the hyperbolic geometry. This work tries to compute conformal mappings from ventricular surfaces to the hyperbolic space $\mathbb{H}^2$ and uses it as the canonical parameter space to register ventricular surfaces.

Poincaré disk model. As the hyperbolic space cannot be realized in $\mathbb{R}^3$, the Poincaré disk model is used to visualize it. The Poincaré disk is the unit disk $|z| < 1, z = x + iy$ in the complex plane with the metric $ds^2 = \frac{4dzd\bar{z}}{(1-z\bar{z})^2}$. The rigid motion in the Poincaré disk is the Möbius transformation:

$$z \to e^{i\theta}\frac{z-z_0}{1-\overline{z_0}z} \tag{3.1}$$

In Euclidean space, rigid motions include translation and rotation. Any transformation consisting of rigid motions changes the position of an object without deforming the shape of the object. As the Poincaré disk is a representation of the hyperbolic space, the rigid motion in it is defined by Eq. 3.1, which is the *Möbius* transformation and is different from that in the Euclidean space. However, the *Möbius transformation has the same properties as the Euclidean rigid motion. For example, as shown in figure 3.4 (d), the object at the center is transformed to four other different positions in the* Poincaré disk with four different *Möbius transformations. Each of the four pieces (shown in four colors) is a copy of the center object. They have different positions, but their shapes are the same in the hyperbolic space.* A hyperbolic line (a geodesic) in the Poincaré disk is a circular arc which is perpendicular to the unit circle $|z| = 1$. A hyperbolic circle $circ(c, r)$ (c is the center and r is the radius) looks like a Euclidean circle $Circ(C, R)$, with $C = \frac{2-2\mu^2}{1-\mu^2|c|^2}$, and $R^2 = |C|^2 - \frac{|c|^2-\mu^2}{1-\mu^2|c|^2}$, where $\mu = \frac{e^r-1}{e^r+1}$. Figure 3.2 (c) shows an illustration of the Poincaré disk. In order to map the ventricular surfaces to the hyperbolic Poincaré disk, two paths, τ_1 connecting γ_1 and γ_2 and τ_2 connecting γ_1 and γ_3, were automatically traced, as shown in figure 3.4 (b). Initially, the locations of the paths were not required to be consistent across subjects. But they were required to connect consistent ends of $\gamma_1, \gamma_2, \gamma_3$ for consistent surface mappings to be discussed in Sec. 3.2.6. As shown in figure 3.4 (a-b), endpoints with same colors were connected to each other. After slicing along the paths, a ventricular surface became a simply connected domain, which we call a topological disk. Figure 3.2

(b) is an illustration of the topological disk of the topological pants in figure 3.2 (a), which provides the fundamental domain when embedded in the Poincaré disk.

In practice, surfaces are represented by triangular meshes. If a surface admits hyperbolic geometry, all triangles on it are hyperbolic triangles. As an illustration of the hyperbolic geometry, figure 3.2 (d) shows a saddle-shape plane which has constant negative Gaussian curvatures with a hyperbolic triangle.

3.2.4 Hyperbolic Ricci Flow

This work uses the surface Ricci flow method [1, 2, 45, 262, 263] to conformally project the ventricular surfaces to the hyperbolic space and isometrically embeds them in the Poincaré disk. This method is called the hyperbolic Ricci flow.

Ricci flow is a powerful curvature flow method, which was first introduced in [279]. Let S be a smooth surface with Riemannian metric $\mathbf{g} = (g_{ij})$, the Ricci flow deforms the metric $\mathbf{g}(t)$ according to the Gaussian curvature $K(t)$ (induced by the metric itself),

$$\frac{dg_{ij}(t)}{dt} = -2K(t)g_{ij}(t) \tag{3.2}$$

where t is the time parameter. Eq. 3.2 states that the metric should change according to the Gaussian curvature, so that the curvature evolves like a heat diffusion process. There is an analogy between the Ricci flow and heat diffusion. Suppose $T(t)$ is a temperature field on the surface, the heat diffusion equation is $\frac{dT(t)}{dt} = -\Delta_{\mathbf{g}}T(t)$, where $\Delta_{\mathbf{g}}$ is the Laplace-Beltrami operator induced by the surface metric. The temperature field becomes more and more uniform with the increase in t, and it will become constant eventually. In a physical sense, the curvature evolution induced by the Ricci flow is exactly the same as the heat diffusion on the surface as $\frac{dK(t)}{dt} = -\Delta_{\mathbf{g}(t)}K(t)$, where $\Delta_{\mathbf{g}(t)}$ is the Laplace-Beltrami operator induced by the metric $\mathbf{g}(t)$. For the proof of this analogy, please refer to [2].

With conformal mapping, which requires $\mathbf{g}(t) = e^{2u(t)}\mathbf{g}(0)$, we have a simplified Ricci flow equation

$$\frac{du(t)}{dt} = -2K(t) \tag{3.3}$$

the derivation of Eq. 3.3 can be found in [2].

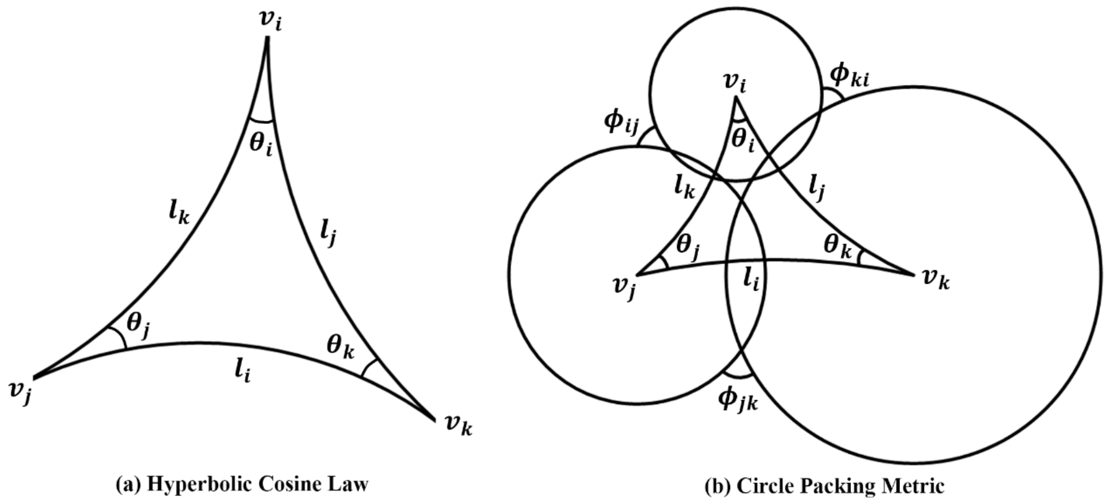

Figure 3.3. Illustration of the hyperbolic cosine law (a) and visualization of the circle packing metric on a hyperbolic triangle (b).

In engineering field, surfaces are approximated by triangular meshes. Major concepts such as metric, curvature, Ricci flow, etc., which were introduced above in the continuous setting, need to be generalized to the discrete setting. Suppose $M(V, E, F)$ is a triangular mesh, with the vertex set V, edge set E, and face set F. We define v_i the ith vertex, $[v_i, v_j]$ the edge connecting vertices v_i and v_j, and $[v_i, v_j, v_k]$ the face formed by v_i, v_j, v_k. The discrete Riemannian metric on M is a function defined on each edge $l: E \rightarrow R^+$ such that in each face $[v_i, v_j, v_k]$, the triangle inequality holds $l_i + l_j > l_k$. Usually, it is the edge length. As shown in figure 3.3 (a), the corner angles in each face are determined by the metric according to the hyperbolic cosine law:

$$\theta_i = \cos^{-1} \frac{\cosh l_j \cosh l_k - \cosh l_i}{2 \sinh l_j \sinh l_k} \tag{3.4}$$

Let f_{ijk} be the face formed by v_i, v_j, v_k, and θ_i^{jk} the corner angle at v_i in this face, the discrete Gaussian curvature on v_i can be defined by the angle deficit:

$$K_i = \begin{cases} 2\pi - \sum_{f_{ijk} \in F} \theta_i^{jk} & v_i \notin \partial M \\ \pi - \sum_{f_{ijk} \in F} \theta_i^{jk} & v_i \in \partial M \end{cases} \tag{3.5}$$

The discrete Gaussian curvature definition is an approximation of that in the continuous setting, for the derivation, please refer to [40]. Accordingly, the Gauss-Bonnet theorem also holds for the discrete meshes $\sum_{v_i \in V} K_i = 2\pi\chi(M)$ [71].

By definition, the conformal deformation maps infinitesimal circles in one surface to infinitesimal circles in another and preserves angles among the circles. The discrete conformal deformation uses circles with finite radii to approximate the infinitesimal circles. The concept of the circle packing metric was introduced in [280] and later adopted by Hurdal and Stephenson in their discrete cortical conformal flattening work [78, 281]. Figure 3.3 (b) shows a hyperbolic triangle together with three circles centered at its three vertices. Let Γ be a function defined on vertices $\Gamma: V \to \mathbb{R}^+$, which assigns a radius γ_i to vertex v_i. Similarly, let Φ be a function defined on edges $\Phi: E \to [0, \frac{\pi}{2}]$, which assigns an acute angle ϕ_{ij} to edge e_{ij} and is called a weight function of the edge. The pair of vertex radius function and edge weight function, (Γ, Φ), is called the circle packing metric of M. As shown in [1, 2, 282], the circles in the circle packing metric are not necessarily tangent to each other, they can intersect [2], or not intersect at all [1]. As shown in figure 3.3 (b), for each triangle $[v_i, v_j, v_k]$, one can compute the Riemannian metrics by the hyperbolic cosine law:

$$l_k = \cosh^{-1}(\cosh\gamma_i \cosh\gamma_j + \cos\phi_{ij} \sinh\gamma_i \sinh\gamma_j) \tag{3.6}$$

Let $U: V \to \mathbb{R}$ be the discrete conformal factor and [1, 263],

$$u_i = \log(\tanh \frac{\gamma_i}{2}) \tag{3.7}$$

the discrete Ricci flow is defined as

$$\frac{du_i}{dt} = -2K_i \tag{3.8}$$

The discrete Ricci flow is in the exact same form as the smooth Ricci flow (Eq. 3.3). Let $U = (u_1, u_2, \dots, u_n)$ be the conformal factor vector, where n is the number of vertices on M, and $U_0 = (0,0, \dots, 0)$, then the discrete hyperbolic Ricci energy is defined as [263]

$$E(U) = \int_{U_0}^{U} \sum_{i=1}^{n} K_i du_i \tag{3.9}$$

Given the definitions 3.4, 3.6 and 3.7, by direct computations, we get $\frac{\partial\theta_i}{\partial u_j} = \frac{\partial\theta_j}{\partial u_i}$. Considering the definition of K_i (Eq. 3.5), immediately we get $\frac{\partial K_i}{\partial u_j} = \frac{\partial K_j}{\partial u_i}$. Thus, the differential 1-form $\omega = \sum_{i=1}^{n} K_i du_i$ is closed as $d\omega = 0$. This proves that the hyperbolic Ricci energy (Eq. 3.9) is convex and its unique global minimum corresponds to the hyperbolic metric with zero vertex Gaussian curvatures. The discrete Ricci flow is the negative gradient flow of the hyperbolic Ricci energy.

The algorithm with gradient descent is summarized as following:

i. Compute the initial radius γ_i for each vertex v_i, and weight ϕ_{ij} for each edge e_{ij} with the hyperbolic cosine law;

ii. Set the target Gaussian curvature as zero;

iii. Compute edge lengths with Eq. 3.6, face corner angles with Eq. 3.4, and the Gaussian curvature with Eq. 3.5.

iv. Update u_i for each vertex v_i with Eq. 3.8 as $u_i^{t+1} = u_i^t - 2\Delta t K_i$.

v. Update γ_i with Eq. 3.7.

vi. Repeat steps (3) to (5) until the final Gaussian curvature is no greater than a user-specified error tolerance.

Instead of gradient descent, the Ricci energy (Eq. 3.9) can also be optimized by Newton's method [2, 263], which requires compute the Hessian matrix. Let $H = (h_{ij})$ be the Hessian matrix, then

$$h_{ij} = \frac{\partial K_i}{\partial u_j}, h_{ii} = \frac{\partial K_i}{\partial u_i}$$

In the experiments, the Newton's method was used to optimize the Ricci energy, which is stable and fast (details are in Sec. 4.4.2). For a ventricular surface with more than 50K vertices, the optimization took less than 30 seconds on a 2.66 GHz Intel Quad CPU Q8400 PC with Windows 7 64-bit operating system.

3.2.5 Embedding into the Poincaré Disk Model

After computing the discrete hyperbolic metric of a surface, it can be embedded onto the Poincaré disk. At the beginning, a seed face f_{012} is selected and the positions of its vertices v_0, v_1, v_2 are computed in the Poincaré disk as following:

$$p(v_0) = (0,0), p(v_1) = \frac{e^{l_{01}} - 1}{e^{l_{01}} + 1}(1,0), p(v_2) = \frac{e^{l_{02}} - 1}{e^{l_{02}} + 1}(\cos\theta_0^{12}, \sin\theta_0^{12})$$

Then the embedding is propagated to other faces. We put all un-embedded faces adjacent to the current face into a queue. A face f_{ijk} is popped from the queue and checked whether all its vertices have been embedded. If so, continue to pop the next face from the queue. Otherwise, suppose that v_i and v_j are embedded, then $p(v_k)$ can be computed as one of the two intersections between two hyperbolic circles, $circ(p(v_i), l_{ki})$ and $circ(p(v_j), l_{kj})$, satisfying $\left(p(v_j) - p(v_i)\right) \times \left(p(v_k) - p(v_i)\right) > 0$. Continue to do so until the queue is empty. Figure 3.4 (c) shows the embedding of the ventricular surface in the Poincaré disk. The boundaries $\gamma_1, \gamma_2, \gamma_3$ have become geodesics $\frac{\gamma_1}{2}, \frac{\gamma_1}{2}, \gamma_2, \gamma_3$. It is called the Poincaré disk embedding of the fundamental domain of the surface. As pointed out in [263], different selections of the seed face will result in different layouts of the fundamental domain. In this work, to keep the fundamental domain consistency across subjects, prior holomorphic 1-form based method [27, 283] was firstly applied to compute a Euclidean conformal mapping and the seed face was then automatically chosen as the center of the zero point region [131], as shown in figure 3.9 (a).

The computed boundaries of the fundamental domains of different ventricular surfaces are not consistent, i.e., the positions of τ_1, τ_2 may not be consistent. A geodesic lifting step is further applied to achieve consistent boundaries with the deck transformation group generators. For a surface with hyperbolic geometry, its universal covering space is the entire Poincaré disk. As shown in figure 3.4 (c), there are 4 free sides in the fundamental domain, τ_1, τ_2 and their compliments τ_1^{-1}, τ_2^{-1} (after cutting along a curve, it generates two boundaries on the new surface, one is τ_1 and its compliment is τ_1^{-1}). The rigid transformations across these sides induce different periods of the surface mapping. In Poincaré disk, all rigid motions are Möbius transformations. There exist unique Möbius transformations map τ_1 to τ_1^{-1} and τ_2 to τ_2^{-1}, respectively, as shown in figure 3.4 (d). The details for computing the Möbius transformation that maps τ_1 to τ_1^{-1} are explained here. Counterclockwisely, let the starting and ending vertices of the two sides be $\partial\tau_1 = (p_0, q_0)$ and $\partial\tau_1^{-1} = (q_1, p_1)$. The geodesic distance from p_0 to q_0 equals the geodesic distance from p_1 to q_1 in the Poincaré disk. To align them, a Möbius transformation t_0, which maps p_0 to the origin and q_0 to a positive real number, is computed with

$$t_0 = e^{i\theta_0}\frac{z - p_0}{1 - \overline{p_0}z}, \theta_0 = arg\frac{p_0 - q_0}{1 - \overline{p_0}q_0}$$

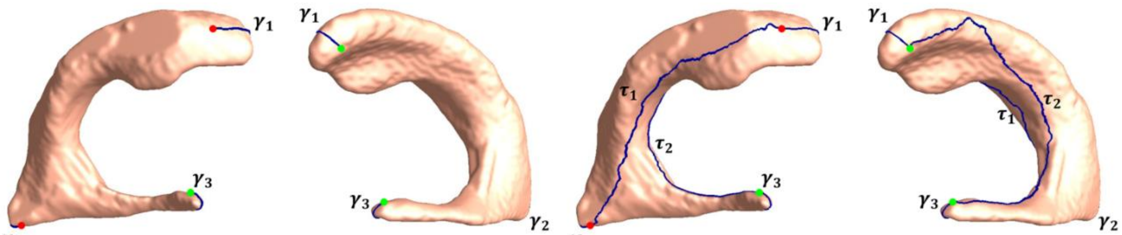

(a) Topology Optimization of a Left Ventricular Surface Shown in Two Different Views

(b) Paths Connecting Boundary Endpoints on the Ventricular Surface in (a) Shown in Two Different Views

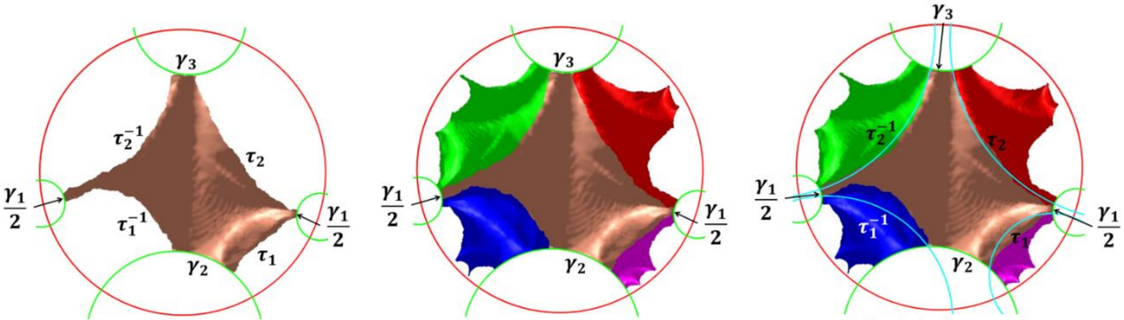

(c) Poincaré disk Embedding

(d) Universal Covering Space

(e) Geodesic Computation

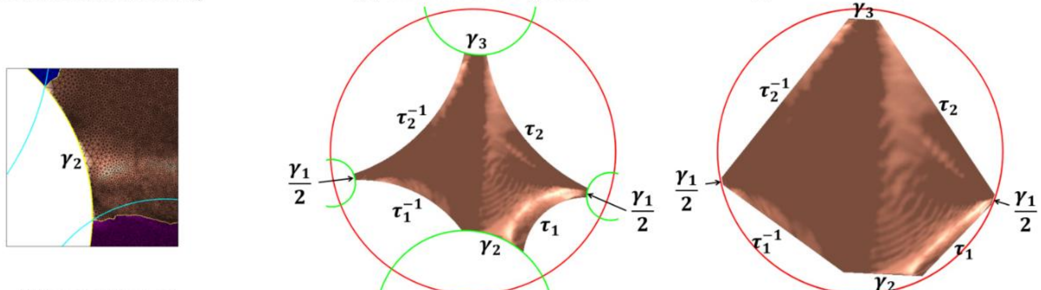

(f) Zoomed View of Geodesic Computation

(g) Canonical Fundamental Domain

(h) Klein Model

Figure 3.4. A chart showing the computation of geodesic curves for a ventricular surface.

Similarly, another Möbius transformations t_1, which maps p_1 to the origin and q_1 to a positive real number, can be computed. Then with $t_0(q_0) = t_1(q_1)$, the final Möbius transformation is $t = t_1^{-1} \circ t_0$, which satisfies $p_1 = t(p_0)$ and $q_1 = t(q_0)$. Any deck transformation can be composed by the generators. Then the universal covering space can be tiled by transforming a fundamental domain by the deck transformations and gluing the transformed fundamental domains with the original fundamental domain. Figure 3.4 (d) shows a portion of the universal covering space, which is tiled by 5 fundamental domains, one original and 4 transformed by the 4 deck transformation group generators.

3.2.6 Geodesic Curve Lifting and Ventricular Surface Constrained Harmonic Map via the Klein Model

As stated in Chapter 1, to register brain surfaces, a common approach is to compute a range of intermediate mappings to a canonical parameter space, such as a sphere [25, 56, 57, 284] or a planar domain [28, 58, 79, 80, 285, 286]. In the current work, the Klein model is used as the canonical space to register ventricular surfaces.

First, the Poincaré disk model is used to achieve consistent geodesic curves across ventricular surfaces. As shown in figure 3.4 (c), $\frac{\gamma_1}{2}, \frac{\gamma_1}{2}, \gamma_2, \gamma_3$ are already geodesics on the Poincaré disk model, but the paths between them, $\tau_1, \tau_2, \tau_1^{-1}, \tau_2^{-1}$, are not. Figure 3.4 (b) shows the paths on the original surface. If the positions of the paths are not consistent across subjects, the fundamental domains will also be different for different surfaces. This problem can be solved by locating the geodesic on the Poincaré disk between two fixed points and mapping it back to the original surface, a step known as geodesic curve lifting. Specifically, each of these geodesics is an arc on a circle which passes two fixed points in the Poincaré disk and is orthogonal to the unit circle. Thus the geodesics are unique. The fixed points are the endpoints of existing geodesics. For example, as shown in figure 3.4 (e), τ_1 is an arc on the circle which passes one endpoint of $\frac{\gamma_1}{2}$ and one endpoint of γ_2 and is orthogonal to $|z| = 1$. As stated in Sec. 3.2.3, the initial paths τ_1, τ_2 can be inconsistent, but they have to connect consistent endpoints of $\gamma_1, \gamma_2, \gamma_3$, as to guarantee the consistency of the geodesic curve computation. After slicing the universal covering space along the geodesics, we get the canonical fundamental domain, as shown in figure 3.4 (g). All the boundary curves become geodesics. As the geodesics are unique, they are also consistent when mapped back to the surface in $\mathbb{R}^3$. As shown in figure 3.5, the first row shows a left ventricular surface from the MCI stable group and second row shows one from the MCI converter group. It can be seen that, although the two surfaces have different shapes due to disease progression, the geodesics τ_1, τ_2 on them are consistent.

Furthermore, the Poincaré model is converted to the Klein model with the following transformation [1],

$$z \rightarrow \frac{2z}{1+\bar{z}z} \tag{3.10}$$

It converts the canonical fundamental domains of the ventricular surfaces to a Euclidean octagon, as shown in figure 3.4 (h). Then the Klein disk is used as the canonical parameter space for the ventricular surface registration.

In the experiment, 133 left and 133 right ventricular surfaces were registered to a common left and right template, respectively. The templates are the left and right ventricular surfaces from a randomly selected subject. The octagon constrained harmonic map [2, 27] was implemented. Briefly, the constrained harmonic map was computed by solving the Laplace equation with the Dirichlet boundary condition. Suppose M, N are two ventricular surfaces with their Klein disks, the map $f: M \rightarrow N$ is a harmonic map if $\Delta f = 0$. In order to solve the Laplace equation, all the boundary curves in the Klein octagon disk were treated as boundary conditions and enforced to be aligned across subjects with linear interpolation by the arc length parameter. To show the correspondences between boundaries, unique labels were assigned to geodesic boundaries shown in figure 3.5.

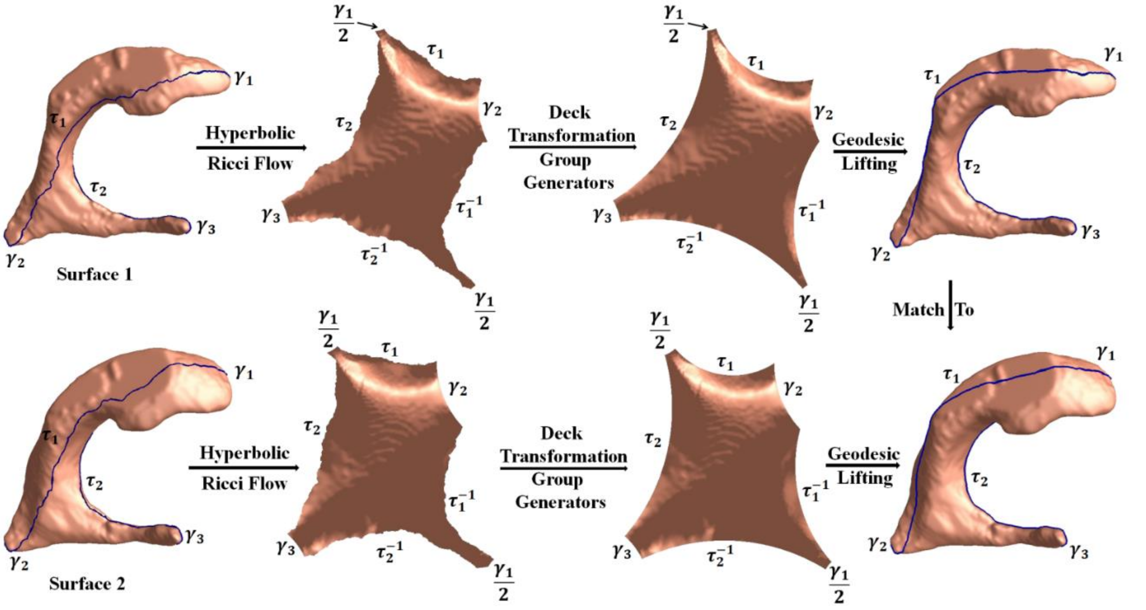

Figure 3.5. Illustration of ventricular surface registration with the hyperbolic Ricci flow and geodesic curve lifting. Surface 1 and surface 2 were from the MCI stable group and MCI converter group, respectively. After computing their canonical fundamental domains with the steps in figure 3.4, the computed geodesic curves were lifted to the original surfaces. The last column shows that the geodesic curves introduced by the proposed method are consistent across subjects. Then the surfaces were registered by constrained harmonic map with consistent geodesic curve matching.

3.2.7 Surface Tensor-based Morphometry and Its Smoothness with Heat Kernel Method

This work uses surface tensor-based morphometry (TBM) [29, 30, 32] to analyze the ventricular shape changes along with disease progression. Specifically, details for computing the Jacobian matrix of the map between two ventricular surfaces were given in Sec. 2.2.5. After computing the Jacobian matrix J with Eq. 2.10, the TBM is defined as $\sqrt{\det(J)}$. TBM measures the amount of local area changes in a surface with the map ϕ [32].

As pointed out in [277, 287], in an integrated surface analysis system, each step in the processing pipeline including MR image acquisition, image segmentation, surface reconstruction, etc., are expected to introduce noise in the deformation measurement. To account for the noise effects, the heat kernel smoothing algorithm proposed in [277] is applied to increase the SNR in the TBM statistical features and boost the sensitivity of statistical analysis. The smoothing method is briefly described as follows, for details please refer to [277].

Let S be a surface and $p \in S$ be a point on S. Y is a real-valued function defined on S, representing a measurement of the surface, e.g., the TBM features in this work. Consider a stochastic model for Y as $Y(p) = \theta(p) + \epsilon(p)$, where θ is the unknown mean measurement and ϵ is a zero mean Gaussian random field. The heat kernel smoothing estimator of θ is defined by the convolution

$$\bar{\theta}(p) = K_\sigma * Y(p) = \int_S K_\sigma(p,q)Y(q)d\mu(q) \tag{3.11}$$

where q is a point on S which is adjacent to p, $\mu(q)$ is the surface Lebesgue measure, and σ is the smoothing parameter (bandwidth). In numerical implementation, if σ is sufficiently small and q is sufficiently close to p, the heat kernel is defined as:

$$K_\sigma(p,q) \approx \frac{1}{\sqrt{2\pi\sigma}} \exp[-\frac{d^2(p,q)}{2\sigma^2}] \tag{3.12}$$

where $d(p,q)$ is the geodesic distance between p and q. Heat kernel smoothing with large bandwidth can be decomposed into iterated kernel smoothing with small bandwidth via

$$K_\sigma^{(m)} * Y = \underbrace{K_\sigma * K_\sigma * \ldots * K_\sigma * Y}_{m\ times} = K_{\sqrt{m}\sigma} * Y \tag{3.13}$$

For the case at hand, we define $N_p = \{q_0, q_1, \ldots, q_k\}$ to be the set of neighboring points of p on S and the normalized truncated kernel for S to be

$$W_\sigma(p,q_i) = \frac{\exp[-\frac{d^2(p,q_i)}{2\sigma^2}]}{\sum_{j=0}^{k} \exp[-\frac{d^2(p,q_j)}{2\sigma^2}]} \tag{3.14}$$

The discrete convolution is defined as $W_\sigma * Y(p) = \sum_{i=0}^{k} W_\sigma(p,q_i) Y(q_i)$.

3.2.8 Ventricular Surface Morphometry Analysis of MCI Group Differences Study

To evaluate whether ventricular morphometry, analyzed in this way, could be a valid predictive biomarker, morphological differences in the lateral ventricles extracted from the baseline MR images between the two different MCI groups were studied. The Student's *t* test is applied on the TBM statistic to study group difference; same to Sec. 2.3.6, permutation tests are used to correct for multiple comparisons [288]. Given two groups of ventricular surfaces, on each surface point, a *t* value with true group labels is computed to represent the difference between the two groups of subjects on this point. Then the ventricular surfaces are randomly assigned into two groups with same number of subjects in each group as in the true grouping and the *t* value on each surface point is re-computed, which is denoted as the *t'* value. The random group assignment is permuted 5,000 times and results in 5,000 *t'* values on each point. A probability on each surface point is computed as the ratio of the number of *t'* values which are greater than the *t* value to the number of total permutations. These probability values (*p*-values) are color coded on an average ventricular shape to build the significance *p*-map (uncorrected) of the group comparison. Given a predefined statistical threshold of $p = 0.05$, the feature in a significance *p*-map is defined as number of surface points with *p*-values lower than this threshold, which is also regarded as the real effect in the true experiment. The feature is then compared with features that occur by accident in the random groupings. A ratio is computed describing the fraction of the time an effect of similar or greater magnitude to the real effect occurs in the random assignments. This ratio is the chance of the observed pattern occurring by accident and provides an overall significance value of the map (corrected for multiple comparisons) [289].

3.2.9 Correlation Between Ventricular Shape and Cognition and Other AD Biomarkers

In addition to examining the group difference, we also investigated the ventricular shape morphometry correlation with each of several cognitive tests such as the 11-item Alzheimer's Disease Assessment Scale-Cognitive (ADAS-COG11) [290], and with the FDG-PET based hypometabolic convergence index (HCI) [87], which is computed from the same subject's FDG-PET image and is a single measurement of the extent to which the pattern and magnitude of cerebral hypometabolism in an individual's FDG-PET image correspond to that in AD patients. Such correlation analysis may help evaluate whether the proposed ventricular morphometry is linked to cognition or abnormal levels of AD-related markers that were previously reported. A Pearson correlation method is applied to analyze the relationship between the ventricular shape morphometry and cognitive or FDG-PET measures, where the latter is used as the predictor. The *p*-value of the correlation is estimated at every surface point to build the correlation *p*-map. The estimated *r*-value, i.e., the correlation coefficient on each surface point, is also computed. Similar to group difference analysis, the overall significance value of the correlation, corrected for multiple comparisons, is obtained through a permutation test (5,000 iterations) of cognitive or other AD biomarker values.

3.3 Experimental Results

3.3.1 Subjects

High-resolution brain structural MRI scans were acquired at multiple ADNI sites using 1.5 Tesla MRI scanners manufactured by General Electric Healthcare, Siemens Medical Solutions, and Philips Medical Systems. For each subject, the T1-weighted MRI scan was collected with a sagittal 3D MP-RAGE sequence. Typical 1.5T acquisition parameters are repetition time (TR) of 2,400 ms, minimum full excitation time (TE), inversion time (TI) of 1,000 ms, flip angle of 8°, 24 cm field of view. The acquisition matrix was $192 \times 192 \times 166$ in the x, y, and z dimensions and the voxel size was $1.25 \times 1.25 \times 1.2\ \mathrm{mm}^3$. In-plane, zero-filled reconstruction (i.e., sinc interpolation) generated a 256×256 matrix for a reconstructed voxel size of $0.9375 \times 0.9375 \times 1.2\ \mathrm{mm}^3$.

Based on the availability of both volumetric MRI and FDG-PET data, 133 subjects were selected from the MCI group in the ADNI baseline dataset, including 71 subjects (age: 74.77 ± 6.81) who developed incident AD during the subsequent 36 months, which we call the MCI converter group, and 62 subjects (age: 75.42 ± 7.83 years) who did not convert during the same period, which we call the MCI stable group. These subjects were chosen on the basis of having at least 36 months of longitudinal data. If a subject developed incident AD more than 36 months after baseline, it was assigned to the MCI stable group. All subjects underwent thorough clinical and cognitive assessment at the time of acquisition, including the Mini-Mental State Examination (MMSE) score [157], Alzheimer's disease assessment scale – Cognitive (ADAS-COG) [290] and Auditory Verbal Learning Test (AVLT) [291]. The demographic information of the subjects is in Table 3.1.

	Gender (M/F)	Education	Age	MMSE at Baseline
MCI Converter (N = 71)	45/26	15.99 ± 2.73	74.77 ± 6.81	26.83 ± 1.60
MCI Stable (N = 62)	44/18	15.87 ± 2.76	75.42 ± 7.83	27.66 ± 1.57

Table 3.1. Demographic information of studied MCI subjects in ADNI baseline dataset.

3.3.2 Volume and Area Differences between Diagnostic Groups

We first tested if there were significant differences between two groups (MCI converter vs. stable) with two global measurements of shape changes: the total volumes and surface areas of the ventricles. In each experiment, the volumes or areas of the left and right ventricles were combined to form a 1×2 vector (V_l, V_r) or (A_l, A_r) for the permutation test with 5,000 random assignments of subjects to groups, given 0.05 as the significant level. However, neither of them detected significant differences between the groups. The permutation test corrected p-values are 0.0803 for the volume and 0.2922 for the area.

3.3.3 Group Difference Analysis with Tensor-based Morphometry

A group comparison was performed with Student’s *t* test on the smoothed TBM features after registering the ventricular surfaces with the proposed method. Specifically, for all points on the ventricular surface, a permutation test with 5,000 random assignments of subjects to groups was run to estimate the statistical significance of the areas with group differences in surface morphometry. The probability was color coded on each surface point as the statistical *p*-map of group difference. Figure 3.6 shows the *p*-map of group difference detected between the MCI converter (N = 71) and stable (N = 62) groups, using the smoothed TBM as a measure of local surface area change and the significance level at each surface point as 0.05. In figure 3.6, the non-blue color areas denote the statistically significant difference areas between two groups. The overall significance of the map is 0.0172.

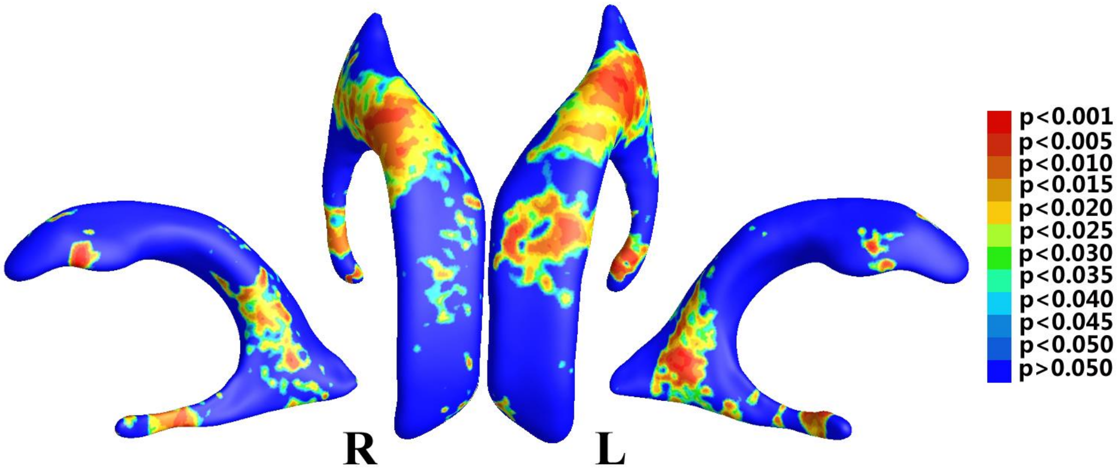

Figure 3.6. Illustration of statistical map showing local shape differences (*p*-values) between MCI converter and MCI stable groups from the ADNI baseline dataset, based on tensor-based morphometry (TBM), which was smoothed by the heat kernel smoothing method [277].

3.3.4 Correlation Analysis of Ventricular Morphometry with Cognitive Measurements

This experiment studied the correlation between the smoothed surface TBM statistic and three cognitive measurements, including MMSE score [157], ADAS-COG11 [290] and AVLT [291] on the 133 subjects with MCI. After the permutation tests, the correlation with ADAS-COG11 passed the multiple comparisons (the overall significance of the correlation value $p = 0.0110$) while the correlations with MMSE and AVLT did not pass the multiple comparisons test (the overall significance of the correlation value $p = 0.8516$ for MMSE and $p = 0.4358$ for AVLT). Figure 3.7 (a) shows the p-map of correlation results with ADAS-COG11, where the non-blue color areas denote the statistically significant difference areas; (b) shows the r-map of the r-values where the red color denotes a positive correlation and the blue color a negative correlation. In the statistically significant areas in figure 3.7 (a), the maximum r-value is 0.3701, the average r-value is 0.1548, and the dominant correlations are positive (86.18%).

3.3.5 Correlation Analysis of Ventricular Morphometry with HCI

Since all subjects included in this study had both structural MRI and FDG-PET images, this experiment attempted to study whether ventricular morphometry features were correlated with FDG-PET based single global index HCI. If such a correlation holds, one may use MRI measures as surrogates of disease progression in AD, even in pre-clinical stages (for related work, please see [101, 106, 292-294]). Prior studies showed that HCI correlated with AD progression and smaller hippocampal volumes [295-298].

The smoothed TBM statistic of the 133 MCI patients was correlated with their HCI measurements, with the permutation test corrected p-value as 0.0001. Figure 3.8 (a) shows the correlation *p*-map color-coded with uncorrected *p*-values and (b) shows the *r*-map color-coded with the correlation coefficients. On the statistically significant areas in figure 3.8 (a), the maximum *r*-value is 0.5163, the average *r*-value is 0.3030, and the dominant

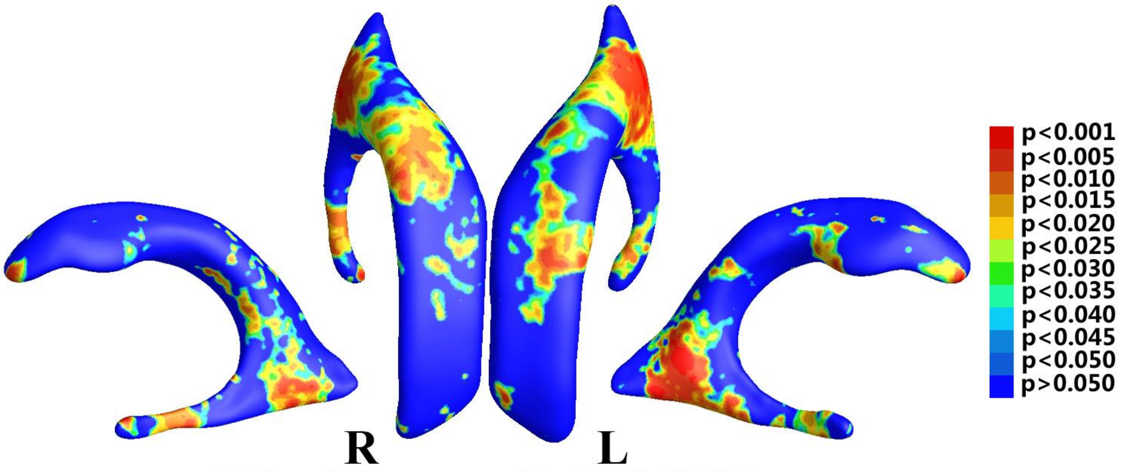

(a) Correlation p-map with ADAS-COG11

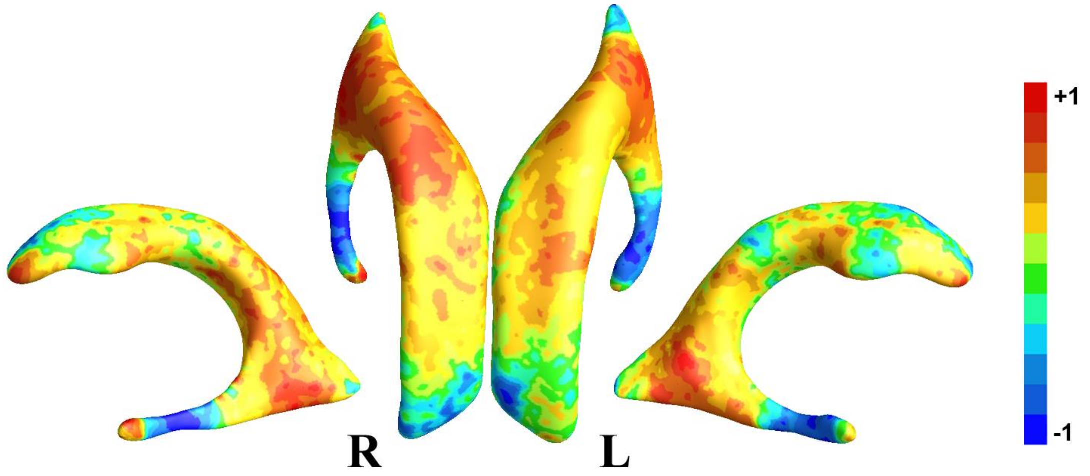

(b) Correlation r-map with ADAS-COG11

Figure 3.7. Correlation maps with ADAS-COG11. (a) shows the *p*-map of correlation results with ADAS-COG11, where the non-blue color areas denote the statistically significant difference areas; (b) shows the *r*-map of the *r*-values where the red color denotes a positive correlation and the blue color a negative correlation.

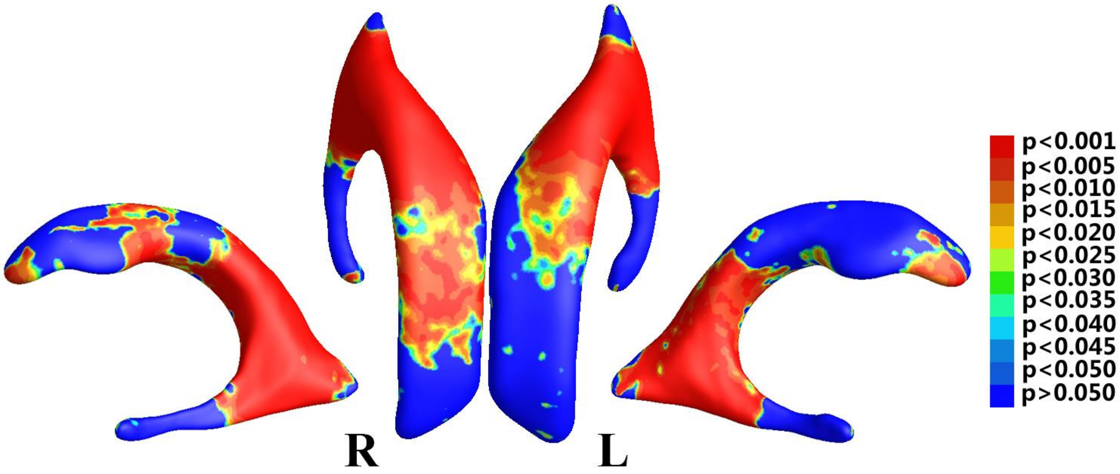

(a) Correlation p-map with HCI

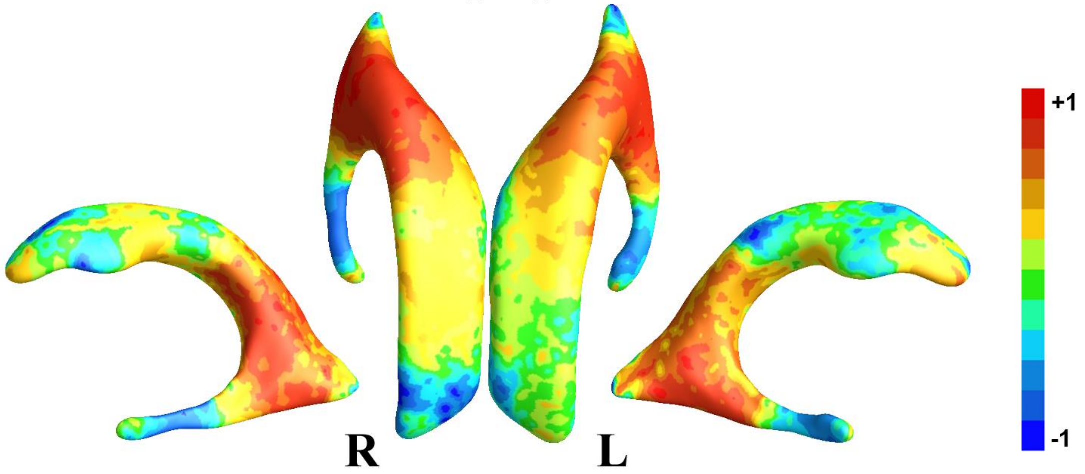

(b) Correlation r-map with HCI

Figure 3.8. Correlation maps with HCI. (a) shows the *p*-map of correlation results with HCI, where the non-blue color areas denote the statistically significant difference areas; (b) shows the *r*-map of the *r*-values where the red color denotes a positive correlation and the blue color a negative correlation.

correlations are positive (99.40%). It is interesting to note that the enlargement of lateral ventricles in these patients was correlated with higher HCI, implicating enlarged ventricles were associated with greater glucose uptake reduction. Such positive correlation was observed in multiple locations. Of special interest and relevant to reported AD hypometabolism were the regions in the neighborhood of posterior cingulate.

3.4 Discussion

This study has two main findings. First, it demonstrates the feasibility to apply hyperbolic geometry to register ventricular surfaces across subjects. In brain imaging, a surface-based morphometry analysis approach is to set up parametric grids on surfaces, and then use differential geometry to come up with useful descriptors of surface features of interest, or to summarize the geometry as a whole. Prior research has used sphere [96, 299, 300] or Euclidean plane [27, 79] as the parameter domain. However, for ventricular surfaces with a branching structure, as demonstrated in [79], spherical mapping creates distortions and planar mapping some inevitable singularities. The hyperbolic Ricci flow method [1, 44, 45] is capable of parameterizing complex shapes. Thus it has the potential to detect subtle differences between people with high accuracy and categorize them into diseased and healthy control groups, or as in the current study categorize them into different risk levels of disease, by analyzing ventricular surface deformation tensors computed from a set of parametric surfaces using concepts from hyperbolic conformal parameterizations. In addition, the introduced hyperbolic Ricci flow method is theoretically sound and numerically efficient [1, 2, 263]. Together with geodesic curve lifting and the Klein model, the proposed computational framework may achieve a diffeomorphic ventricular surface registration with consistent boundary matching condition. Second, the surface tensor-based morphometry, which is computable from the conformal grid, carries rich information on local surface geometry that is defined at the coordinates of the well-organized surface grid.

As demonstrated in many prior studies [29, 30, 32, 118], the resulting set of surface tensor methods practically encodes a great deal of information that would otherwise be inaccessible, or overlooked. The analysis of parametric meshes for computational studies of ventricular structures can be made more powerful by analyzing the surface metric tensor information inherent in the surface.

The proposed method was validated in our ongoing work on MCI conversion prediction [301] which examined baseline measurements of structural MRI and FDG-PET, in combination with cognitive tests, to distinguish individuals with MCI who developed incident AD from those who did not, with the aim of establishing their usefulness as predictors for progression to AD. This work focused on ventricular morphometry analysis. Although the analyses of global ventricular volume and surface area did not differentiate MCI converter and MCI stable groups, our fine-grained analysis revealed significant differences mostly localized around the subregion of the ventricular body that abuts medial temporal lobe structures. This subregional ventricular enlargement was reported to correlate with atrophy of medial temporal lobe which includes the hippocampal formation. Consistent with prior observations, e.g. [86, 289], our findings suggest that grey matter atrophy starts from the temporal lobe region and then spreads to involve frontal cortices, consistent with Braak staging of neurofibrillary pathology [302]. Importantly, they provide evidence that ventricular subfield analysis provides enhanced statistical power in structural MRI analysis compared with ventricular volume analysis. Some recent studies [303-305] found that including optimum features from multiple modalities provides better AD predictive value than any one measure alone. The proposed ventricular surface TBM features may enhance the predictive value of MRI-derived data in AD research.

Furthermore, the positive correlation between ventricular morphometry and ADAS-COG11 that this study found is consistent with previous studies that correlated ventricular expansion with worsening cognition in MCI subjects [306, 307]. The strong positive correlation with HCI values supports the validity of the proposed algorithm and demonstrates the linkage between functional abnormalities and structural changes (ventricular enlargement particularly in this study). As shown in the Sec. 3.3, the ventricular subregions where the statistically significant correlation between ventricular enlargement and HCI abutted areas of earliest FDG-PET change in AD, particularly the posterior cingulate [308-310], and to our knowledge, this is the first study to explore the relationship between ventricular measures and FDG-PET measures.

Applicability to other brain structures. As stated by the uniformization theorem, any surface with a negative Euler characteristic number admits a hyperbolic background geometry and can be conformally mapped to the hyperbolic space $\mathbb{H}^2$. Geometrically, the Euler characteristic number is defined as $2 - 2\mathrm{g}$ for closed surfaces, where g is the surface genus, i.e., the number of handles on a surface, and is defined as $2 - 2\mathrm{g} - \mathrm{b}$ for surfaces with boundaries, where b is the number of boundaries. Thus the hyperbolic Ricci flow method has broad applicability in human brain surface morphometry studies, as surfaces of brain structures are often irregular and topologically complicated. Take the cortical surface as an example. In human brain mapping field, a diffeomorphic mapping between a pair of cortical surfaces with landmark correspondence is usually pursued to study brain deformations along with disease progression. By slicing a cortical surface open along three or more landmark curves, the cortical surface becomes a genus-0 surface with multiple boundaries, which has a negative Euler number. Figure 1.2 (d) [81] illustrates the application of the proposed method on a cortical surface with three landmark curves, which is homotopic to the topological pants. For cortical surfaces with more landmarks, which also have negative Euler numbers, the hyperbolic Ricci flow method is still applicable [4, 5], so the remaining processes of the proposed method follow naturally. On the other hand, for different brain structures, certain processing steps in the pipeline may need to be adapted accordingly. For example, a major difference between cortical and ventricular surface processing with the proposed method is the topology optimization. Given the highly variable gyral patterns of cortical surfaces, one may need to work with experienced neuroanatomists to manually or automatically label homologous landmark curves across subjects following some well-established anatomical protocols such as [311], as described in prior work [2, 80]. In this case, the topology optimization reduces to slicing a cortical surface along a set of landmark curves to change it into a genus-0 surface with multiple boundaries. Chapter 4 will introduce the application of the proposed method on cortical surfaces with six automatically labeled landmark curves, where the hyperbolic harmonic map [4] is used to diffuse the surface registration constructed by this work to a global harmonic map.

Comparison with holomorphic 1-form algorithm. The holomorphic 1-form algorithm [312] is a commonly used method to analyze lateral ventricular surfaces [27]. However, due to the limitation of holomorphic 1-form itself, this method introduces singularities and the number of singularities equals the absolute value of the Euler characteristic number of a surface. In analyzing lateral ventricular surfaces, each surface has a singular point, as shown in figure 3.9 (a), which was called zero point in [312] and [27] and used as the starting point to segment a ventricular surface into three parts, the superior horn, the

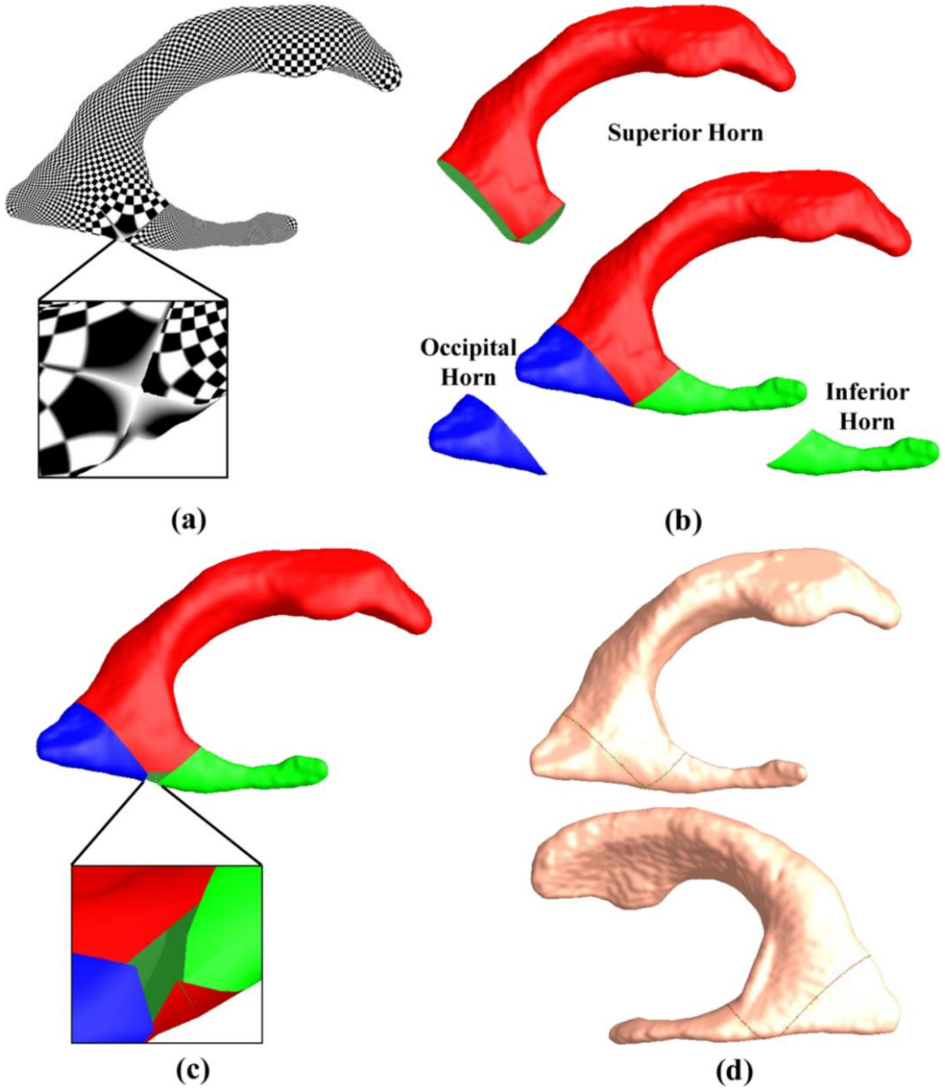

Figure 3.9. Lateral ventricular surface parameterization with a method based on holomorphic 1-forms [312]. Due to the property of holomorphic 1-forms, the ventricular surface parameterization has a zero point (a). In [312], the ventricular surface was segmented with curves traced from the zero point and each horn was mapped to the parameter domain and registered separately (b). After registering each part separately and merging them back together, the ventricular surface has a hole at the zero-point position (c). Surface registration is also affected by the locations of the cuts that divide a ventricular surface into three parts (d).

inferior horn, and the occipital horn, as shown in figure 3.9 (b). After registering the three horns separately and merging them to form the whole registered ventricular surface, a hole is generated around the zero point due to the changes from surface registration, as shown in figure 3.9 (c), which is not reasonable in analyzing anatomical surfaces. On the other hand, the new registration introduces no holes as shown in figure 3.6. Furthermore, the segmentation of ventricular surfaces with holomorphic 1-form, though consistent, separates an entire surface into independent partitions. The independent registrations of different partitions are based on matching surface features which should not be separated. For example, when registering the superior horn, the other two horns are not affected, which may not be true when registering the ventricular surfaces as a whole. Particularly, as shown in figure 3.6, as most of the significantly different areas concentrated at the locations of the partition cuts, the statistical analysis may be affected by the segmentations. Another problem with the ventricular surface segmentation is that the surface registration may be affected by the locations of the cuts that divide a ventricular surface into three parts. As shown in figure 3.9 (d), the locations of the cuts on a left ventricular surface (shown in two different views) were slightly changed, where the original cuts are shown in green, and the changed cuts are shown in red. Although the cutting locations almost overlap, the resulting registered ventricular surfaces are different. By measuring the differences with the Euclidean distances between pairs of vertices on the two registered surfaces, the differences are in the range of [0.0001, 1.3545]. Even more careful studies are necessary to determine the impact of the cutting locations on the statistical analysis. Thus it is advantageous for the new algorithm as it takes the ventricular surface as an entirety for the registration.

Comparison with SPHARM. SPHARM [161], as introduced in Sec. 2.3.5, is another surface mapping tool with a number of applications [165-168]. Briefly, it takes a binary image segmentation as input and provides functions such as surface reconstruction, spherical harmonic mapping and surface registration; statistical analysis tools are also included. The major limitation of SPHARM is that it assumes the input binary image segmentation has a spherical topology. Thus prior work on ventricular shape morphometry with SPHARM usually discarded the inferior horn [168, 186]. The inclusion of the long and narrow inferior horn in our segmentation makes the shape of the lateral ventricle non-spherical. As a result, SPHARM cannot successfully parameterize the concave ventricular surfaces that are reconstructed from our segmentation unless a coarse resolution is used. For this experiment, the segmented binary images were resampled into a resolution of $2 \times 2 \times 2\ \mathrm{mm}^3$. However, the resulting spherical parameterizations still have severe distortion and overlap on the inferior horn, as shown in figure 3.10 (a), and 22 subjects failed the parameterization process. After surface registration, the TBM statistic was computed at each vertex of the aligned surfaces as described in Sec. 3.2.7 and group difference was analyzed as in Sec. 3.2.8. The significance p-map of group comparison between 58 converters and 53 stable MCI subjects with SPHARM is shown in figure 3.10 (b). The result of the proposed method is shown in figure 3.10 (c) and the cumulative distribution function (CDF) plots in figure 3.10 (d) show the comparison of the resulting p-values for each method. As described in Sec. 2.3.6, while the line $y = x$ represents null hypothesis, which implies there is no detectable difference, a steeper curve suggests that greater differences are detected. The details of the experiment with SPHARM can be found in Appendix B. From the CDF comparison, both methods got comparable results, but the proposed method is more robust for processing the concave ventricular surfaces.

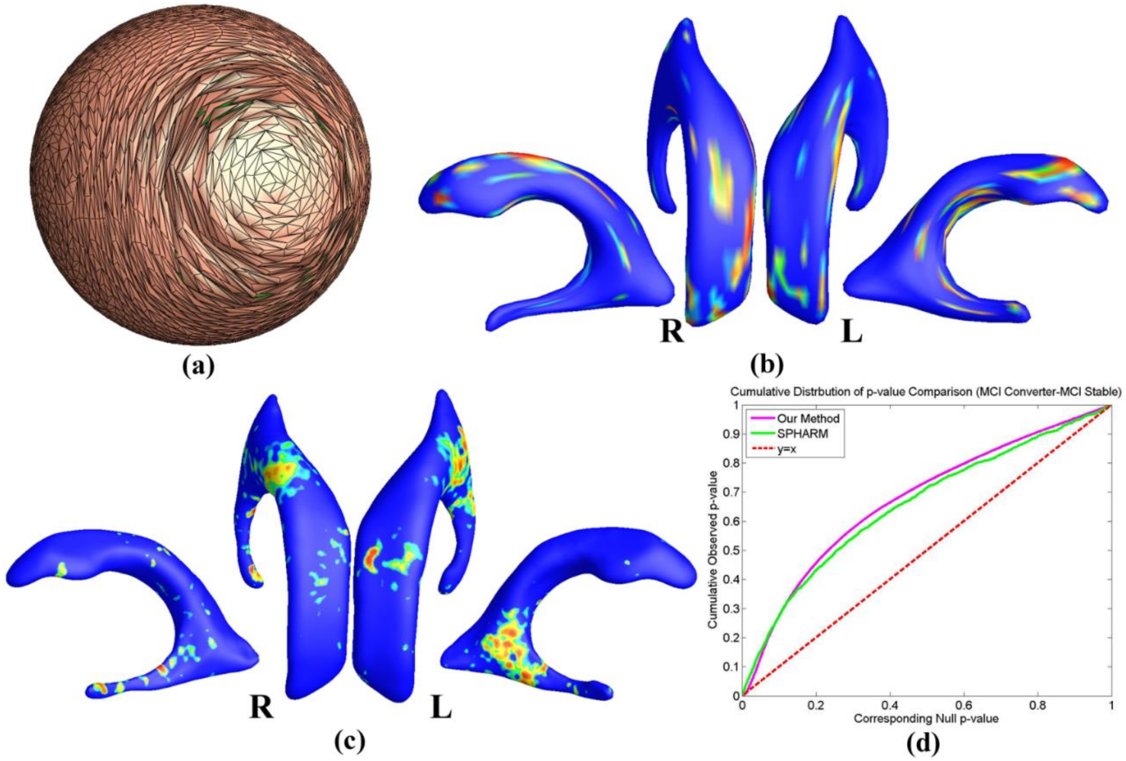

Figure 3.10. Comparison with SPHARM. (a) is the spherical harmonic mapping of a left ventricular surface; (b) is the statistical map from SPHARM [161] showing local shape differences (*p*-values) between MCI converter (*N* = 58) and MCI stable (*N* = 53) groups from the ADNI baseline dataset; (c) is the statistical map from the proposed method showing local shape differences (*p*-values) between the same groups as in (b); (d) shows the CDF plots comparing the two methods.

The inferior horn on the lateral ventricle is also important for the study of AD, as it is adjacent to the hippocampus and its enlargement may indicate hippocampal atrophy – a well-established biomarker for AD. As shown in figure 3.6, our approach detected significant differences on both left and right inferior horns. Even with a smaller dataset, the proposed method detected significant differences on the right inferior horn, as shown in figure 3.10 (c). The significance *p*-maps of the two methods are not quite consistent, most probably because that details in the original image segmentations were greatly removed during the resolution resampling step of SPHARM. A more convincing way to validate the new algorithm is to apply it to study cortical surface morphometry and compare the results to other extensively applied cortical analysis tools such as FreeSurfer [26].

Comparisons with voxel-based morphometry and pattern analysis. When studying brain morphology with imaging, the voxel-based morphometry (VBM) method has been extensively developed, improved, and used [313-318]. Briefly, VBM starts by spatially normalizing the T1-weighted image of each individual subject to a template image to establish a voxel-to-voxel correspondence across subjects. The registration process consists of both affine transformation and a nonlinear deformation. After segmenting the registered images into tissue classes, each voxel contains a measure of the probability that it belongs to a specific segmentation class. This quantity can be used to compute other brain anatomical features such as gray matter volume [313]. Voxel-wise statistical analyses are then applied to study local differences in the anatomical features of each tissue class across subjects. The VBM method is available in many major neuroimaging software packages such as FSL and SPM and is efficient and easy to apply. However, the VBM method may have limited accuracy in measuring some aspects of brain morphology, particularly in regions where fine anatomical features are found within brain structures. For example, the cerebral cortex has a highly folded geometry. Many of its anatomical features are built in deep folds. The voxel-wise nature of the VBM method may limit its capability to accurately measure such features and to align these features across subjects. On the other hand, our surface-based method can achieve sub-voxel accuracy when applied to some specific structures. For example, as discussed above, the hyperbolic Ricci flow method can conformally flatten a convoluted cortical surface onto a 2D domain [4]. The flattened cortical surface retains substantial geometric information about the original surface with no singularities or overlap in the mapping, so all features in the cortical folds are well preserved and can be accurately analyzed. Pattern analysis [319-321] is another commonly applied method, which aims to identify the most discriminative disease-related features in brain images or surfaces. Here the proposed method is based on tensor-based morphometry (TBM), which is generalized to deal with 3D surfaces, to study the morphological deformation patterns of ventricular surfaces along with disease progression. The TBM features encode rich information about the local surface geometry, which may be inaccessible or overlooked in other methods [29, 30, 32, 118]. Experimental results in the group difference study illustrate the differentiation power of the TBM features, as shown in figure 3.6. These TBM features may also improve MRI-based diagnostic classification with sparse learning based feature selection method [80]. Despite the many advantages of the proposed method, however, a few issues need to be addressed before it can be established as an attractive alternative to other methods. First, more experiments on large-scale datasets of ventricular and other brain structure surfaces, especially cortical surfaces, are necessary to validate the efficacy of the method. Second, the system needs to be automated to hide the complex details for general users. Third, the ability of TBM features in diagnostic classification needs more systematic study. Future work is needed to address these problems.

Statistical feature smoothing. In the proposed surface registration pipeline, each of the MR image acquisition, image segmentation, surface reconstruction, surface parameterization, and surface registration procedures is expected to introduce noise in the TBM statistical features. The mesh smoothing process introduced in Sec. 2.2.1 is used to reduce the noise from image acquisition, segmentation and partial volume effects in surface reconstruction [266]. The remaining noise and noise introduced in subsequent processes still affect the SNR in the TBM features and the final statistical analysis. Thus, the heat kernel smoothing algorithm [277] has been applied to the TBM features before the group difference and correlation studies, as introduced in Sec. 3.2.7. From Eq. 3.13, the bandwidth of the smoothing process is determined by the number of iterations. As pointed out in [322], the correlation of noise in surface measurements falls off rapidly with distance on the surface, so it is sufficient to use a small kernel bandwidth. For heat kernel smoothing on cortical surfaces, usually applied parameters include bandwidth $\sigma = 1$ and number of iterations $m = 200$ yielding the effective smoothness of $\sqrt{m} = 14.14\, mm$ [323] or even smaller smoothness values such as $6\, mm$ in [322]. Based on these observations, in this work, we set $\sigma = 1, m = 10$, giving the effective smoothness of $3.16\, mm$. As few studies in the literature have validated the performance of the heat kernel smoothing method [324], the smoothing parameters were chosen tentatively. The group difference *p*-map with unsmoothed TBM features is shown in figure 3.11. In figure 3.6, the significant areas are consistent with those in figure 3.11, but the noisy distributions are greatly improved by the smoothing process. Similar comparison studies for correlation-based *p*-maps give similar results. Thus the parameters are suitable for current studies. A potential future work is to quantitatively study the effects of the heat kernel smoothing process on the statistical analysis.

Surface multivariate tensor-based morphometry. In some prior studies [79, 80], the multivariate tensor-based morphometry (mTBM) introduced in Sec. 2.2.5 was proved to be more powerful for checking group differences than other statistics including TBM. Here the proposed system used TBM as the statistic instead of mTBM because for the lateral ventricle, a fluid-filled subcortical structure, its changes vary drastically with normal aging, disease progression, or other brain activities. As the mTBM is very sensitive to local changes, the resulting significantly different areas spread on the ventricular surface even after smoothing, making the results difficult to be interpreted as meaningful anatomical findings or noise from subtle changes. Thus here TBM was used as the measurement of changes.

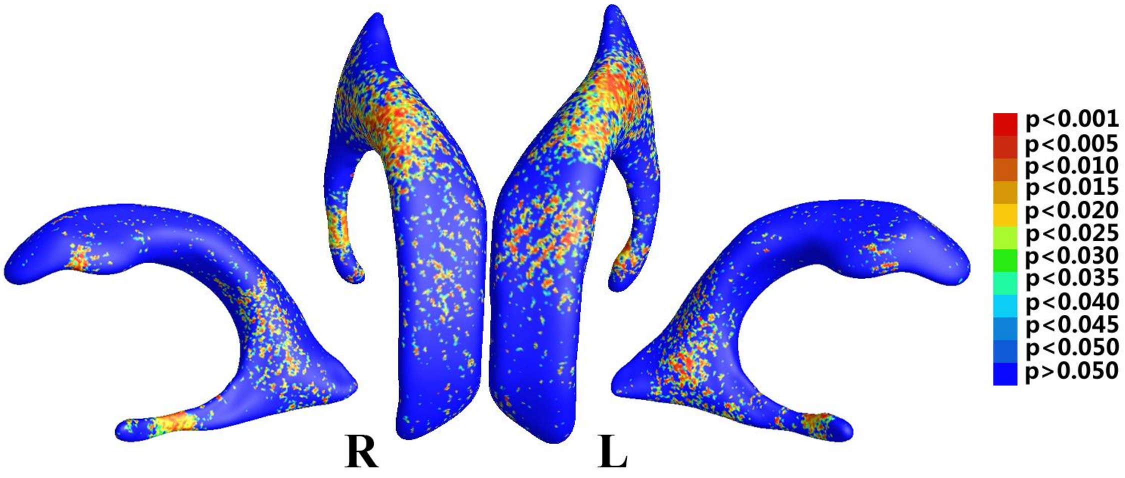

Figure 3.11. Illustration of statistical map showing local shape differences (*p*-values) between MCI converter and MCI stable groups from the ADNI baseline dataset, based on determinant of Jacobian matrix (TBM), which was not smoothed.

Integration of relative pose statistical analysis. In the current study, the proposed surface-based ventricular morphometry system relies on shape changes of the lateral ventricles along with disease progression. Similar to other shape analysis studies of a single structure, ventricular pose information is discarded in this work during the surface registration stage. Pose mainly depends on extrinsic factors such as the position and orientation of a ventricular surface in $\mathbb{R}^3$ while the proposed method depends on the intrinsic factors of the ventricular surfaces such as local enlargement. Although it rarely happens that atrophy of brain tissue causes only pose changes in adjacent structures without any local shape deformation, pose information is still very important in brain morphometry studies. In [212], the statistical analysis of relative pose was presented to study brain atrophy associated pose changes of the subcortical nuclei in AD. Same method was applied in [325] to study pose changes of thalamus due to prematurity and in [326] to study pose changes of corpus callosum due to traumatic brain injury. Briefly, the relative pose is computed by following steps, where we take ventricular surfaces as an example. First, one-to-one point correspondences between different ventricular surfaces are established by a surface registration algorithm, such as the method proposed here. Second, for each registered ventricular surface, a pose matrix is obtained by fitting a template shape to this surface with a Procrustes alignment. Third, the mean pose is calculated iteratively with the pose matrix of each ventricular surface. The relative pose of each ventricular surface, which consists of 7 parameters: 1 scale scalar, 3 rotation scalars and 3 translation scalars, is obtained by subtracting the mean pose from its pose matrix. Statistical analyses are then applied on the relative pose parameters. For details of the algorithm, please refer to [212]. Since the proposed ventricular surface analysis gives indirect information about the atrophy of surrounding brain structures, integration of relative pose analysis in our algorithm may help to better understand the abnormal growth of brain tissue adjacent to lateral ventricles.

This could be a possible future work.

In neuroimaging research, T1-weighted MRI has high contrast differences from surrounding structures making accurate lateral ventricle segmentation straightforward for both manual and automatic methods [84, 85, 106, 327, 328]. Thus structural MRI based lateral ventricular structure has been used to study a variety of human diseases including AD [27, 84, 85, 101, 247, 328, 329], HIV/AIDS [79, 330], normal pressure hydrocephalus [331], ventriculomegaly [168], vascular dementia [331], diabetes mellitus [300], drug addiction [299], and others. The proposed algorithm is very generalizable and may be applied to a similar range of diseases including but not limited to AD. Starting from prior work on brain surface conformal parameterization [4, 5, 25, 44, 45, 131], this work shows that the hyperbolic Ricci flow method can be adopted to analyze branching ventricular morphometry. Besides its global non-singularity parameterization, the proposed method also carries a few other novel ideas, such as using geodesic curve lifting to enforce a meaningful boundary matching, diffeomorphic surface registration via the Klein model, and combing hyperbolic conformal parameterization with TBM analysis. It is expected that this work can provide some practical experience and inspire more interest in hyperbolic geometry related neuroimaging research.

3.5 Conclusion and Future Work

This chapter presented a hyperbolic Ricci flow and surface TBM based ventricular surface registration algorithm, which can improve the computational efficiency and accuracy for in vivo regional structural MRI lateral ventricle estimation. This approach introduced the hyperbolic Ricci flow method which computes a ventricular surface conformal parameterization on the hyperbolic Poincaré disk without any singularity. Through geodesic curve lifting and the conversion to the Klein model [1], a diffeomorphic surface mapping with consistent boundary matching condition was computed. Furthermore, the TBM was computed from the well-organized conformal grids and used to capture any possible subtle surface deformations. The method was applied to our ongoing work on MCI conversion prediction [301] and the results demonstrated that the proposed method achieved good correlation with cognition and other AD biomarker such as FDG-PET, which may help predict longitudinal AD conversion by capturing subtle ventricular morphometric differences from the baseline image analysis.

In the past few years, our group has developed a series of structural MRI analysis software tools for AD research, such as multivariate TBM on cortical surface [80] and hippocampal abnormality analyses [27, 265-267], together with cortical thickness estimation with volumetric Laplace-Beltrami operator and heat kernel [332, 333]. One of the future work is to apply our structural MRI software tools, including this work, in the preclinical AD research [268, 269]. A broad range of research questions on structural MRI analysis [334] need to be carefully explored, such as (1) structural MRI as an AD biomarker to measure AD progression; (2) the relationship of structural MRI to cognition (3) and to other AD biomarkers including amyloid imaging and FDG-PET; and (4) the value for structural MRI measures to help predict cognitive decline.

Furthermore, as discussed above, possible future work that may improve current ventricular surface registration method include (1) algorithm pipeline automation by hiding complex computational details; (2) quantitative evaluation of the effects of different TBM smoothing parameters and automatic choice of the parameters for different brain structures;

and (3) integration of relative pose analysis to analyze the abnormal morphometry of brain tissues adjacent to the studied structure.

CHAPTER 4

SHAPE ANALYSIS WITH HYPERBOLIC WASSERSTEIN DISTANCE

Shape space is an active research field in computer vision and medical imaging study. The shape distance defined in a shape space may provide a simple and refined index to represent a unique shape. Wasserstein distance defines a Riemannian metric for the Wasserstein space. It intrinsically measures the similarities between shapes and is robust to image noise. Thus it has the potential for the 3D shape indexing and classification research. While the algorithms for computing Wasserstein distance have been extensively studied, most of them only work for genus-0 surfaces. This chapter introduces a novel framework to compute Wasserstein distance between general topological surfaces with hyperbolic metric. The computational algorithms are based on Ricci flow, hyperbolic harmonic map, and hyperbolic power Voronoi diagram and the method is general and robust. The method was applied to study human facial expression, longitudinal brain cortical morphometry with normal aging, and cortical shape classification in Alzheimer's disease (AD). Experimental results demonstrate that the proposed method may be used as an effective shape index, which outperforms some other standard shape measures in the AD versus healthy control classification study.

4.1 Introduction

Over the past decade, exciting opportunities have emerged in studying 3D imaging data thanks to the rapid progress made in 3D image acquisition. There is a crucial need to develop effective 3D shape indexing and classification techniques. Shape space models, which usually measure similarities between two shapes by the deformation between them, may provide a suitable mathematical and computational description for shape analysis (as reviewed in [335]). In computer vision research, shape space has been well studied for brain atlas estimation [336, 337], shape analysis [338-340], morphometry study [201, 341], etc. Recently, the Wasserstein space is attracting more attention. The Wasserstein space is the space consisting of all the probability measures on a Riemannian manifold. The Wasserstein distance defines a Riemannian metric for the Wasserstein space and it intrinsically measures the similarities between shapes. The advantages of Wasserstein distance for 3D shape analysis research are: (1) the geodesic distance between space points gives a continuous and refined shape difference measure, which is particularly useful for brain imaging study, where higher accuracy is usually expected; (2) it studies a transport between two probability measures on a canonical image or manifold so it is robust to noise. It holds the potential to quantitatively measure 3D shapes reconstructed from images and provide a theoretical foundation for 3D shape analysis.

Wasserstein distance has been widely studied and applied in image and shape analysis. In [48], the Wasserstein distance was used to model local shape appearances and shape variances for joint variational object segmentation and shape matching. A linear optimal transportation (LOT) framework was introduced in [49], where a linearized version of the Wasserstein distance was used to measure the differences between images. Hong, et al. [342] used Wasserstein distance to encode the integral shape invariants computed at multiple scales and to measure the dissimilarities between two shapes. However, these methods only work with 2D images. In [50], the Wasserstein distance was generalized to Riemannian manifolds, but the method was only applied on genus-0 closed 3D surfaces, where the spherical conformal domain was used as the canonical space for Wasserstein distance computation. To date, few studies have investigated Wasserstein distance defined on general topological surfaces.

In practice, most 3D shapes have complicated topology (high-genus). In brain imaging research, to enforce the alignment of the major anatomic features, one may slice the surfaces open along certain landmark curves [4]. This procedure generates genus-0 surfaces with multiple open boundaries. The current state-of-the-art Wasserstein space research is unable to compute Wasserstein distance on these high-genus surfaces or genus-0 surfaces with multiple open boundaries. Here, to overcome these limitations, I propose a novel framework by integrating hyperbolic Ricci flow [1, 343], hyperbolic harmonic map [4], surface tensor-based morphometry (TBM) [30, 32], and optimal mass transportation map [88, 89]. The computation of the optimal mass transportation map and the Wasserstein distance is also extended to the hyperbolic space, i.e., the Poincaré disk. The resulting Wasserstein distance is called the hyperbolic Wasserstein distance.

The hyperbolic Wasserstein distance was applied in this work to index and compare different 3D shapes. The algorithm was tested on genus-0 surfaces with multiple open boundaries, including human face surfaces with different expressions, longitudinal brain cortical morphology with normal aging, and cortical shape classification between Alzheimer's disease (AD) patients and healthy control people. Experimental results demonstrated that the proposed method is promising to be a new shape analysis tool.

The major contributions can be summarized as follows:

1. Propose a novel algorithm to compute Wasserstein distance between general surfaces with hyperbolic Riemannian metric.

2. Extend the optimal mass transportation map to hyperbolic Poincaré space, which greatly enhance its applicability for general surface analysis.

3. Develop a general framework that may be applicable for other shape space work. Currently, most of shape space work were developed on genus-0 surfaces, e.g. [339, 344], which cannot be directly applied to high-genus surfaces because of the difficulty in building a canonical space for them. The proposed framework, which adopts a hyperbolic harmonic map to build diffeomorphic mappings between general surfaces, may be used to generalize other shape space studies to general surfaces as well.

4.2 Prior Work

Analysis and understanding of shapes is one of the most fundamental tasks in computer vision and medical imaging research. Many 3D shape indexing methods have been proposed and extensively applied. The spherical harmonic analysis [161, 186] and its extension, the weighted spherical harmonic representation [32], use spherical harmonics to match and compare shapes. But these methods require the surfaces to be homotopic to a sphere. The medial description of shapes [39, 184], which is composed of a set of medial samples (m-reps), is also widely applied. Wang et al. introduced a series of conformal invariants to represent and analyze shapes, which are the coordinates of surfaces in the Teichmüller space. The conformal invariants were computed with Euclidean Ricci flow [46] or hyperbolic Yamabe flow [45] and no surface registration was required. In brain imaging studies, the volumes and surface areas of cortical or subcortical structures are often used as biomarkers to characterize brain morphometry associated with cognitive diseases [345].

The optimal mass transportation problem was first raised by Monge, concerning to find an optimal way to move a pile of soil from one place to another with minimal transportation cost [346]. The existence and uniqueness of the solution for the optimal mass transportation problem were proved in [88] using linear programming. The Monge-Kantorovich optimization has been widely applied in various fields, including physics, economics, computer science, etc. Specifically, the optimal mass transportation map provides an important tool for image processing [347, 348]. Recently, the algorithm has been generalized to 3D surfaces for area-preserving mappings [349, 350] and Wasserstein distance computation [50, 340]. However, existing methods only work on genus-0 surfaces, while the proposed algorithm extends the optimal mass transportation problem to general surfaces with hyperbolic metric.

Kendall [47] pioneered the manifold shape space research. In computational anatomy framework [351], the space of diffeomorphisms was carefully studied [352, 353]. In [354, 355], shape space was defined as the space of orbits of the reparameterization group acting on the space of immersions. The reparameterization invariant (RI) metric constructed in [356] used the volume form and the mean curvature of the immersion f, and the metric in [344] used the area multiplication factor of f. Kurtek et al. [357] extended the work in [344] by adding landmark constraints. Jermyn et al. [358] simplified the RI metric computation and Gutman et al. [339] built a Riemannian framework for an intrinsic comparison of the RI metric structure. Lipman and Daubechies [359] introduced a metric for shape comparison based on conformal uniformization and optimal mass transportation. The metric is invariant under Möbius transformation. Later, Lipman et al. [360] provided a convergence analysis of the discrete approximation to the arising mass transportation problems. Mémoli [361] presented a modification and expansion of the original Gromov-Hausdorff notion of distance between metric spaces which considers probability measures defined on measurable subsets of metric spaces.

4.3 Theoretical Background

This section briefly introduces the most relevant concepts and theories. For details, please refer to [40] for computational conformal geometry, and to [88, 89] for optimal mass transportation map.

Please refer to Sec. 3.2.3 for the concepts of conformal deformation, uniformization theorem, and Poincaré disk model. Suppose z_1 and z_2 are two points in the Poincaré disk, the hyperbolic distance between them is defined as

$$\mathrm{dist}(z_1, z_2) = \tanh^{-1}\left|\frac{z_1 - z_2}{1 - z_1\overline{z_2}}\right| \tag{4.1}$$

Surface Ricci Flow. The uniformization metric of a surface can be computed by the Ricci flow method. The normalized surface Ricci flow is defined as $\frac{d\mathbf{g}(t)}{dt} = \left(\frac{4\pi\chi(S)}{A(0)} - 2K(t)\mathbf{g}(t)\right)$, where $A(0)$ is the total area of S at time 0, $K(t)$ is the Gaussian curvature induced by $\mathbf{g}(t)$ and $\chi(S)$ is the Euler characteristic number of S. It has been proved that if $\chi(S) < 0$, the solution to the normalized Ricci flow equation exists for all $t > 0$ and converges to a metric with constant Gaussian curvature $\frac{2\pi\chi(S)}{A(0)}$ [279]. Thus, the hyperbolic uniformization metric of a surface, which introduces -1 Gaussian curvature everywhere, can be computed by the Ricci flow.

Fuchsian Group. Suppose $\{S, \mathbf{g}\}$ is a surface with a negative Euler characteristic number and its hyperbolic uniformization metric is $\tilde{\mathbf{g}}$. Let $p \in S$ be a base point, two loops through p are homotopic, if one can deform to the other without leaving S. All the homotopic classes of loops starting from p form a simply connected surface $\tilde{S}$. Then the universal covering space of S, $\{\tilde{S}, \tilde{\mathbf{g}}\}$, can be isometrically embedded in $\mathbb{H}^2$. A Fuchsian transformation ϕ is a Möbius transformation that maps a universal covering space $\tilde{S}$ to another and preserves the projection $\phi \circ p = p$. All Fuchsian transformations form the Fuchsian group, $Fuchs(S)$. The Fuchsian transformations are also called deck transformations, as introduced in Sec. 3.2.5.

Harmonic Map. Given a surface$\{S, \mathbf{g}\}$, if the coordinates (x, y) satisfy $\mathbf{g} = e^{2u(x,y)}(dx^2 + dy^2)$, where u is the conformal factor, (x, y) are called the isothermal coordinates. Consider a map $f: \{S_1, \mathbf{g}_1\} \rightarrow \{S_2, \mathbf{g}_2\}$, z and w are the local isothermal coordinates on S_1 and S_2, respectively. We denote $f(z) = w$ and $\mathbf{g}_1 = \sigma(z)dzd\bar{z}$, $\mathbf{g}_2 = \rho(w)dwd\bar{w}$, where $z, w \in \mathbb{C}$ and $z = x + iy, w = u + iv$, $dz = dx + idy$, $d\bar{z} = dx - idy$. The harmonic energy of the map f is defined as

$$E(f) = \int_{S_1} \rho(f(z))(|f_z|^2 + |f_{\bar{z}}|^2)\, dxdy \tag{4.2}$$

where $f_z = \frac{1}{2}\left(\frac{\partial f}{\partial x} - i\frac{\partial f}{\partial y}\right)$, $f_{\bar{z}} = \frac{1}{2}\left(\frac{\partial f}{\partial x} + i\frac{\partial f}{\partial y}\right)$.

If f is a critical point of the harmonic energy, then it is called a harmonic map. The necessary condition for f to be a harmonic map is the Euler-Lagrange equation $f_{z\bar{z}} + \frac{\rho_f}{\rho} f_z f_{\bar{z}} \equiv 0$. The following theorem [362] shows that harmonic maps with hyperbolic metrics are beneficial for general surface registration study.

Theorem 4.1 (Yau): Suppose $f: \{S_1, \mathbf{g}_1\} \rightarrow \{S_2, \mathbf{g}_2\}$ is a degree one harmonic map, furthermore, the Riemannian metric on S_2 induces negative Gaussian curvature, then for each homotopy class, the harmonic map is unique and diffeomorphic.

Optimal Mass Transportation Map. Given a Riemannian manifold $\{S, \mathbf{g}\}$, let μ and ν be two probability measures on S with the same total mass, i.e., $\int_S \mu dx = \int_S \nu dx$, let $\phi: S \to S$ be a diffeomorphic map, then the pull-back measure induced by ϕ is $\phi^* \nu = \det(J)\, \nu \circ \phi$, where J is the Jacobian matrix of ϕ. If the pull-back measure satisfies $\phi^* \nu = \mu$, then the map ϕ is measure preserving. The transportation cost of ϕ is defined as

$$\mathrm{Cost}(\phi) = \int_S d_{\mathbf{g}}^2\left(p, \phi(p)\right)\mu(p) dx \tag{4.3}$$

where p is a vertex on S and $d_{\mathbf{g}}(p, \phi(p))$ is the geodesic distance between p and its image $\phi(p)$ with respect to the metric $\mathbf{g}$. The optimal mass transportation problem tries to find the measure preserving mapping, which uses minimal transportation cost (Eq. 4.3).

Wasserstein Space and Wasserstein Distance. Given a Riemannian manifold $\{S, \mathbf{g}\}$, the Wasserstein space is defined as:

Definition 4.1 (Wasserstein Space): Let $P_n(S)$ denote the space of all probability measures μ on S with finite n^{th} moment, where $n \geq 1$. Suppose there exists some point $p_0 \in S$, such that $\int_S d_{\mathbf{g}}^n(p, p_0)\mu(p) dx < +\infty$.

Given two measures μ and ν in $P_n(S)$, the Wasserstein distance between them is defined as the cost of the optimal mass transportation map $\phi: S_\mu \to S_\nu$.

$$W_n(\mu, \nu) = \inf_{\phi^* \nu = \mu} \left(\int_S d_{\mathbf{g}}^n\left(p, \phi(p)\right)\mu(p) dx\right)^{\frac{1}{n}} \tag{4.4}$$

Theorem 4.2 [363]: The Wasserstein distance W_n is a Riemannian metric of the Wasserstein space $P_n(S)$.

4.4 Computational Algorithms

This section explains the computation framework of the hyperbolic Wasserstein distance. Genus-0 surfaces with multiple boundaries are used as examples to illustrate the algorithm. The pipeline is summarized in Algorithm 4.1 and illustrated in Fig. 4.1.

Algorithm 4.1. Hyperbolic Wasserstein Distance Computation Pipeline.

---

1. Slice the surface open along some delineated landmark curves to generate a genus-0 surface with multiple boundaries (Fig. 4.1 (a)).
2. Compute the hyperbolic uniformization metric of the surface with hyperbolic Ricci flow.
3. Isometrically embed the surface onto the Poincaré disk and convert it to the Klein model (Fig. 4.1 (b)-(c)).
4. With the Klein model, construct the initial mapping between the surface and a template surface with the constrained harmonic map.
5. Improve the initial mapping with hyperbolic harmonic map to obtain a global diffeomorphic mapping on the Poincaré disk (Fig. 4.1 (d)).
6. Compute the optimal mass transportation map between the surface and the template surface with the hyperbolic power Voronoi diagram, where the surface tensor-based morphometry of the hyperbolic harmonic map is used as a measure (Fig. 4.1 (e)).
7. Compute the hyperbolic Wasserstein distance between the surface and the template surface.

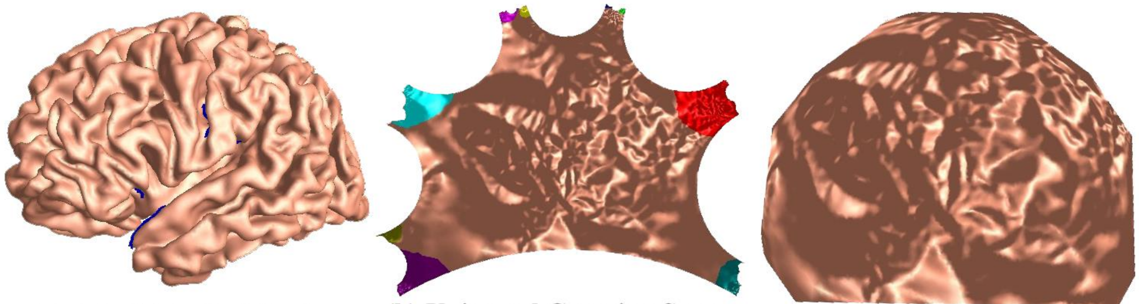

(a) A Left Cortical Surface with Multiple Boundaries **(b) Universal Covering Space of (a) in the Poincaré Disk** **(c) Klein Model of (a)**

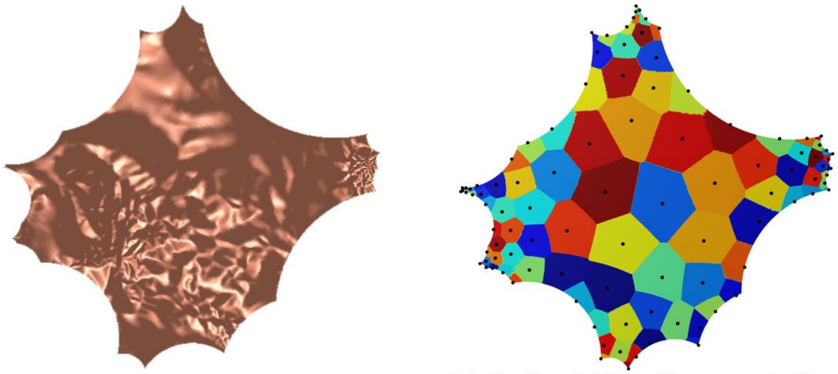

(d) Hyperbolic Harmonic Map of (a) to a Template **(e) Optimal Mass Transportation Map of (a) to a Template with the Hyperbolic Power Voronoi Diagram**

Figure 4.1. Algorithm pipeline: (a) slice a surface open along landmark curves to generate a genus-0 surface with multiple boundaries; (b) embed the surface onto the Poincaré disk with its hyperbolic uniformization metric, which is computed by the hyperbolic Ricci flow; (c) covert the Poincaré disk to the Klein model to construct the initial map between the surface and a template; (d) compute the hyperbolic harmonic map by diffusing the initial map; (e) compute the optimal mass transportation map using hyperbolic power Voronoi diagram, with surface tensor-based morphometry as the probability measure, where the colored regions denote Voronoi cells.

4.4.1 Topology Optimization

Surfaces with negative Euler characteristic numbers admit hyperbolic geometry. For closed surfaces with genus $g \geq 2$, their hyperbolic uniformization metric can be directly computed with hyperbolic Ricci flow. For genus-0 surfaces, we usually slice them open along multiple (3 or more) boundaries, as shown in Fig. 4.1 (a). This process is called topology optimization and is usually applied in medical imaging research [2, 4, 343], where landmark curve matchings are often enforced across subjects.

4.4.2 Discrete Hyperbolic Ricci Flow

The computational algorithm of discrete hyperbolic Ricci flow with gradient descent optimization is introduced in Sec. 3.2.4. This section describes the hyperbolic Ricci flow algorithm with Newton's method [1, 2], which is more stable and efficient.

Similar to Sec. 3.2.4, $M(V,E,F)$ denotes a triangular mesh, where V is the vertex set, E is the edge set, and F is the face set, respectively. The circle packing metric of M is defined in the same form as Sec. 3.2.4, (Γ, Φ), where $\Gamma = \{\gamma_i\}: V \rightarrow \mathbb{R}^+$ and $\Phi = \{\phi_{ij}\}: E \rightarrow \left[0, \frac{\pi}{2}\right]$. The gradient of the hyperbolic Ricci energy (Eq. 3.9) is $\nabla E(U) = \left(\frac{\partial E}{\partial u_1}, \frac{\partial E}{\partial u_2}, \dots, \frac{\partial E}{\partial u_n}\right) = (K_1, K_2, \dots, K_n)$, where n is the number of vertices. Then the elements in the Hessian matrix H are $h_{ii} = \frac{\partial K_i}{\partial u_i}$, $h_{ij} = \frac{\partial K_i}{\partial u_j}$, $i, j = 1,2, \dots, n$. Define $\tau_{ij} = \sinh(\gamma_i)\cosh(\gamma_j) + \cosh(\gamma_i)\sinh(\gamma_j)\cos(\phi_{ij})$, we have

$$\frac{\partial K_i}{\partial u_i} = \sinh(\gamma_i) \times \sum_{f_{ijk}} \frac{CB-DA}{A\sqrt{A^2-B^2}}, \frac{\partial K_i}{\partial u_j} = \sinh(\gamma_j) \times \sum_{f_{ijk}} \frac{EB-FA}{A\sqrt{A^2-B^2}} \tag{4.5}$$

where

$$A = \sinh(l_k)\sinh(l_j)$$

$$B = \cosh(l_k)\cosh(l_j) - \cosh(l_i)$$

$$C = \tau_{ij}\sinh\left(l_j\right)\frac{\cosh(l_k)}{\sinh(l_k)} + \tau_{jk}\sinh(l_k)\frac{\cosh(l_j)}{\sinh(l_j)}$$

$$D = \tau_{ij}\cosh\left(l_j\right) + \tau_{ki}\cosh(l_k)$$

$$E = \tau_{ji}\sinh(l_j)\frac{\cosh(l_k)}{\sinh(l_k)}$$

$$F = \tau_{ji}\cosh(l_j) - \tau_{jk}$$

Algorithm 4.2 summarizes the hyperbolic Ricci flow method with Newton's optimization.

Algorithm 4.2. Hyperbolic Ricci flow with Newton’s Optimization

```
Input: triangular mesh $M(V, E, F)$.
Output: hyperbolic uniformization metric of $M$.
1. Compute the initial circle radius $\gamma_i$ for each vertex $v_i$ and the weight $\phi_{ij}$ for each edge $e_{ij}$.
2. Set the target Gaussian curvature as zero.
3. repeat
    (1) Compute the edge lengths with Eq. 3.6, face corner angles with Eq. 3.4, and the Gaussian curvature with Eq. 3.5.
    (2) For each vertex $v_i$, compute $\frac{\partial K_i}{\partial u_i}$ and $\frac{\partial K_i}{\partial u_j}$ with Eq. 4.5 and construct the Hessian matrix $H$.
    (3) Solve the linear system $H\Delta U = -2K$.
    (4) Update $u_i$ for vertex $v_i$ with $u_i \leftarrow u_i + \Delta u_i$.
```

(5) Update γ_i for vertex v_i with Eq. 3.7.

until the resulting Gaussian curvature of all vertices is less than a user-defined threshold.

4.4.3 Initial Map Construction

With the hyperbolic uniformization metric, the surface can be isometrically embedded onto the Poincaré disk, using the method in Sec. 3.2.5. Then a finite portion of the universal covering space of the surface is tiled with Fuchsian group generators, as shown in Fig. 4.1 (b). The computation of the Fuchsian transformations is introduced in Sec. 3.2.5. With the geodesic curve lifting algorithm (Sec. 3.2.6), the canonical Poincaré disk of the surface is obtained, where all boundaries become geodesics. We then convert the Poincaré disk to the Klein model (Eq. 3.10), which is a hyperbolic polygon with all the hyperbolic lines coincide with Euclidean straight lines, as shown in Fig. 4.1 (c). With the Klein model, the initial map between the surface and a template surface is constructed using the constrained harmonic map [2, 4, 343], as introduced in Sec. 3.2.6. As indicated in [362], if the target domain is convex, the planar harmonic maps are diffeomorphic. Thus, the constructed initial map is diffeomorphic.

4.4.4 Hyperbolic Harmonic Map

The initial map is then diffused to form the hyperbolic harmonic map [4]. Given two surfaces M and N with hyperbolic metrics $\mathbf{g}_M$ and $\mathbf{g}_N$, respectively, their local isothermal coordinates are denoted as z and w. Suppose $f: M \to N$ is the initial map, locally, it can be written as $f(z) = w$. Then the diffusion process is given by the following gradient descent method

$$\frac{df(z,t)}{dt} = -[f_{z\bar{z}} + \frac{\rho_w(w)}{\rho(w)} f_z f_{\bar{z}}] \tag{4.6}$$

where $\rho(w) = \frac{1}{(1-w\bar{w})^2}$ is the hyperbolic metric in the Poincaré disk. Algorithm 4.3 gives the detailed computation steps. A hyperbolic harmonic map example is illustrated in Fig. 4.1 (d).

Algorithm 4.3. Hyperbolic Harmonic Map

---

1. Given two surfaces $\{M, \mathbf{g}_M\}$ and $\{N, \mathbf{g}_N\}$, where $\mathbf{g}_M$ and $\mathbf{g}_N$ are hyperbolic metrics in the Poincaré disk. There is a one-to-one correspondence between these two surfaces, (m_i, n_i), where m_i and n_i are vertices on M and N, respectively.

2. For each pair of corresponding vertices $m_i \in M$ and $n_i \in N$, embed their one-ring neighboring vertices onto the Poincaré disk. Let z_i and $w_i = f(z_i)$ denote the 2D coordinates of m_i and n_i in the Poincaré disk, respectively.

3. Compute $\frac{dw_i(z_i,t)}{dt}$ with Eq. 4.6.

4. Update $w_i^{t+1} = w_i^t - \epsilon \frac{dw_i(z_i,t)}{dt}$.

5. Compute the new 3D coordinates of n_i with the new w_i.

6. Repeat steps 2 to 5, until $\frac{dw_i(z_i,t)}{dt}$ is less than a user-specified threshold.

In this work, surface tensor-based morphometry (TBM) [30, 32] of the hyperbolic harmonic map is used to define the probability measure on the Poincaré disk. The computation of the TBM is detailed in Sec. 3.2.7.

4.4.5 Optimal Mass Transportation Map and Hyperbolic Wasserstein Distance

As shown in [50, 340], the optimal mass transportation map between two probability measures that are defined on surfaces can be computed by the power Voronoi diagram [364]. Here we use the hyperbolic space as the canonical space and TBM as the measure to compute the power Voronoi diagram on the Poincaré disk.

Given a surface S with the Riemannian metric $\mathbf{g}$, let $P = \{p_1, p_2, \dots, p_n\}$ be a set of n discrete points on S and $\boldsymbol{w} = \{w_1, w_2, \dots, w_n\}$ be the weights defined on each point.

Definition 4.2 (Power Voronoi Diagram): Given a point set P and its corresponding weight vector $\boldsymbol{w}$, the power Voronoi diagram induced by $(P, \boldsymbol{w})$ is a cell decomposition of the surface $\{S, \mathbf{g}\}$, such that the cell spanned by p_i is given by

$$\mathrm{Cell}_i = \left\{x \in S \middle| d_{\mathbf{g}}^2(x, p_i) - w_i \le d_{\mathbf{g}}^2(x, p_j) - w_j\right\}, j = 1,2, \dots, n \text{ and } i \neq j \qquad (4.7)$$

In this work, with the Poincaré disk model, the geodesic distance $d_{\mathbf{g}}$ between two points is defined by Eq. 4.1. The term $d_{\mathbf{g}}^2(x, p_i) - w_i$ is called the power distance between x and p_i. Figure 4.2 (a) shows the power distance on the Euclidean plane. Figure 4.2 (b) illustrates the power Voronoi diagram on the Poincaré disk.

Theorem 4.3: Given a Riemannian manifold $\{S, \mathbf{g}\}$, μ and ν represent two probability measures defined on S and they have the same total mass. ν is a Dirac measure, with discrete point set support $P = \{p_1, p_2, \dots, p_n\}$ and $\nu(p_i) = \nu_i$. Then there exists a weight vector $\boldsymbol{w} = \{w_1, w_2, \dots, w_n\}$, unique up to a constant, such that the power Voronoi diagram induced by $(P, \boldsymbol{w})$ gives the optimal mass transportation map between μ and ν:

$$\psi\colon \mathrm{Cell}_i \to p_i, i = 1,2, \dots, n$$

and

$$\int_{\mathrm{Cell}_i} \mu(x)dx = \nu_i, \forall i \in [1, \dots, n]$$

The proof of Theorem 4.3 can be found in [50].

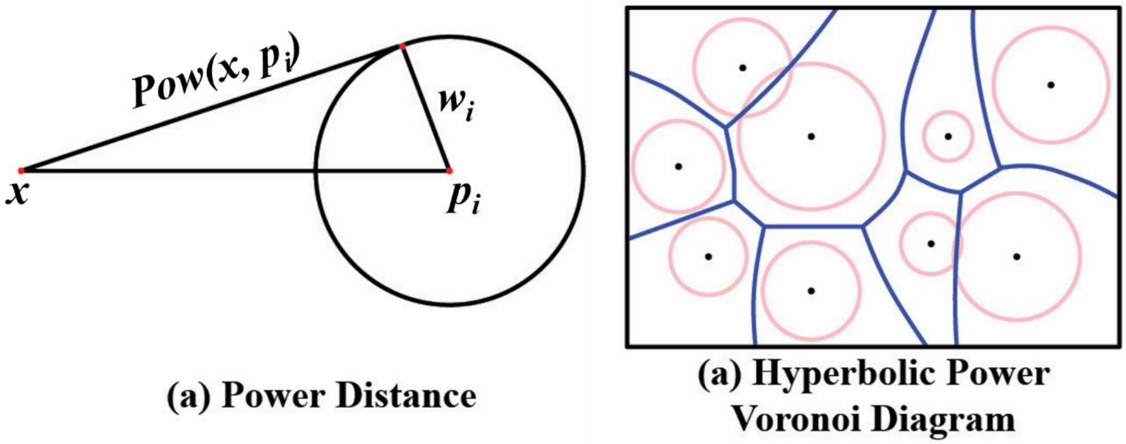

(a) Power Distance

(a) Hyperbolic Power Voronoi Diagram

Figure 4.2. Illustration of the power distance between two points on the Euclidean plane and the power Voronoi diagram on the Poincaré disk.

The optimal weight for the power Voronoi diagram that induces the optimal mass transportation map can be computed by

$$\frac{dw_i}{dt} = \nu_i - \int_{\mathrm{Cell}_i} \mu(x)\, dx, x \in S \tag{4.8}$$

Algorithm 4.4 gives the details about the optimal mass transportation map computation with hyperbolic metric. Figure 4.1 (e) illustrates the hyperbolic power Voronoi diagram that results in the optimal mass transportation map between the cortical surface in Fig. 4.1 (a) and a template cortical surface. In Fig. 4.1 (e), the black points form the discrete point set P. The initial hyperbolic geodesic Voronoi diagram is computed by the method in [365].

Algorithm 4.4. Optimal Mass Transportation Map

```
1. Given a triangular mesh $M$ with hyperbolic metric $\mathbf{g}$ on the Poincaré disk, define a measure $\mu$ and a Dirac measure $(P, \nu) = \{(p_i, \nu_i)\}, i = 1, 2, \ldots, n$, $\int_M \mu(x)dx = \sum_{i=1}^{n} \nu_i$.
2. For each $p_i \in P$, compute it geodesic distance to every other vertex on $M$ with Eq. 4.1.
3. For each vertex $v_i \in M$, determine which Voronoi cell it belongs to with Eq. 4.7.
4. For each $p_i \in P$, compute the total mass of the measures in the cell spanned by it, $\mu_i = \int_{\mathrm{Cell}_i} \mu(x)dx$.
5. Update each weight by $w_i^{t+1} = w_i^t + \epsilon(\nu_i - \mu_i)$.
6. Repeat steps 3 to 5, until $|\nu_i - \mu_i|, \forall i$, is less than a user-specified threshold.
```

The cost of the optimal mass transportation map computed by Algorithm 4.4 gives the Wasserstein distance between two measures. With the hyperbolic metric, we define the hyperbolic Wasserstein distance between two measures that are defined on the Poincaré disk by

$$\mathrm{Wasserstein}(\mu, \nu) = \sum_{i=1}^{n} \int_{\mathrm{Cell}_i} \left(\tanh^{-1} \left|\frac{x - p_i}{1 - x\overline{p_i}}\right|\right)^2 \mu(x)dx \tag{4.9}$$

4.5 Experimental Results

4.5.1 Human Facial Expression Analysis

In the first experiment, the proposed method was applied to study 3D human face expression. Human facial expression modeling is an interesting problem studied for a long time [366]. The goal is to discriminate and describe different human facial expressions. It is useful for face recognition and dynamical facial animation research.

Three face meshes were selected from the BU-3DFE Database [337], including an angry face (Fig. 4.3 (a)), a happy face (Fig. 4.3 (b)), and a happier face (Fig. 4.3 (c)), which all belong to a randomly selected sample. On each face surface, two eyes and the mouth were removed along their boundaries, a common approach used in 3D face modeling [1]. The resulting facial surface became a genus-0 surface with four open boundaries. The happy face was used as the template surface to compute the hyperbolic harmonic map and the optimal mass transportation map. First, we ran hyperbolic Ricci flow on the three surfaces and isometrically embedded them on the Poincaré disk, as shown in Fig. 4.3 (d-f). Then, the angry and happier faces were registered to the happy face with the hyperbolic harmonic map (Fig. 4.3 (g)). Finally, with the TBM measures, the optimal mass transportation maps were constructed between both faces and the template face with the hyperbolic power Voronoi diagram (Fig. 4.3 (h)). Later, the hyperbolic Wasserstein distances between the angry face and the template face, between the happier face and the template face, were computed as the costs of respective optimal mass transportation maps. Intuitively, the happier face is more similar to the template, thus it should have smaller Wasserstein distance. The experimental results verify our intuition, where the hyperbolic Wasserstein distances for the angry face and happier faces are 25.94 and 11.75, respectively. Although multi-subject studies are clearly necessary, this experiment demonstrates that the hyperbolic Wasserstein distance may have the potential to quantify and measure human expression changes.

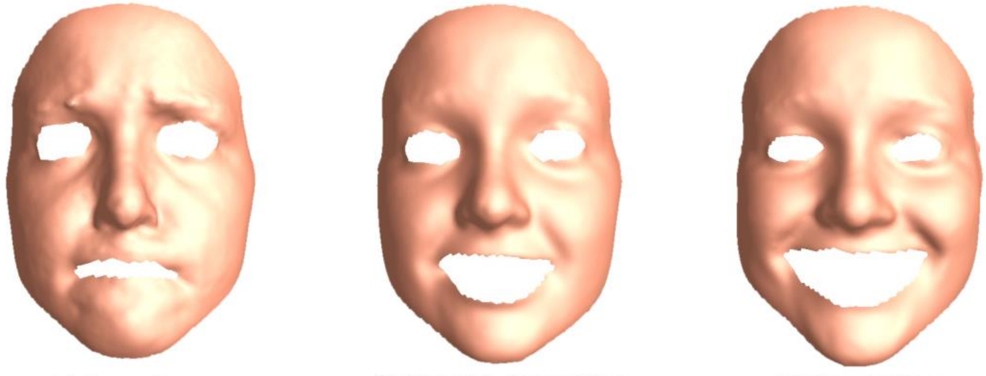

(a) Angry Face **(b) Template Happy Face** **(c) Happier Face**

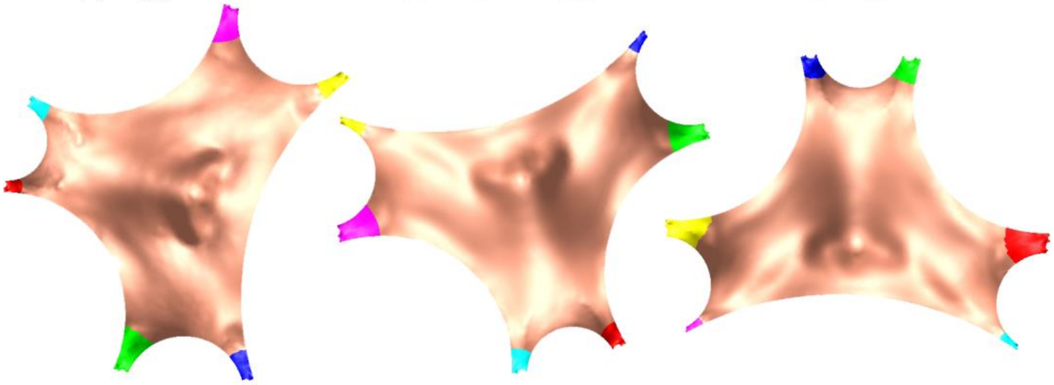

(d) Universal Covering Space of (a) in the Poincaré Disk **(e) Universal Covering Space of (b) in the Poincaré Disk** **(f) Universal Covering Space of (c) in the Poincaré Disk**

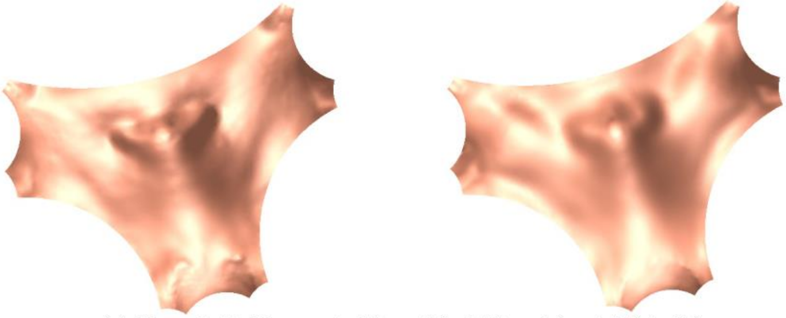

(g) Hyperbolic Harmonic Map of (a, left) and (c, right) to (b)

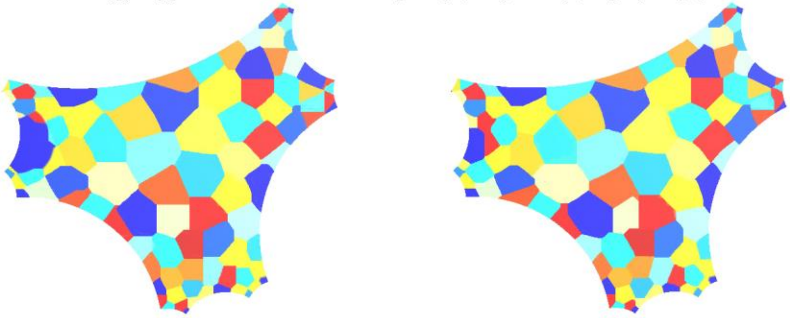

(h) Optimal Mass Transportation Maps of (a, left) and (c, right) to (b)

Figure 4.3. Experimental results of human facial expression analysis with hyperbolic Wasserstein distance.

4.5.2. Longitudinal Cortical Morphometry Analysis

This experiment applied the proposed algorithm to analyze cortical surface morphology in normal aging. Brain atrophy seems to be inevitable for elderly people [86]. However, a simple, non-invasive brain imaging biomarker would be beneficial to quantify brain morphometry change patterns and identify abnormal changes potentially for early interventions.

An elderly heathy subject (85-year old male) was randomly selected from the Alzheimer's Disease Neuroimaging Initiative (ADNI) [367]. The longitudinal structural magnetic resonance images (MRIs) at three time points, the baseline, 12 months, and 24 months after screening, were studied. The structural MRIs were preprocessed using FreeSurfer [26] to reconstruct the cortical surfaces. Only the left hemispheric cerebral cortices were used here. Six major brain landmark curves were automatically labeled on each cortical surface with the Caret software package [55], including the Central Sulcus, Anterior Half of the Superior Temporal Gyrus, Sylvian Fissure, Calcarine Sulcus, Medial Wall Ventral Segment, and Medial Wall Dorsal Segment, as shown in Fig. 4.4.

After we cut the cortical surfaces along the delineated landmark curves, they became genus-0 surfaces with six open boundaries. The baseline cortical surface was used as the template and the same analysis as in Sec. 4.5.1 was done. The hyperbolic power Voronoi diagrams for the 12-month and 24-month cortical surfaces are shown in Fig. 4.5. The hyperbolic Wasserstein distances between the template surface and the 12-month and 24-month surfaces are 132.28 and 201.70, respectively, revealing the cortex changing process along with normal aging [368]. This shows that the proposed method may serve as an imaging index to study the longitudinal brain morphometry.

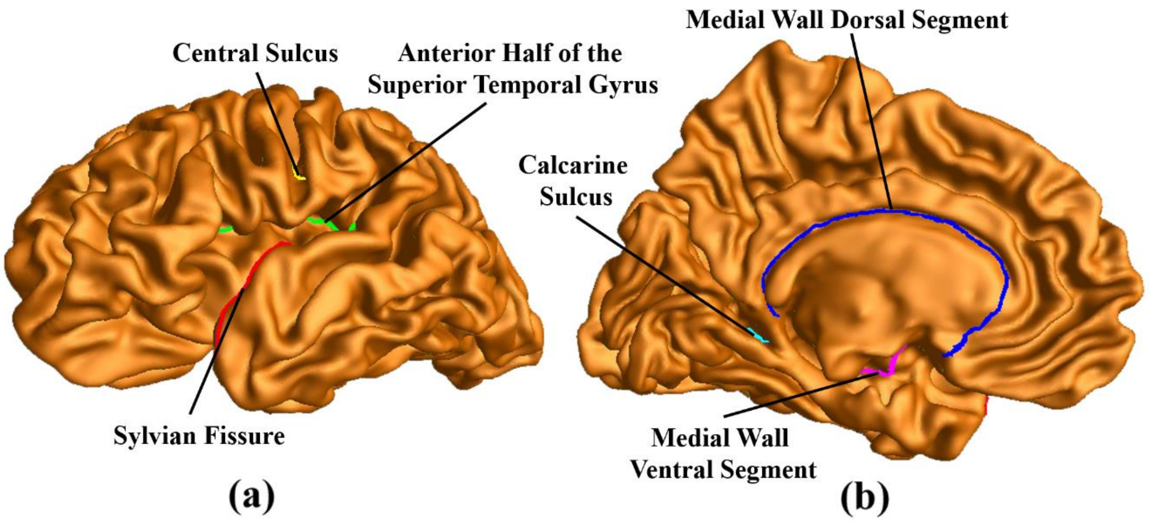

Figure 4.4. Landmark curves on a left cortical surface, which are automatically labeled by Caret [55], showing in two different views.

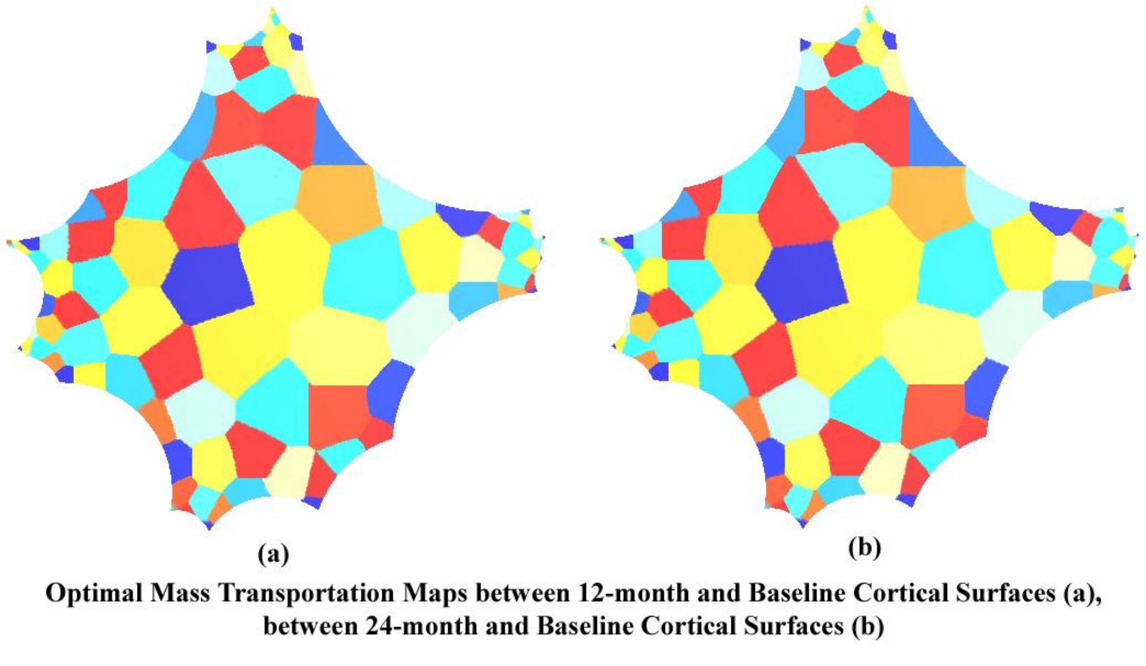

Figure 4.5. Optimal mass transportation maps between the 12-month, 24-month cortical surfaces and baseline surface with hyperbolic power Voronoi diagram.

4.5.3 Cortical Shape Classification

The hyperbolic Wasserstein distance was also applied to study the classification problem with cortical surfaces between healthy control subjects and AD patients. Thirty AD patients and thirty healthy controls were randomly selected from the ADNI baseline dataset. The inclusive rules were based on segmentation and reconstruction result quality of the FreeSurfer package [26]. Only left hemispheric cortices were studied here, as some prior research, e.g. [267], has identified a trend that AD related brain atrophy may starts from left side and subsequently extends to the right. The left cortical surface of a healthy control subject, who is not in our 60 studied subject dataset, was randomly selected as the template surface. Similar to Sec. 4.5.2, Caret was used to automatically identify six landmark curves on each cortical surface. After cutting open the cortical surfaces along the landmark curves, we modeled each left hemispheric cortical surface as a genus-0 surface with six open boundaries and computed the hyperbolic Wasserstein distance between each cortical surface and the common template surface.

With the computed hyperbolic Wasserstein distances, the complex tree in the Statistics and Machine Learning Toolbox of MATLAB was used as a classifier. With a 5-fold cross validation, the classification rate of the proposed method is 76.7%. As a comparison, we also computed two other standard cortical surface shape features, the cortical surface area and cortical surface volume. The same classifier was applied on the two measurements with 5-fold cross validation. Their results are summarized in Table 4.1. It can be noticed that the new method significantly outperformed them. Generally speaking, the discrimination of the AD progression and normal aging is challenging, but has numerous benefits to help design early interventions. Whether or not the new approach provides a more accurate way to quantify the cortical changes than those afforded by other criteria (such as SPHARM [161], radial distance [369], or Teichmüller shape space coordinates [44-46]) requires careful validation for each application. If statistical power is increased in shape feature representation, this would support the use of 3D modeling techniques in advanced brain imaging research. Meanwhile, this work may build a theoretical foundation to extend other shape space work to general surfaces to further improve AD imaging biomarkers for preclinical AD research.

Method	Classification Rate
Hyperbolic Wasserstein distance	76.7%
Surface area	41.7%
Surface volume	51.7%

Table 4.1. Classification rate comparison of the hyperbolic Wasserstein distance and two other cortical surface shape features, the cortical surface area and cortical surface volume. The results demonstrated a higher accuracy rate achieved by the proposed method.

4.6 Conclusion and Future Work

This work introduced a novel algorithm to compute the Wasserstein distance between general surfaces with hyperbolic metric. With hyperbolic Ricci flow, hyperbolic harmonic map, surface TBM, and hyperbolic power Voronoi diagram, the hyperbolic Wasserstein distance was computed. This method generalized the optimal mass transportation and Wasserstein space work to general surfaces. In the experiments, the algorithm was applied to study human facial expression changes, cortical longitudinal morphometry and cortical shape classification in AD.

In future, the new algorithm should be further validated with more 3D brain imaging data and its potential to be generalized to other shape space work needs to be explored. Another possible future work is to improve the performance of the algorithm by considering other probability measures for the optimal mass transportation map, such as the multivariate tensor-based morphometry (mTBM) [70], as introduced in Sec. 2.2.5.

CHAPTER 5

SUMMARY

This dissertation presented three novel surface-based shape analysis methods based on mathematical theories and computational algorithms from conformal geometry. The proposed algorithms have been applied to study brain shape morphometry associated with Alzheimer's disease (AD).

With holomorphic 1-form based surface conformal parameterization [27, 79], the proposed surface fluid registration algorithm extended the inverse consistent image fluid registration method to match general surfaces. Compared to prior work [28], application of conformal parameterization in the proposed method resulted in a concise surface registration formula, which is easy to understand and implement. Furthermore, as the area distortion correction term in the Navier-Stokes equation was reduced to a scalar function, which can be evaluated before the registration, the new method is also stable and efficient. Integration of the multivariate tensor-based morphometry (mTBM) [69, 80] in the proposed framework may boost the statistical power to detect subtle changes in the surfaces, as mTBM is able to retain full information in the deformation tensor. The algorithm was applied to study the effects of AD symptoms and Apolipoprotein E $\epsilon 4$ (ApoE4) gene on hippocampal atrophy, with data from the Alzheimer's Disease Neuroimaging Initiative (ADNI) baseline dataset. The new method outperformed two other widely applied subcortical shape analysis tools, FIRST and SPHARM [161], in group comparisons between different diagnostic groups. Also, the ApoE4 genetic influence on hippocampal atrophy was found, for the first time, in the non-demented ADNI baseline cohort, which consists of mild cognitive impairment (MCI) patients and healthy people. The examples of matching various hippocampal surfaces are relevant for mapping how degenerative diseases affect the brain, as well as building statistical shape models to detect the anatomical effects of disease, aging, or development. The hippocampus was used as specific examples, but the method is general and is applicable in principle to cortical and other subcortical surfaces. Furthermore, the surface-based fluid registration system automated the matching of surfaces by computing a correspondence field guided by the differences of features between the surfaces. This is a natural idea, in that it uses conformal parameterization to transform a surface matching problem into an image registration problem. Whether or not this approach provides a more relevant correspondence than those afforded by other criteria (mutual information, neural nets, or hand landmarking) requires careful validation for each application. Optimal correspondence depends more on utility for a particular application than on anatomical homology. Because different correspondence principles produce different shape models, a systematic comparison of their efficacy for detecting group differences and genetic influence in brain structures is necessary.

Surface conformal parameterization with holomorphic 1-forms is linear and stable. However, its major limitation is that it generates singularity points and the number of singularity points equals the absolute value of the Euler number of the surface [40]. There are no curvilinear coordinates defined on the singularity points. When using the resulting parameter domain for surface registration, the surfaces have to be segmented into pieces with respect to the singularity points and separate pieces are registered independently [79]. Thus, although surface fluid registration algorithm works in principle for a wide range of cortical or subcortical surfaces, resulting registration may not be meaningful in the anatomical sense. In brain imaging study, surfaces of many brain structures have non-zero, particularly, negative Euler numbers, such as the lateral ventricles and cortical surfaces with multiple landmark curves. For these surfaces, conformal parameterization with hyperbolic Ricci flow [1] provides a better solution. The resulting parameterization has minimal angle distortion and no singularities. To start, a surface registration algorithm for ventricular morphometry study was proposed based on hyperbolic Ricci flow and tensor-based morphometry (TBM) [32]. The approach applied the hyperbolic Ricci flow method to compute a singularity-free ventricular surface conformal parameterization onto the hyperbolic Poincaré disk. Through geodesic curve lifting and the conversion to the Klein model, a diffeomorphic surface registration with consistent boundary matching conditions was constructed. Furthermore, the TBM was computed from the well-organized conformal grids and used to capture any possible subtle surface deformations. The algorithm was applied to our ongoing work on MCI conversion prediction with the ADNI baseline dataset. Experimental results demonstrated that the proposed method achieved good correlation with cognition and other AD biomarker such as FDG-PET [87], which may help predict longitudinal AD conversion by capturing subtle ventricular morphometric differences from the baseline image analysis.

Shape space theory has been extensively applied in computer vision and medical imaging. Wasserstein space is composed of all probability measures that are defined on a Riemannian manifold. Wasserstein distance defines a Riemannian metric for the Wasserstein space and it can intrinsically measure the similarities between different shapes. The Wasserstein distance is continuous, accurate, and robust to image noise, thus it may provide a succinct and refined descriptor for 3D shape indexing and classification. However, existing algorithms for Wasserstein distance computation only work with 2D images [48, 49, 342] or genus-0 closed 3D surfaces [50], which greatly limit its applications. This dissertation presents a novel algorithm to compute Wasserstein distance between general topological surfaces. Briefly, with hyperbolic Ricci flow [1] and hyperbolic harmonic map [4], a global diffeomorphic registration can be established between any two general surfaces that are homotopic to each other. Then the TBM of the registration naturally defines a probability measure on the template surface. Using the hyperbolic Poincaré disk of the template surface as the canonical parameter space, the Wasserstein distance between two TBM measures can be computed by the optimal mass transportation map [88, 89], which is also extended to the hyperbolic space. The new Wasserstein distance is called hyperbolic Wasserstein distance. The algorithm was applied to study cortical shape morphometry in AD, with a set of cortical surfaces from the ADNI baseline dataset. Experimental results demonstrated that the proposed method outperformed other standard shape measures in the AD vs. healthy control classification study, supporting its potential to be used as an effective shape index for brain imaging study.

Overall, the algorithms in this dissertation helped solve a broad range of problems in shape analysis of brain imaging data. Due to the usage of surface conformal geometry, these algorithms are stable, efficient, and general. They are complimentary to many existing shape analysis methods and may provide new opportunities for many future directions.

REFERENCES

1. Zeng, W., D. Samaras, and X.D. Gu, *Ricci flow for 3D shape analysis.* IEEE Trans Pattern Anal Mach Intell, 2010. **32**(4): p. 662-677.

2. Wang, Y., et al., *Brain Surface Conformal Parameterization with the Ricci Flow.* IEEE Trans Med Imag, 2012. **31**(2): p. 251-264.

3. Huang, H., et al., *A novel surface registration algorithm with biomedical modeling applications.* IEEE Trans Inf Technol Biomed, 2007. **11**(4): p. 474-482.

4. Shi, R., et al. *Hyperbolic Harmonic Mapping for Constrained Brain Registration*. in *IEEE Conf Comp Vis Patt Recog CVPR '13*. 2013.

5. Shi, R., et al. *Hyperbolic Harmonic Brain Surface Registration with Curvature-based Landmark Matching*. in *Information Processing in Medical Imaging, 23rd International Conference (IPMI)*. 2013. Asilomar, CA.

6. Bronstein, A.M., M.M. Bronstein, and R. Kimmel, *Numerical Geometry of Non-Rigid Shapes*. 2008: Springer.

7. van Kaick, O., et al., *A Survey on Shape Correspondence.* Computer Graphics Forum, 2011. **30**(6): p. 1681-1707.

8. Zhang, Z., *Iterative point matching for registration of free-form curves and surfaces.* International Journal of Computer Vision, 1994. **13**(2): p. 119-152.

9. Savoye, Y., *Iterative cage-based registration for dynamic shape capture*, in *ACM SIGGRAPH 2012 Posters*. 2012, ACM: Los Angeles, California. p. 1-1.

10. Besl, P.J. and N.D. McKay, *A method for registration of 3-D shapes.* Pattern Analysis and Machine Intelligence, IEEE Transactions on, 1992. **14**(2): p. 239-256.

11. Brown, B.J. and S. Rusinkiewicz, *Global non-rigid alignment of 3-D scans*, in *ACM SIGGRAPH 2007 papers*. 2007, ACM: San Diego, California. p. 21.

12. Tevs, A., et al. *Isometric registration of ambiguous and partial data*. in *Computer Vision and Pattern Recognition, 2009. CVPR 2009. IEEE Conference on*. 2009.

13. Huang, Q.-X., et al., *Non-rigid registration under isometric deformations*, in *Proceedings of the Symposium on Geometry Processing*. 2008, Eurographics Association: Copenhagen, Denmark. p. 1449-1457.

14. Kim, V.G., Y. Lipman, and T. Funkhouser, *Blended intrinsic maps.* ACM Trans. Graph., 2011. **30**(4): p. 1-12.

15. Ovsjanikov, M., et al., *One Point Isometric Matching with the Heat Kernel.* Computer Graphics Forum, 2010. **29**(5): p. 1555-1564.

16. Yun, Z., et al. *Dense non-rigid surface registration using high-order graph matching*. in *Computer Vision and Pattern Recognition (CVPR), 2010 IEEE Conference on*. 2010.

17. Mateus, D., et al. *Articulated shape matching using Laplacian eigenfunctions and unsupervised point registration*. in *Computer Vision and Pattern Recognition, 2008. CVPR 2008. IEEE Conference on*. 2008.

18. Mémoli, F., *Spectral Gromov-Wasserstein distances for shape matching,* in *2009 IEEE 12th International Conference on Computer Vision Workshops (ICCV Workshops)*. 2009. p. 256-263.

19. Vaillant, M. and J. Glaunes, *Surface matching via currents.* Inf Process Med Imaging, 2005. **19**: p. 381-392.

20. Vaillant, M., et al., *Diffeomorphic metric surface mapping in subregion of the superior temporal gyrus.* Neuroimage, 2007. **34**(3): p. 1149-1159.

21. Tan, M. and A. Qiu. *Multiresolution Diffeomorphic Mapping for Cortical Surfaces*. in *Inf Process Med Imaging*. 2015.

22. Jain, V. and H. Zhang. *Robust 3D Shape Correspondence in the Spectral Domain*. in *IEEE International Conference on Shape Modeling and Applications*. 2006.

23. Lombaert, H., et al., *FOCUSR: Feature Oriented Correspondence using Spectral Regularization - A Method for Precise Surface Matching.* IEEE Transactions on Pattern Analysis and Machine Intelligence, 2013. **35**(9): p. 2143-2160.

24. Shi, Y., et al., *Metric optimization for surface analysis in the Laplace-Beltrami embedding space.* IEEE Trans Med Imaging, 2014. **33**(7): p. 1447-1463.

25. Gu, X., et al., *Genus zero surface conformal mapping and its application to brain surface mapping.* IEEE Trans Med Imag, 2004. **23**(8): p. 949-958.

26. Fischl, B., M.I. Sereno, and A.M. Dale, *Cortical Surface-Based Analysis II: Inflation, Flattening, and a Surface-Based Coordinate System.* NeuroImage, 1999. **9**(2): p. 195-207.

27. Wang, Y., et al., *Surface-based TBM boosts power to detect disease effects on the brain: An N=804 ADNI study.* Neuroimage, 2011. **56**(4): p. 1993-2010.

28. Thompson, P.M., et al., *Mapping cortical change in Alzheimer's disease, brain development, and schizophrenia.* NeuroImage, 2004. **23**(Suppl 1): p. S2-S18.

29. Thompson, P.M., et al., *Growth Patterns in the Developing Human Brain Detected Using Continuum-Mechanical Tensor Mapping.* Nature, 2000. **404**(6774): p. 190-193.

30. Davatzikos, C., *Spatial Normalization of 3D Brain Images using Deformable Models.* J Comput Assist Tomogr, 1996. **20**(4): p. 656-665.

31. Tangelder, J.W. and R.C. Veltkamp, *A survey of content based 3D shape retrieval methods.* Multimedia Tools and Applications, 2008. **39**(3): p. 441-471.

32. Chung, M.K., K.M. Dalton, and R.J. Davidson, *Tensor-Based Cortical Surface Morphometry via Weighted Spherical Harmonic Representation.* IEEE Trans Med Imag 2008. **27**(8): p. 1143-1151.

33. Gutman, B.A., et al., *Hippocampal Surface Analysis Using Spherical Harmonic Function Applied to Surface Conformal Mapping*, in *International Conference on Pattern Recognition – ICPR 2006*. 2006: Hong Kong. p. 964-967.

34. Sun, J., M. Ovsjanikov, and L. Guibas. *A concise and provably informative multi-scale signature based on heat diffusion*. in *Proceedings of the Symposium on Geometry Processing*. 2009. Berlin, Germany: Eurographics Association.

35. Castellani, U., et al., *A New Shape Diffusion Descriptor for Brain Classification*, in *Medical Image Computing and Computer-Assisted Intervention*. 2011. p. 426-433.

36. Raviv, D., et al. *Volumetric heat kernel signatures*. in *Proc. Intl. Workshop on 3D Object Retrieval, ACM Multimedia*. 2010.

37. Blum, H. and R.N. Nagel, *Shape description using weighted symmetric axis features.* Pattern Recognition, 1978. **10**(3): p. 167-180.

38. Fletcher, P.T., et al., *Principal geodesic analysis for the study of nonlinear statistics of shape.* IEEE Trans Med Imaging, 2004. **23**(8): p. 995-1005.

39. Styner, M. and G. Gerig. *Medial models incorporating object variability for 3D shape analysis*. in *Information Processing in Medical Imaging*. 2001.

40. Gu, X. and S.-T. Yau, *Computational Conformal Geometry*. 2008: International Press of Boston.

41. Gu, X., Y. Wang, and S.-T. Yau, *Geometric Compression using Riemann Surface Structure.* Communications in Information and Systems, 2004. **3**(3): p. 171-182.

42. Ben-Chen, M. and C. Gotsman, *Characterizing Shape Using Conformal Factors*, in *the 1st Eurographics conference on 3D Object Retrieval*. 2008. p. 1-8.

43. Gardiner, F.P. and N. Lakic, *Quasiconformal Teichmüller theory*. Mathematical Surveys and Monographs. Vol. 76. 2000: American Mathematical Society.

44. Wang, Y., et al. *Studying Brain Morphology using Conformal Equivalence Class*. in *IEEE 12th International Conference on Computer Vision 2009, ICCV 2009*. 2009.

45. Wang, Y., et al., *Teichmüller shape space theory and its application to brain morphometry*. Med Image Comput Comput Assist Interv Proceedings, 2009. **12**(Pt 2): p. 133-140.

46. Wang, Y., et al., *Shape Analysis with Conformal Invariants for Multiply Connected Domains and its Application to Analyzing Brain Morphology*, in *IEEE Conf. Comp. Vis. Patt. Recog. CVPR '09*. 2009. p. 202-209.

47. Kendall, D.G., *The Diffusion of Shape*. Advances in Applied Probability, 1977. **9**(3): p. 428-430.

48. Schmitzer, B. and C. Schnörr, *Object Segmentation by Shape Matching with Wasserstein Modes*, in *Energy Minimization Methods in Computer Vision and Pattern Recognition*. 2013. p. 123-136.

49. Wang, W., et al., *A linear optimal transportation framework for quantifying and visualizing variations in sets of images*. Int J Comput Vis, 2013. **101**(2): p. 254-269.

50. Su, Z., et al., *Shape Classification Using Wasserstein Distance for Brain Morphometry Analysis*. Inf Process Med Imaging, 2015. **24**: p. 411-423.

51. Christensen, G.E., R.D. Rabbitt, and M.I. Miller, *Deformable templates using large deformation kinematics*. IEEE Trans Image Process, 1996. **5**(10): p. 1435-1447.

52. Shen, D. and C. Davatzikos, *HAMMER: hierarchical attribute matching mechanism for elastic registration*. IEEE Trans Med Imaging, 2002. **21**(11): p. 1421-1439.

53. Yanovsky, I., et al., *Comparing registration methods for mapping brain change using tensor-based morphometry*. Med Image Anal, 2009. **13**(5): p. 679-700.

54. Thompson, P.M. and A.W. Toga, *A surface-based technique for warping 3-dimensional images of the brain*. IEEE Trans. Med. Imag. , 1996. **15**(4): p. 1-16.

55. Van Essen, D.C., et al., *An Integrated Software Suite for Surface-based Analyses of Cerebral Cortex.* J Am Med Inform Assoc, 2001. **8**(5): p. 443-459.

56. Bakircioglu, M., S. Joshi, and M.I. Miller, *Landmark Matching on Brain Surfaces via Large Deformation Diffeomorphisms on the Sphere*, in *Proc. SPIE Medical Imaging*. 1999. p. 710-715.

57. Yeo, B.T., et al., *Spherical demons: fast diffeomorphic landmark-free surface registration.* IEEE Trans Med Imaging, 2010. **29**(3): p. 650-668.

58. Thompson, P.M. and A.W. Toga, *A Framework for Computational Anatomy.* Computing and Visualization in Science, 2002. **5**: p. 1-12.

59. Leow, A., et al., *Brain structural mapping using a novel hybrid implicit/explicit framework based on the level-set method.* NeuroImage, 2005. **24**(3): p. 910-927.

60. Auzias, G., et al., *Diffeomorphic brain registration under exhaustive sulcal constraints.* IEEE Trans Med Imaging, 2011. **30**(6): p. 1214-1227.

61. Zhong, J. and A. Qiu, *Multi-manifold diffeomorphic metric mapping for aligning cortical hemispheric surfaces.* NeuroImage, 2010. **49**(1): p. 355-365.

62. Pantazis, D., et al., *Comparison of landmark-based and automatic methods for cortical surface registration.* NeuroImage, 2010. **49**(3): p. 2479-2493.

63. Qiu, A. and M.I. Miller, *Multi-structure network shape analysis via normal surface momentum maps.* NeuroImage, 2008. **42**(4): p. 1430-1438.

64. Durrleman, S., et al., *Inferring brain variability from diffeomorphic deformations of currents: An integrative approach.* Medical Image Analysis, 2008. **12**(5): p. 626-637.

65. Wang, Y., M.-C. Chiang, and P.M. Thompson, *Mutual Information-Based 3D Surface Matching with Applications to Face Recognition and Brain Mapping*, in *Proceedings of the Tenth IEEE International Conference on Computer Vision (ICCV'05) Volume 1 - Volume 01*. 2005, IEEE Computer Society. p. 527-534.

66. Pitiot, A., et al., *Learning object correspondences with the observed transport shape measure.* Inf Process Med Imaging, 2003. **18**: p. 25-37.

67. Davies, R.H., et al., *A Minimum Description Length Approach to Statistical Shape Modeling.* IEEE Trans. Med. Imag., 2002. **21**(5): p. 525-537.

68. Thodberg, H.H., *Minimum Description Length shape and appearance models.* Inf Process Med Imaging, 2003. **18**: p. 51-62.

69. Lepore, N., et al., *Generalized Tensor-Based Morphometry of HIV/AIDS Using Multivariate Statistics on Deformation Tensors.* IEEE Trans. Med. Imag., 2008. **27**(1): p. 129-141.

70. Wang, Y., et al., *Multivariate Tensor-based Brain Anatomical Surface Morphometry via Holomorphic One-Forms.* Med Image Comput Comput Assist Interv Proceedings, 2009. **12**(Pt 1): p. 337-344.

71. Do Carmo, M.P., *Differential Geometry of Curves and Surfaces*. 1976: Prentice-Hall, Inc.

72. Bronstein, A.M., M.M. Bronstein, and R. Kimmel, *Generalized multidimensional scaling: a framework for isometry-invariant partial surface matching.* Proc Natl Acad Sci U S A, 2006. **103**(5): p. 1168-1172.

73. Schwartz, E.L., A. Shaw, and E. Wolfson, *A Numerical Solution to the Generalized Mapmaker's Problem: Flattening Nonconvex Polyhedral Surfaces.* IEEE Trans. Patt. Anal. Mach. Intell., 1989. **11**(9): p. 1005-1008.

74. Balasubramanian, M., J.R. Polimeni, and E.L. Schwartz, *Exact Geodesics and Shortest Paths on Polyhedral Surfaces.* IEEE Trans. Pattern Anal. and Machine Intell., 2009. **31**(6): p. 1006-1016.

75. Brechbühler, C., G. Gerig, and O. Kübler, *Parametrization of Closed Surfaces for 3-D Shape Description.* Computer Vision and Image Understanding, 1995. **61**(2): p. 154-170.

76. Zhao, X., et al., *Area-Preservation Mapping using Optimal Mass Transport.* IEEE Transactions on Visualization and Computer Graphics, 2013. **19**(12): p. 2838-2847.

77. Angenent, S., et al., *On the Laplace-Beltrami operator and brain surface flattening.* IEEE Trans Med Imaging, 1999. **18**(8): p. 700-711.

78. Hurdal, M.K. and K. Stephenson, *Cortical cartography using the discrete conformal approach of circle packings.* Neuroimage, 2004. **23(**Suppl 1): p. S119-S128.

79. Wang, Y., et al., *Multivariate tensor-based morphometry on surfaces: Application to mapping ventricular abnormalities in HIV/AIDS.* NeuroImage, 2010. **49**(3): p. 2141-2157.

80. Wang, Y., et al., *Applying tensor-based morphometry to parametric surfaces can improve MRI-based disease diagnosis.* NeuroImage, 2013. **74**: p. 209-230.

81. Shi, J., P.M. Thompson, and Y. Wang. *Hyperbolic Ricci Flow and Its Application in Studying Lateral Ventricle Morphometry*. in *Multimodal Brain Image Analysis*. 2012. Springer Berlin Heidelberg.

82. Wang, Y., et al., *Brain Mapping with the Ricci Flow Conformal Parameterization and Multivariate Statistics on Deformation Tensors.* 2nd MICCAI Workshop on Mathematical Foundations of Computational Anatomy, 2008: p. 36-47.

83. Bro-Nielsen, M. and C. Gramkow, *Fast fluid registration of medical images*, in *Visualization in Biomedical Computing (VBC'96).* . 1996, Springer. p. 267-276.

84. Jack, C.R., Jr., et al., *MRI as a biomarker of disease progression in a therapeutic trial of milameline for AD.* Neurology, 2003. **60**(2): p. 253-260.

85. Thompson, P.M., et al., *Mapping hippocampal and ventricular change in Alzheimer's disease.* NeuroImage, 2004. **22**(4): p. 1754-1766.

86. Frisoni, G.B., et al., *The clinical use of structural MRI in Alzheimer disease.* Nat Rev Neurol, 2010. **6**(2): p. 67-77.

87. Chen, K., et al., *Characterizing Alzheimer's disease using a hypometabolic convergence index.* Neuroimage, 2011. **56**(1): p. 52-60.

88. Kantorovich, L.V., *On a Problem of Monge.* Uspekhi Mat. Nauk, 1948. **3**(2): p. 225-226.

89. Brenier, Y., *Polar factorization and monotone rearrangement of vector-valued functions.* Communications on Pure and Applied Mathematics, 1991. **44**(4): p. 375-417.

90. Jack, C.R., Jr., et al., *Comparison of different MRI brain atrophy rate measures with clinical disease progression in AD.* Neurology, 2004. **62**(4): p. 591-600.

91. Ridha, B.H., et al., *Volumetric MRI and cognitive measures in Alzheimer disease : comparison of markers of progression.* J Neurol, 2008. **255**(4): p. 567-574.

92. Wolz, R., et al., *Measurement of hippocampal atrophy using 4D graph-cut segmentation: Application to ADNI.* NeuroImage, 2010. **52**(1): p. 109-118.

93. den Heijer, T., et al., *A 10-year follow-up of hippocampal volume on magnetic resonance imaging in early dementia and cognitive decline.* Brain, 2010. **133**(4): p. 1163-1172.

94. Dewey, J., et al., *Reliability and validity of MRI-based automated volumetry software relative to auto-assisted manual measurement of subcortical structures in HIV-infected patients from a multisite study.* NeuroImage, 2010. **51**(4): p. 1334-1344.

95. Holland, D., et al., *Subregional neuroanatomical change as a biomarker for Alzheimer's disease.* Proc Natl Acad Sci U S A, 2009. **106**(49): p. 20954-20959.

96. Styner, M., et al., *Morphometric analysis of lateral ventricles in schizophrenia and healthy controls regarding genetic and disease-specific factors.* Proc Natl Acad Sci U S A, 2005. **102**(13): p. 4872-4877.

97. Apostolova, L.G., et al., *Subregional hippocampal atrophy predicts Alzheimer's dementia in the cognitively normal.* Neurobiol Aging, 2010. **31**(7): p. 1077-1088.

98. Apostolova, L.G., et al., *3D comparison of low, intermediate, and advanced hippocampal atrophy in MCI.* Hum Brain Mapp, 2010. **31**(5): p. 786-797.

99. Morra, J.H., et al., *Automated mapping of hippocampal atrophy in 1-year repeat MRI data from 490 subjects with Alzheimer's disease, mild cognitive impairment, and elderly controls.* NeuroImage, 2009. **45**(1 Suppl): p. S3-S15.

100. Ferrarini, L., et al., *Ventricular shape biomarkers for Alzheimer's disease in clinical MR images.* Magn Reson Med, 2008. **59**(2): p. 260-267.

101. Chou, Y.-Y., et al., *Mapping correlations between ventricular expansion and CSF amyloid and tau biomarkers in 240 subjects with Alzheimer's disease, mild cognitive impairment and elderly controls.* NeuroImage, 2009. **46**(2): p. 394-410.

102. Madsen, S.K., et al., *3D maps localize caudate nucleus atrophy in 400 AD, MCI, and healthy elderly subjects.* Neurobiol Aging, 2010. **31**(8): p. 1312-1325.

103. Qiu, A., et al., *Atlas generation for subcortical and ventricular structures with its applications in shape analysis.* IEEE Trans Image Process, 2010. **19**(6): p. 1539-1547.

104. Costafreda, S.G., et al., *Automated hippocampal shape analysis predicts the onset of dementia in mild cognitive impairment.* Neuroimage, 2011. **56**(1): p. 212-219.

105. Wang, L., et al., *Abnormalities of hippocampal surface structure in very mild dementia of the Alzheimer type.* Neuroimage, 2006. **30**(1): p. 52-60.

106. Chou, Y.-Y., et al., *Ventricular maps in 804 ADNI subjects: correlations with CSF biomarkers and clinical decline.* Neurobiol Aging, 2010. **31**(8): p. 1386-1400.

107. Morra, J.H., et al., *Automated 3D mapping of hippocampal atrophy and its clinical correlates in 400 subjects with Alzheimer's disease, mild cognitive impairment, and elderly controls.* Hum Brain Mapp, 2009. **30**(9): p. 2766-2788.

108. Qiu, A., et al., *Parallel transport in diffeomorphisms distinguishes the time-dependent pattern of hippocampal surface deformation due to healthy aging and the dementia of the Alzheimer's type.* NeuroImage, 2008. **40**(1): p. 68-76.

109. Qiu, A., et al., *Regional shape abnormalities in mild cognitive impairment and Alzheimer's disease.* NeuroImage, 2009. **45**(3): p. 656-661.

110. Shi, Y., et al., *Inverse-Consistent Surface Mapping with Laplace-Beltrami Eigen-Features.* Information Processing in Medical Imaging, 2009: p. 467-478.

111. Cho, Y., et al., *A multi-resolution scheme for distortion-minimizing mapping between human subcortical structures based on geodesic construction on Riemannian manifolds.* Neuroimage, 2011. **57**(4): p. 1376-1392.

112. Lui, L.M., et al., *Shape-based diffeomorphic registration on hippocampal surfaces using Beltrami holomorphic flow.* Med Image Comput Comput Assist Interv, 2010. **13**(Pt 2): p. 323-330.

113. Wang, Y., M.-C. Chiang, and P.M. Thompson. *Automated Surface Matching using Mutual Information Applied to Riemann Surface Structures*. in *Med. Image Comp. Comput.-Assist. Intervention, Proceedings, Part II*. 2005.

114. Leow, A., et al., *Inverse consistent mapping in 3D deformable image registration: its construction and statistical properties.* Inf Process Med Imaging, 2005. **19**: p. 493-503.

115. Chiang, M.C., et al., *Fluid registration of diffusion tensor images using information theory.* IEEE Trans Med Imaging, 2008. **27**(4): p. 442-456.

116. Ashburner, J., et al., *Identifying global anatomical differences: deformation-based morphometry.* Human Brain Mapping, 1998. **6**(5-6): p. 348-357.

117. Chung, M.K., et al., *A unified statistical approach to deformation-based morphometry.* Neuroimage, 2001. **14**: p. 595-606.

118. Chung, M.K., et al., *Deformation-based Surface Morphometry Applied to Gray Matter Deformation.* NeuroImage, 2003. **18**: p. 198-213.

119. Wang, L., et al., *Changes in hippocampal volume and shape across time distinguish dementia of the Alzheimer type from healthy aging.* NeuroImage, 2003. **20**(2): p. 667-682.

120. Davatzikos, C., et al., *A computerized approach for morphological analysis of the corpus callosum.* J Comput Assist Tomogr, 1996. **20**(1): p. 88-97.

121. Fox, N.C., et al., *Correlation between rates of brain atrophy and cognitive decline in AD.* Neurology, 1999. **52**(8): p. 1687-1689.

122. Chen, K., et al., *Correlations between apolipoprotein E epsilon4 gene dose and whole brain atrophy rates.* Am J Psychiatry, 2007. **164**(6): p. 916-921.

123. Stonnington, C.M., et al., *Predicting clinical scores from magnetic resonance scans in Alzheimer's disease.* Neuroimage, 2010. **51**(4): p. 1405-1413.

124. Cardenas, V.A., et al., *Brain atrophy associated with baseline and longitudinal measures of cognition.* Neurobiol Aging, 2011. **32**(4): p. 572-580.

125. Hua, X., et al., *Accurate measurement of brain changes in longitudinal MRI scans using tensor-based morphometry.* Neuroimage, 2011. **57**(1): p. 5-14.

126. Han, X., C. Xu, and J.L. Prince, *A topology preserving level set method for geometric deformable models.* IEEE Trans Pattern Anal Mach Intell, 2003. **25**(6): p. 755-768.

127. Lorensen, W.E. and H.E. Cline, *Marching cubes: A high resolution 3D surface construction algorithm.* SIGGRAPH Comput. Graph., 1987. **21**(4): p. 163-169.

128. Hoppe, H., *Progressive meshes*, in *Proceedings of the 23rd annual conference on Computer graphics and interactive techniques*. 1996, ACM. p. 99-108.

129. Loop, C., *Smooth Subdivision Surfaces Based on Triangles*, in *Mathematics Department*. 1987, University of Utah.

130. Guggenheimer, H.W., *Differential Geometry*. 1977: Dover Publications.

131. Wang, Y., et al., *Brain Surface Conformal Parameterization using Riemann Surface Structure.* IEEE Trans Med Imag, 2007. **26**(6): p. 853-865.

132. Lui, L.M., et al., *Computation of Curvatures using Conformal Parameterization.* Communications in Information and Systems, 2008. **8**(1): p. 1-16.

133. Gu, X. and B. Vemuri. *Matching 3D shapes using 2D conformal representations*. in *Med Image Comput Comput Assist Interv*. 2004. Springer.

134. D'Agostino, E., et al., *A viscous fluid model for multimodal non-rigid image registration using mutual information.* Med Image Anal, 2003. **7**(4): p. 565-575.

135. Hermosillo, G., et al., *Variational methods for multimodal image matching*. International Journal of Computer Vision, 2002. 50(3): p. 329-343.

136. Kim, B., et al., *Mutual information for automated unwarping of rat brain autoradiographs.* NeuroImage, 1997. **5**(1): p. 31-40.

137. West, J., et al., *Comparison and evaluation of retrospective intermodality brain image registration techniques.* J Comput Assist Tomogr, 1997. **21**(4): p. 554-566.

138. Meyer, C.R., et al., *Demonstration of accuracy and clinical versatility of mutual information for automatic multimodality image fusion using affine and thin-plate spline warped geometric deformations.* Med Image Anal, 1997. **1**(3): p. 195-206.

139. Rueckert, D., et al., *Nonrigid registration using free-form deformations: application to breast MR images.* IEEE Trans Med Imaging, 1999. **18**(8): p. 712-721.

140. Lui, L.M., Y. Wang, and T.F. Chan, *Solving PDEs on Manifolds with Global Conformal Parametriazation,* in *Variational, Geometric, and Level Set Methods in Computer Vision*. 2005. p. 307-319.

141. Stam, J., *Flows on surfaces of arbitrary topology*, in *ACM Transactions on Graphics*. 2003. p. 724-731.

142. Aris, R., *Vectors, Tensors and the Basic Equations of Fluid Mechanics*. 1989: Dover, New York.

143. Lui, L.M., et al., *Variational Method on Riemann Surfaces using Conformal Parameterization and its Applications to Image Processing.* Methods Appl. Anal., 2008. **15**(4): p. 513-538.

144. Christensen, G.E., *Deformable Shape Models For Anatomy*. 1994, Washington University.

145. Rey, D., et al., *Automatic detection and segmentation of evolving processes in 3D medical images: Application to multiple sclerosis.* Med Image Anal, 2002. **6**(2): p. 163-179.

146. Christensen, G.E. and H.J. Johnson, *Consistent image registration.* IEEE Trans Med Imaging, 2001. **20**(7): p. 568-582.

147. Reuter, M. and B. Fischl, *Avoiding asymmetry-induced bias in longitudinal image processing.* Neuroimage, 2011. **57**(1): p. 19-21.

148. Reuter, M., H.D. Rosas, and B. Fischl, *Highly accurate inverse consistent registration: a robust approach.* Neuroimage, 2010. **53**(4): p. 1181-1196.

149. Hsiung, C.-C., *A First Course in Differential Geometry*. 1997: International Press.

150. Arsigny, V., et al., *Log-Euclidean Metrics for Fast and Simple Calculus on Diffusion Tensors.* Magn. Reson. Med., 2006. **56**(2): p. 411-421.

151. Hotelling, H., *The generalization of Student's ratio.* Ann. Math. Statist., 1931. **2**: p. 360-378.

152. Cao, J. and K.J. Worsley, *The detection of local shape changes via the geometry of Hotelling's* T^2 *fields.* Ann. Statist, 1999. **27**(3): p. 925-942.

153. Thirion, J.P., et al., *Statistical analysis of normal and abnormal dissymmetry in volumetric medical images.* Med Image Anal, 2000. **4**(2): p. 111-121.

154. Kim, W.H., et al., *Wavelet based multi-scale shape features on arbitrary surfaces for cortical thickness discrimination* Advances in Neural Information Processing Systems (NIPS), 2012: p. 1250-1258.

155. Zhang, D. and G. Lu, *Review of shape representation and description techniques.* Pattern Recognition, 2004. **37**(1): p. 1-19.

156. Elad, M., P. Milanfar, and G.H. Golub, *Shape from moments - an estimation theory perspective.* Trans. Sig. Proc., 2004. **52**(7): p. 1814-1829.

157. Folstein, M.F., S.E. Folstein, and P.R. McHugh, *"Mini-mental state". A practical method for grading the cognitive state of patients for the clinician.* J Psychiatr Res, 1975. **12**(3): p. 189-198.

158. Berg, L., *Clinical Dementia Rating (CDR).* Psychopharmacol Bull, 1988. **24**(4): p. 637-639.

159. Wechsler, D., *Wechsler Memory Scale-Revised Manual*. 1987, San Antonio, TX: Psychological Corporation.

160. Benjamini, Y. and Y. Hochberg, *Controlling the False Discovery Rate: A Practical and Powerful Approach to Multiple Testing.* Journal of the Royal Statistical Society. Series B (Methodological), 1995. **57**(1): p. 289-300.

161. Styner, M., et al., *Framework for the Statistical Shape Analysis of Brain Structures using SPHARM-PDM.* Insight Journal, 2006. (1071): p. 242-250.

162. Patenaude, B., et al., *A Bayesian model of shape and appearance for subcortical brain segmentation.* Neuroimage, 2011. **56**(3): p. 907-922.

163. Patenaude, B., *Bayesian Statistical Models of Shape and Appearance for Subcortical Brain Segmentation*. 2007, University of Oxford.

164. Carmichael, D., *Hippocampal Volume and Morphometry in a Cognitively Impaired Population at Increased Risk of Schizophrenia: The Edinburgh Study of Comorbidity*. 2011, The University of Edinburgh.

165. Tae, W.S., et al., *Hippocampal shape deformation in female patients with unremitting major depressive disorder.* AJNR Am J Neuroradiol, 2011. **32**(4): p. 671-676.

166. Alhadidi, A., et al., *3D quantification of mandibular asymmetry using the SPHARM-PDM tool box.* Int J Comput Assist Radiol Surg, 2012. **7**(2): p. 265-271.

167. Paniagua, B., et al. *Combined SPHARM-PDM and entropy-based particle systems shape analysis framework*. in *SPIE Conference 8317 Progress in Biomedical Optics and Imaging*. 2012.

168. Paniagua, B., et al., *Lateral ventricle morphology analysis via mean latitude axis.* Proc Soc Photo Opt Instrum Eng, 2013. **8672**.

169. Duvernoy, H.M., *The Human Hippocampus. An Atlas of Applied Anatomy*. 1988, Munich: J. F. Bergmann Verlag.

170. Poirier, J., et al., *Apolipoprotein E polymorphism and Alzheimer's disease.* Lancet, 1993. **342**(8873): p. 697-699.

171. Strittmatter, W.J., et al., *Apolipoprotein E: high-avidity binding to beta-amyloid and increased frequency of type 4 allele in late-onset familial Alzheimer disease.* Proc Natl Acad Sci U S A, 1993. **90**(5): p. 1977-1981.

172. Corder, E.H., et al., *Gene dose of apolipoprotein E type 4 allele and the risk of Alzheimer's disease in late onset families.* Science, 1993. **261**(5123): p. 921-923.

173. Blacker, D., et al., *ApoE-4 and age at onset of Alzheimer's disease: the NIMH genetics initiative.* Neurology, 1997. **48**(1): p. 139-147.

174. Meyer, M.R., et al., *APOE genotype predicts when--not whether--one is predisposed to develop Alzheimer disease.* Nat Genet, 1998. **19**(4): p. 321-322.

175. Agosta, F., et al., *Apolipoprotein E epsilon4 is associated with disease-specific effects on brain atrophy in Alzheimer's disease and frontotemporal dementia.* Proc Natl Acad Sci U S A, 2009. **106**(6): p. 2018-2022.

176. Geroldi, C., et al., *APOE-epsilon4 is associated with less frontal and more medial temporal lobe atrophy in AD.* Neurology, 1999. **53**(8): p. 1825-1832.

177. Hashimoto, M., et al., *Apolipoprotein E epsilon 4 and the pattern of regional brain atrophy in Alzheimer's disease.* Neurology, 2001. **57**(8): p. 1461-1466.

178. Lehtovirta, M., et al., *Volumes of hippocampus, amygdala and frontal lobe in Alzheimer patients with different apolipoprotein E genotypes.* Neuroscience, 1995. **67**(1): p. 65-72.

179. Mueller, S.G. and M.W. Weiner, *Selective effect of age, Apo e4, and Alzheimer's disease on hippocampal subfields.* Hippocampus, 2009. **19**(6): p. 558-564.

180. Qiu, A., et al., *APOE related hippocampal shape alteration in geriatric depression.* NeuroImage, 2009. **44**(3): p. 620-626.

181. Pievani, M., et al., *APOE4 is associated with greater atrophy of the hippocampal formation in Alzheimer's disease.* Neuroimage, 2011. **55**(3): p. 909-919.

182. Caselli, R.J., et al., *Longitudinal modeling of age-related memory decline and the APOE epsilon4 effect.* N Engl J Med, 2009. **361**(3): p. 255-263.

183. Caselli, R.J., et al., *Cerebrovascular risk factors and preclinical memory decline in healthy APOE epsilon4 homozygotes.* Neurology, 2011. **76**(12): p. 1078-1084.

184. Pizer, S., et al., *Segmentation, registration, and measurement of shape variation via image object shape.* IEEE Trans. Med. Imag., 1999. **18**: p. 851-865.

185. Bansal, R., et al., *Integrated segmentation, registration and visualization of multimodal medical image datasets*, in *IEEE Visualization*. 2000.

186. Gerig, G., et al., *Shape analysis of brain ventricles using SPHARM*, in *IEEE Workshop on Mathematical Methods in Biomedical Image Analysis (MMBIA'01)*. 2001.

187. Wang, Y. *Multivariate Surface-based Subcortical Structure Morphometry System*. 2011; Available from: http://gsl.lab.asu.edu/conformal.htm.

188. Dickson, D.W., et al., *Identification of normal and pathological aging in prospectively studied nondemented elderly humans.* Neurobiol Aging, 1992. **13**(1): p. 179-189.

189. Gouras, G.K., et al., *Increased apolipoprotein E epsilon 4 in epilepsy with senile plaques.* Ann Neurol, 1997. **41**(3): p. 402-404.

190. Bennett, D.A., et al., *Neuropathologic intermediate phenotypes enhance association to Alzheimer susceptibility alleles.* Neurology, 2009. **72**(17): p. 1495-1503.

191. Kok, E., et al., *Apolipoprotein E-dependent accumulation of Alzheimer disease-related lesions begins in middle age.* Ann Neurol, 2009. **65**(6): p. 650-657.

192. Caselli, R.J., et al., *Amyloid load in nondemented brains correlates with APOE e4.* Neurosci Lett, 2010. **473**(3): p. 168-171.

193. Reiman, E.M., et al., *Preclinical evidence of Alzheimer's disease in persons homozygous for the epsilon 4 allele for apolipoprotein E.* N Engl J Med, 1996. **334**(12): p. 752-758.

194. Reiman, E.M., et al., *Correlations between apolipoprotein E epsilon4 gene dose and brain-imaging measurements of regional hypometabolism.* Proc Natl Acad Sci U S A, 2005. **102**(23): p. 8299-8302.

195. Reiman, E.M., et al., *Fibrillar amyloid-beta burden in cognitively normal people at 3 levels of genetic risk for Alzheimer's disease.* Proc Natl Acad Sci U S A, 2009. **106**(16): p. 6820-6825.

196. Torgerson, W., *Multidimensional scaling: I. Theory and method.* Psychometrika, 1952. **17**(4): p. 401-419.

197. Shepard, R., *The analysis of proximities: Multidimensional scaling with an unknown distance function. II.* Psychometrika, 1962. **27**(3): p. 219-246.

198. Kruskal, J., *Nonmetric multidimensional scaling: A numerical method.* Psychometrika, 1964. **29**(2): p. 115-129.

199. Kruskal, J., *Multidimensional scaling by optimizing goodness of fit to a nonmetric hypothesis.* Psychometrika, 1964. **29**(1): p. 1-27.

200. Lipman, Y. and T. Funkhouser, *Möbius voting for surface correspondence*, in *ACM SIGGRAPH 2009 papers*. 2009, ACM: New Orleans, Louisiana. p. 1-12.

201. Boyer, D.M., et al., *Algorithms to automatically quantify the geometric similarity of anatomical surfaces.* Proc Natl Acad Sci U S A, 2011. **108**(45): p. 18221-18226.

202. Timsari, B. and R.M. Leahy, *Optimization method for creating semi-isometric flat maps of the cerebral cortex*. Medical Imaging 2000: Image Processing, 2000. **3979**(1): p. 698-708.

203. Sander, P.V., et al. *Texture mapping progressive meshes*. in *Proceedings of the 28th annual conference on Computer graphics and interactive techniques*. 2001. ACM.

204. Zigelman, G., R. Kimmel, and N. Kiryati, *Texture mapping using surface flattening via multidimensional scaling.* Visualization and Computer Graphics, IEEE Transactions on, 2002. **8**(2): p. 198-207.

205. Balasubramanian, M., J.R. Polimeni, and E.L. Schwartz, *Near-isometric flattening of brain surfaces.* Neuroimage, 2010. **51**(2): p. 694-703.

206. Schreiner, J., et al. *Inter-surface mapping*. in *ACM SIGGRAPH 2004 Papers*. 2004. Los Angeles, California: ACM.

207. Eckstein, I., et al., *Generalized surface flows for deformable registration and cortical matching.* Med Image Comput Comput Assist Interv, 2007. **10**(Pt 1): p. 692-700.

208. Shen, L. and F. Makedon, *Spherical mapping for processing of 3D closed surfaces.* Image and Vision Computing, 2006. **24**(7): p. 743-761.

209. Morra, J.H., et al., *Comparison of AdaBoost and Support Vector Machines for Detecting Alzheimer's Disease Through Automated Hippocampal Segmentation.* Medical Imaging, IEEE Transactions on, 2010. **29**(1): p. 30-43.

210. Shattuck, D.W. and R.M. Leahy, *BrainSuite: an automated cortical surface identification tool.* Med Image Anal, 2002. **6**(2): p. 129-142.

211. Yushkevich, P.A., et al., *User-guided 3D active contour segmentation of anatomical structures: significantly improved efficiency and reliability.* Neuroimage, 2006. **31**(3): p. 1116-1128.

212. Bossa, M., E. Zacur, and S. Olmos, *Statistical analysis of relative pose information of subcortical nuclei: application on ADNI data.* Neuroimage, 2011. **55**(3): p. 999-1008.

213. Yushkevich, P.A., H. Zhang, and J.C. Gee, *Continuous medial representation for anatomical structures.* IEEE Trans Med Imaging, 2006. **25**(12): p. 1547-1564.

214. Brodmann, K., *Vergleichende Lokalisationslehre der Grosshirnrinde in ihren Prinzipien dargestellt auf Grund des Zellenbaues*. 1909: Johann Ambrosius Barth Verlag.

215. Chung, M.K., *Computational Neuroanatomy: The Methods*. 2012: World Scientific Publishing Company.

216. Hasboun, D., et al., *MR determination of hippocampal volume: comparison of three methods.* AJNR Am J Neuroradiol, 1996. **17**(6): p. 1091-1098.

217. Ystad, M.A., et al., *Hippocampal volumes are important predictors for memory function in elderly women.* BMC Med Imaging, 2009. **9**: p. 17.

218. Hickie, I., et al., *Reduced hippocampal volumes and memory loss in patients with early- and late-onset depression.* Br J Psychiatry, 2005. **186**: p. 197-202.

219. Taubin, G. *A signal processing approach to fair surface design*. in *SIGGRAPH '95 Proceedings*. 1995.

220. Desbrun, M., et al. *Implicit fairing of irregular meshes using diffusion and curvature flow*. in *SIGGRAPH '99 Proceedings*. 1999.

221. Ohtake, Y., A.G. Belyaev, and I.A. Bogaevski. *Polyhedral Surface Smoothing with Simultaneous Mesh Regularization*. in *Geometric Modeling and Processing*. 2000.

222. Desbrun, M., et al. *Anisotropic Feature-Preserving Denoising of Height Fields and Bivariate Data*. in *Graphics Interface*. 2000.

223. Clarenz, U., U. Diewald, and M. Rumpf. *Anisotropic Geometric Diffusion in Surface Processing*. in *IEEE Visualization 2000*. 2000.

224. Zhang, H. and E. Fiume. *Mesh Smoothing with Shape or Feature Preservation*. in *Advances in Modeling, Animation, and Rendering*. 2002.

225. Meyer, M., et al. *Discrete Differential-Geometry Operators for Triangulated 2-Manifolds*. in *Proceedings of Visualization and Mathematics*. 2003.

226. Bajaj, C.L. and G. Xu, *Anisotropic diffusion of surfaces and functions on surfaces.* ACM Transactions on Graphics, 2003. **22**(1): p. 4-32.

227. Jones, T.R., F. Durand, and M. Desbrun, *Non-iterative, feature-preserving mesh smoothing.* ACM Transactions on Graphics, 2003. **22**(3): p. 943-949.

228. Fleishman, S., I. Drori, and D. Cohen-Or, *Bilateral mesh denoising.* ACM Transactions on Graphics, 2003. **22**(3): p. 950-953.

229. Sun, X., et al., *Fast and Effective Feature-Preserving Mesh Denoising* IEEE Transactions on Visualization and Computer Graphics, 2007. **13**(5): p. 925-938.

230. Sun, X., et al., *Random walks for feature-preserving mesh denoising.* Computer Aided Geometric Design, 2008. **25**(7): p. 437-456.

231. Li, Z., et al., *A new feature-preserving mesh-smoothing algorithm.* The Visual Computer, 2009. **25**(2): p. 139-148.

232. Worsley, K.J., et al., *Unified univariate and multivariate random field theory.* Neuroimage, 2004. **23 Suppl 1**: p. S189-195.

233. Taylor, J.E. and K.J. Worsley, *Random fields of multivariate test statistics, with applications to shape analysis.* Annals of Statistics, 2008. **36**: p. 1-27.

234. Roy, S.N., *On a Heuristic Method of Test Construction and its use in Multivariate Analysis.* The Annals of Mathematical Statistics, 1953. **24**(2): p. 220-238.

235. Chung, M.K., et al., *General multivariate linear modeling of surface shapes using SurfStat.* Neuroimage, 2010. **53**(2): p. 491-505.

236. Wang, Y., et al. *Surface Multivariate Tensor-based Morphometry on Premature Neonates: A Pilot Study*. in *Image Analysis of Human Brain Development (IAHBD)*. 2011. Toronto, Canada.

237. Winkler, A.M., et al., *Cortical thickness or grey matter volume? The importance of selecting the phenotype for imaging genetics studies.* NeuroImage, 2010. **53**(3): p. 1135-1146.

238. Winkler, A.M., et al., *Measuring and comparing brain cortical surface area and other areal quantities.* Neuroimage, 2012. **61**(4): p. 1428-1443.

239. Goebel, R., *BrainVoyager--past, present, future.* Neuroimage, 2012. **62**(2): p. 748-756.

240. Apostolova, L.G., et al., *Automated 3D mapping of baseline and 12-month associations between three verbal memory measures and hippocampal atrophy in 490 ADNI subjects.* Neuroimage, 2010. **51**(1): p. 488-499.

241. Van Leemput, K., et al., *Automated segmentation of hippocampal subfields from ultra-high resolution in vivo MRI.* Hippocampus, 2009. **19**(6): p. 549-557.

242. Yassa, M.A., et al., *High-resolution structural and functional MRI of hippocampal CA3 and dentate gyrus in patients with amnestic Mild Cognitive Impairment.* Neuroimage, 2010. **51**(3): p. 1242-1252.

243. Yushkevich, P.A., et al., *Nearly automatic segmentation of hippocampal subfields in in vivo focal T2-weighted MRI.* Neuroimage, 2010. **53**(4): p. 1208-1224.

244. Du, J., L. Younes, and A. Qiu, *Whole brain diffeomorphic metric mapping via integration of sulcal and gyral curves, cortical surfaces, and images.* Neuroimage, 2011. **56**(1): p. 162-173.

245. Shi, J., et al., *Surface Fluid Registration and Multivariate Tensor-based Morphometry in NewBorns – the Effects of Prematurity on the Putamen*, in *Asia-Pacific Signal and Information Processing Association Annual Summit and Conference (APSIPA ASC)*. 2012: Hollywood, CA, USA.

246. Wang, Y., et al., *3D vs. 2D Surface Shape Analysis of the Corpus Collosum in Premature Neonates*, in *MICCAI: Workshop on Paediatric and Perinatal Imaging*. 2012: Nice, France.

247. Gutman, B.A., et al., *Maximizing power to track Alzheimer's disease and MCI progression by LDA-based weighting of longitudinal ventricular surface features.* Neuroimage, 2013. **70**: p. 386-401.

248. Yuan, L., et al., *Multi-source feature learning for joint analysis of incomplete multiple heterogeneous neuroimaging data.* Neuroimage, 2012. **61**(3): p. 622-632.

249. Ye, J., et al., *Sparse learning and stability selection for predicting MCI to AD conversion using baseline ADNI data.* BMC Neurol, 2012. **12**(1): p. 46.

250. Ho, A.J., et al., *A commonly carried allele of the obesity-related FTO gene is associated with reduced brain volume in the healthy elderly.* Proc Natl Acad Sci U S A, 2010. **107**(18): p. 8404-8409.

251. Sun, D., et al., *Elucidating a Magnetic Resonance Imaging-Based Neuroanatomic Biomarker for Psychosis: Classification Analysis Using Probabilistic Brain Atlas and Machine Learning Algorithms.* Biological Psychiatry, 2009. **66**(11): p. 1055-1060.

252. Kohannim, O., et al., *Boosting power for clinical trials using classifiers based on multiple biomarkers.* Neurobiol Aging, 2010. **31**(8): p. 1429-1442.

253. Wang, Y., et al. *MRI-based Biomarker Detection using Conformal Slit Maps and Machine Learning*. in *The 16th Annual Meeting of the Organization for Human Brain Mapping*. 2010. Barcelona, Spain.

254. Vapnik, V., *Statistical Learning Theory*. 1998: New York: Wiley-Interscience.

255. Candès, E.J. and T. Tao, *Decoding by linear programming.* Information Theory, IEEE Transactions on, 2005. **51**(12): p. 4203-4215.

256. Lewis, M.M., et al., *Asymmetrical lateral ventricular enlargement in Parkinson's disease.* Eur J Neurol, 2009. **16**(4): p. 475-481.

257. Kempton, M.J., et al., *Progressive lateral ventricular enlargement in schizophrenia: A meta-analysis of longitudinal MRI studies.* Schizophrenia Research, 2010. **120**(1-3): p. 54-62.

258. Chou, Y.-Y., et al., *Mapping genetic influences on ventricular structure in twins.* NeuroImage, 2009. **44**(4): p. 1312-1323.

259. Kremen, W.S., et al., *Heritability of brain ventricle volume: converging evidence from inconsistent results.* Neurobiol Aging, 2012. **33**(1): p. 1-8.

260. Luo, F., X. Gu, and J. Dai, *Variational principles on discrete Surfaces*. Advanced Lectures in Mathematics. 2008: International Press.

261. Tsui, A., et al., *Globally optimal cortical surface matching with exact landmark correspondence*, in *Proceedings of the 23rd international conference on Information Processing in Medical Imaging*. 2013, Springer-Verlag: Asilomar, CA. p. 487-498.

262. Wang, Y., et al., *Brain Surface Conformal Parameterization with Algebraic Functions.* Med Image Comput Comput Assist Interv Proceedings, Part II, 2006: p. 946-954.

263. Jin, M., et al., *Discrete surface Ricci flow.* IEEE Trans Vis Comput Graph, 2008. **14**(5): p. 1030-1043.

264. Leow, A.D., et al., *Alzheimer's disease neuroimaging initiative: a one-year follow up study using tensor-based morphometry correlating degenerative rates, biomarkers and cognition.* Neuroimage, 2009. **45**(3): p. 645-655.

265. Shi, J., et al., *A multivariate surface-based analysis of the putamen in premature newborns: regional differences within the ventral striatum.* PLoS One, 2013. **8**(7): p. e66736.

266. Shi, J., et al., *Surface fluid registration of conformal representation: application to detect disease effect and genetic influence on hippocampus.* NeuroImage, 2013. **78**: p. 111-134.

267. Shi, J., et al., *Genetic influence of apolipoprotein E4 genotype on hippocampal morphometry: An N = 725 surface-based Alzheimer's disease neuroimaging initiative study*. Hum Brain Mapp, 2014.

268. Caselli, R.J. and E.M. Reiman, *Characterizing the preclinical stages of Alzheimer's disease and the prospect of presymptomatic intervention.* J Alzheimers Dis, 2013. **33**(Suppl 1): p. S405-416.

269. Langbaum, J.B., et al., *Ushering in the study and treatment of preclinical Alzheimer disease.* Nat Rev Neurol, 2013. **9**(7): p. 371-381.

270. Wolf, H., et al., *A critical discussion of the role of neuroimaging in mild cognitive impairment.* Acta Neurol Scand Suppl, 2003. **179**: p. 52-76.

271. Small, G.W., et al., *PET of brain amyloid and tau in mild cognitive impairment.* N Engl J Med, 2006. **355**(25): p. 2652-2663.

272. Matsuda, H., *The role of neuroimaging in mild cognitive impairment.* Neuropathology, 2007. **27**(6): p. 570-577.

273. Pihlajamaki, M., A.M. Jauhiainen, and H. Soininen, *Structural and functional MRI in mild cognitive impairment.* Curr Alzheimer Res, 2009. **6**(2): p. 179-185.

274. Petersen, R.C. and C.R. Jack, Jr., *Imaging and biomarkers in early Alzheimer's disease and mild cognitive impairment.* Clin Pharmacol Ther, 2009. **86**(4): p. 438-441.

275. Petersen, R.C., *Clinical practice. Mild cognitive impairment.* N Engl J Med, 2011. **364**(23): p. 2227-2234.

276. Caroli, A., et al., *Summary metrics to assess Alzheimer disease-related hypometabolic pattern with 18F-FDG PET: head-to-head comparison.* J Nucl Med, 2012. **53**(4): p. 592-600.

277. Chung, M.K., et al., *Cortical thickness analysis in autism with heat kernel smoothing.* NeuroImage, 2005. **25**(4): p. 1256-1265.

278. Collins, D.L., et al., *Automatic 3D intersubject registration of MR volumetric data in standardized Talairach space.* J Comput Assist Tomogr, 1994. **18**(2): p. 192-205.

279. Hamilton, R.S., *The Ricci flow on surfaces.* Contemp. Math., 1988. **71**: p. 237-262.

280. Thurston, W.P., *Geometry and Topology of Three-Manifolds*. 1976: Princeton lecture notes.

281. Hurdal, M.K. and K. Stephenson, *Discrete conformal methods for cortical brain flattening.* Neuroimage, 2009. **45**(1 Suppl): p. S86-98.

282. Stephenson, K., *Introduction to Circle Packing: The Theory of Discrete Analytic Functions*. 2005: Cambridge University Press.

283. Wang, Y., et al., *Multivariate Tensor-based Morphometry on Surfaces: Application to Mapping Ventricular Changes in HIV/AIDS*, in *IEEE International Symposium on Biomedical Imaging: From Nano to Macro, 2009 (ISBI 2009)*. 2009.

284. Fischl, B., et al., *High-resolution intersubject averaging and a coordinate system for the cortical surface.* Hum Brain Mapp, 1999. **8**(4): p. 272-284.

285. Joshi, A.A., et al., *Surface-Constrained Volumetric Brain Registration Using Harmonic Mappings.* IEEE Trans Med Imag, 2007. **26**(12): p. 1657-1669.

286. Auzias, G., et al., *Model-driven harmonic parameterization of the cortical surface: HIP-HOP.* IEEE Trans Med Imaging, 2013. **32**(5): p. 873-887.

287. Chung, M.K., et al., *Tensor-based Brain Surface Modeling and Analysis*, in *IEEE Conference on Computer Vision and Pattern Recognition*. 2003. p. 467-473.

288. Nichols, T.E. and A.P. Holmes, *Nonparametric permutation tests for functional neuroimaging: a primer with examples.* Hum Brain Mapp, 2002. **15**(1): p. 1-25.

289. Thompson, P.M., et al., *Dynamics of Gray Matter Loss in Alzheimer's Disease.* J. Neuroscience, 2003. **23**: p. 994-1005.

290. Rosen, W.G., R.C. Mohs, and K.L. Davis, *A new rating scale for Alzheimer's disease.* Am J Psychiatry, 1984. **141**(11): p. 1356-1364.

291. Rey, A., *L'examen clinique en psychologie*. 1964: Presses Universitaires de France, Paris.

292. Whitwell, J.L., et al., *MRI correlates of neurofibrillary tangle pathology at autopsy: a voxel-based morphometry study.* Neurology, 2008. **71**(10): p. 743-749.

293. Henneman, W.J., et al., *Baseline CSF p-tau levels independently predict progression of hippocampal atrophy in Alzheimer disease.* Neurology, 2009. **73**(12): p. 935-940.

294. Vemuri, P., et al., *Serial MRI and CSF biomarkers in normal aging, MCI, and AD.* Neurology, 2010. **75**(2): p. 143-151.

295. Reiman, E.M. and W.J. Jagust, *Brain imaging in the study of Alzheimer's disease.* Neuroimage, 2012. **61**(2): p. 505-516.

296. Toledo, J.B., et al., *Clinical and multimodal biomarker correlates of ADNI neuropathological findings.* Acta Neuropathol Commun, 2013. **1**(1): p. 65.

297. Chen, K., et al., *Correlations between FDG PET glucose uptake-MRI gray matter volume scores and apolipoprotein E epsilon4 gene dose in cognitively normal adults: A cross-validation study using voxel-based multi-modal partial least squares.* Neuroimage, 2012. **60**(4): p. 2316-2322.

298. Schraml, F., et al., *Association between an Alzheimer's Disease-Related Index and Gene Dose.* PLoS One, 2013. **8**(6): p. e67163.

299. Jeong, H.S., et al., *Morphometric abnormalities of the lateral ventricles in methamphetamine-dependent subjects.* Drug Alcohol Depend, 2013. **131**(3): p. 222-229.

300. Lee, J.H., et al., *Morphometric changes in lateral ventricles of patients with recent-onset type 2 diabetes mellitus.* PLoS One, 2013. **8**(4): p. e60515.

301. Chen, K., et al. *Baseline FDG PET and volumetric MRI predicts Alzheimer's disease conversion from mild cognitive impairment: An ADNI study*. in *Alzheimer's Association International Conference*. 2013. Boston.

302. Braak, H., et al., *Staging of Alzheimer disease-associated neurofibrillary pathology using paraffin sections and immunocytochemistry.* Acta Neuropathol, 2006. **112**(4): p. 389-404.

303. Weiner, M.W., et al., *The Alzheimer's Disease Neuroimaging Initiative: a review of papers published since its inception.* Alzheimers Dement, 2012. **8**(1 Suppl): p. S1-68.

304. Westman, E., et al., *Regional magnetic resonance imaging measures for multivariate analysis in Alzheimer's disease and mild cognitive impairment.* Brain Topogr, 2013. **26**(1): p. 9-23.

305. Li, Y., et al., *Discriminant analysis of longitudinal cortical thickness changes in Alzheimer's disease using dynamic and network features.* Neurobiol Aging, 2012. **33**(2): p. 427 e15-30.

306. Jack, C.R., Jr., et al., *Serial PIB and MRI in normal, mild cognitive impairment and Alzheimer's disease: implications for sequence of pathological events in Alzheimer's disease.* Brain, 2009. **132**(Pt 5): p. 1355-1365.

307. Samtani, M.N., et al., *An improved model for disease progression in patients from the Alzheimer's disease neuroimaging initiative.* J Clin Pharmacol, 2012. **52**(5): p. 629-644.

308. Buckner, R.L., J.R. Andrews-Hanna, and D.L. Schacter, *The brain's default network: anatomy, function, and relevance to disease.* Ann N Y Acad Sci, 2008. **1124**: p. 1-38.

309. Leech, R. and D.J. Sharp, *The role of the posterior cingulate cortex in cognition and disease.* Brain, 2014. **137**(Pt 1): p. 12-32.

310. Matsuda, H., *Role of neuroimaging in Alzheimer's disease, with emphasis on brain perfusion SPECT.* J Nucl Med, 2007. **48**(8): p. 1289-1300.

311. Sowell, E.R., et al., *Mapping sulcal pattern asymmetry and local cortical surface gray matter distribution in vivo: maturation in perisylvian cortices.* Cereb Cortex, 2002. **12**(1): p. 17-26.

312. Wang, Y., et al., *Brain Surface Conformal Parameterization with Holomorphic Flow Method and Its Application to HIV/AIDS.* NeuroImage, 2009. **47**(Suppl 1): p. 99.

313. Ashburner, J. and K.J. Friston, *Voxel-based morphometry--the methods.* Neuroimage, 2000. **11**(6 Pt 1): p. 805-821.

314. Good, C.D., et al., *Cerebral asymmetry and the effects of sex and handedness on brain structure: a voxel-based morphometric analysis of 465 normal adult human brains.* NeuroImage, 2001. **14**(3): p. 685-700.

315. Whitwell, J.L., *Voxel-based morphometry: an automated technique for assessing structural changes in the brain.* The Journal of Neuroscience, 2009. **29**(31): p. 9661-9664.

316. Mechelli, A., et al., *Voxel-based Morphometry of the Human Brain: Methods and Applications.* Current Medical Imaging Reviews, 2005. **1**(2): p. 105.

317. Niedtfeld I, I., et al., *Voxel-Based Morphometry in Women with Borderline Personality Disorder with and without Comorbid Posttraumatic Stress Disorder.* PLoS ONE, 2013. **8**(6): p. e65824.

318. Killgore, W.D.S., et al., *Voxel-based morphometric gray matter correlates of daytime sleepiness.* Neuroscience Letters, 2012. **518**(1): p. 10-13.

319. Joshi, S.H., et al., *Brain pattern analysis of cortical valued distributions*, in *IEEE International Symposium on Biomedical Imaging: from nano to macro*. 2011. p. 1117-1120.

320. Li, K., et al., *Gyral folding pattern analysis via surface profiling.* NeuroImage, 2010. **52**(4): p. 1202-1214.

321. Liu, S., et al., *Multi-Channel neurodegenerative pattern analysis and its application in Alzheimer's disease characterization.* Computerized Medical Imaging and Graphics, 2014. **38**(6): p. 436-444.

322. Han, X., et al., *Reliability of MRI-derived measurements of human cerebral cortical thickness: The effects of field strength, scanner upgrade and manufacturer.* NeuroImage, 2006. **32**: p. 180-194.

323. Chung, M.K., S. Robbins, and A.C. Evans, *Unified Statistical Approach to Cortical Thickness Analysis*, in *Information Processing in Medical Imaging (IPMI)*. 2005. p. 627-638.

324. Seo, S., M.K. Chung, and H.K. Vorperian, *Heat kernel smoothing using Laplace-Beltrami eigenfunctions*, in *13th International Conference on Medical Image Computing and Computer Assisted Intervention (MICCAI)*. 2010. p. 505-512.

325. Lao, Y., et al., *Statistical Analysis of Relative Pose of the Thalamus in Preterm Neonates*, in *MICCAI workshop on CLinical Imagebased Procedures (CLIP 2013): Translational Research in Medical Imaging*. 2013. p. 1-9.

326. Lao, Y., et al., *3D pre- versus post-season comparisons of surface and relative pose of the corpus callosum in contact sport athletes*, in *SPIE, Medical Imaging*. 2014.

327. Carmichael, O.T., et al., *Ventricular volume and dementia progression in the Cardiovascular Health Study.* Neurobiol Aging, 2007. **28**(3): p. 389-397.

328. Ferrarini, L., et al., *Shape differences of the brain ventricles in Alzheimer's disease.* NeuroImage, 2006. **32**(3): p. 1060-1069.

329. Ferrarini, L., et al., *MMSE scores correlate with local ventricular enlargement in the spectrum from cognitively normal to Alzheimer disease.* NeuroImage, 2008. **39**(4): p. 1832-1838.

330. Thompson, P.M., et al., *3D Mapping of Ventricular and Corpus Callosum Abnormalities in HIV/AIDS.* NeuroImage, 2006. **31**(1): p. 12-23.

331. Bader, C., et al., *Estimation of the lateral ventricles volumes from a 2D image and its relationship with cerebrospinal fluid flow.* Biomed Res Int, 2013. **2013**: p. 215989.

332. Wang, G., et al. *A Heat Kernel Based Cortical Thickness Estimation Algorithm*. in *Multimodal Brain Image Analysis*. 2013. Springer International Publishing.

333. Wang, G., et al., *A Novel Cortical Thickness Estimation Method based on Volumetric Laplace-Beltrami Operator and Heat Kernel.* Medical Image Analysis, 2015. **22**(1): p. 1-20.

334. Braskie, M.N. and P.M. Thompson, *A Focus on Structural Brain Imaging in the Alzheimer's Disease Neuroimaging Initiative.* Biol Psychiatry, 2014. **75**(7): p. 527-533.

335. Younes, L., *Spaces and manifolds of shapes in computer vision: An overview.* Image and Vision Computing, 2012. **30**(6-7): p. 389-397.

336. Fletcher, P.T., *Geodesic Regression and the Theory of Least Squares on Riemannian Manifolds.* International Journal of Computer Vision, 2013. **105**(2): p. 171-185.

337. Fletcher, P.T., S. Venkatasubramanian, and S. Joshi, *The geometric median on Riemannian manifolds with application to robust atlas estimation.* Neuroimage, 2009. **45**(1 Suppl): p. S143-152.

338. Kurtek, S., et al., *Parameterization-invariant shape comparisons of anatomical surfaces.* IEEE Trans Med Imaging, 2011. **30**(3): p. 849-858.

339. Gutman, B.A., et al., *A Riemannian Framework for Intrinsic Comparison of Closed Genus-Zero Shapes.* Inf Process Med Imaging, 2015. **24**: p. 205-218.

340. Su, Z., et al., *Optimal mass transport for shape matching and comparison.* IEEE Trans Pattern Anal Mach Intell, 2015. **37**(11): p. 2246-2259.

341. Younes, L., e. Arrate, and M.I. Miller, *Evolutions Equations in Computational Anatomy.* Neuroimage, 2009. **45**(1 Suppl): p. S40-S50.

342. Hong, B.-W. and S. Soatto, *Shape Matching Using Multiscale Integral Invariants.* IEEE Transactions on Pattern Analysis and Machine Intelligence, 2015. **37**(1): p. 151-160.

343. Shi, J., et al., *Studying ventricular abnormalities in mild cognitive impairment with hyperbolic Ricci flow and tensor-based morphometry.* Neuroimage, 2015. **104**: p. 1-20.

344. Kurtek, S., et al., *Elastic geodesic paths in shape space of parameterized surfaces.* IEEE Trans Pattern Anal Mach Intell, 2012. **34**(9): p. 1717-1730.

345. Hibar, D.P., et al., *Common genetic variants influence human subcortical brain structures.* Nature, 2015. **520**(7546): p. 224-229.

346. Bonnotte, N., *From Knothe's Rearrangement to Brenier's Optimal Transport Map.* SIAM J. Math. Anal., 2013. **45**(1): p. 64-87.

347. Haker, S., et al., *Optimal Mass Transport for Registration and Warping.* International Journal of Computer Vision, 2004. **60**(3): p. 225-240.

348. Rehman, T.u., et al., *3D nonrigid registration via optimal mass transport on the GPU.* Med Image Anal, 2009. **13**(6): p. 931-940.

349. Zhu, L., S. Haker, and A. Tannenbaum, *Area-Preserving Mappings for the Visualization of Medical Structures*, in *Medical Image Computing and Computer-Assisted Intervention*. 2003. p. 277-284.

350. Su, Z., et al., *Area Preserving Brain Mapping*, in *IEEE Conference on Computer Vision and Pattern Recognition (CVPR)*. 2013. p. 2235-2242.

351. Grenander, U. and M.I. Miller, *Computational anatomy: an emerging discipline.* Q. Appl. Math., 1998. **LVI**(4): p. 617-694.

352. Miller, M.I., A. Trouve, and L. Younes, *On the metrics and euler-lagrange equations of computational anatomy.* Annu Rev Biomed Eng, 2002. **4**: p. 375-405.

353. Younes, L., *Shapes and Diffeomorphisms*. 2010: Springer.

354. Srivastava, A., et al., *Statistical shape analysis: clustering, learning, and testing.* IEEE Transactions on Pattern Analysis and Machine Intelligence, 2005. **27**(4): p. 590-602.

355. Srivastava, A. and I.H. Jermyn, *Looking for Shapes in Two-Dimensional Cluttered Point Clouds.* IEEE Transactions on Pattern Analysis and Machine Intelligence, 2009. **31**(9): p. 1616-1629.

356. Bauer, M., P. Harms, and P.W. Michor, *Almost local metrics on shape space of hypersurfaces in n-space.* Siam Journal on Imaging Sciences, 2012. **5**(1): p. 244-310.

357. Kurtek, S., et al., *Landmark-Guided Elastic Shape Analysis of Spherically-Parameterized Surfaces.* Computer Graphics Forum, 2013. **32**(2): p. 429-438.

358. Jermyn, I.H., et al., *Elastic Shape Matching of Parameterized Surfaces Using Square Root Normal Fields*, in *12th European Conference on Computer Vision*. 2012. p. 804-817.

359. Lipman, Y. and I. Daubechies, *Conformal Wasserstein distances: Comparing surfaces in polynomial time.* Advances in Mathematics, 2011. **227**(3): p. 1047-1077.

360. Lipman, Y., J. PuenteIngrid, and Daubechies, *Conformal Wasserstein distance: II. computational aspects and extensions.* Math. Comput., 2013. **82**: p. 331-381.

361. Mémoli, F., *Gromov–Wasserstein Distances and the Metric Approach to Object Matching.* Foundations of Computational Mathematics, 2011. **11**(4): p. 417-487.

362. Schoen, R. and S.-T. Yau, *Lectures on Harmonic Maps*. 1997: International Press.

363. Villani, C., *Topics in Optimal Transportation*. 2003: American Mathematical Society.

364. Edelsbrunner, H., *Algorithms in Combinatorial Geometry*. 1987: Springer-Verlag Berlin Heidelberg.

365. Peyré, G. and L.D. Cohen, *Geodesic Remeshing Using Front Propagation.* International Journal of Computer Vision, 2006. **69**(1): p. 145-156.

366. Essa, I.A. and A.P. Pentland, *Coding, analysis, interpretation, and recognition of facial expressions* IEEE Transactions on Pattern Analysis and Machine Intelligence, 1997. **19**(7): p. 757-763.

367. Jack, C.R., Jr., et al., *The Alzheimer's disease neuroimaging initiative (ADNI): MRI methods.* Journal of Magnetic Resonance Imaging, 2008. **27**(4): p. 685-691.

368. Raz, N., et al., *Regional brain changes in aging healthy adults: general trends, individual differences and modifiers.* Cereb Cortex, 2005. **15**(11): p. 1676-1689.

369. Apostolova, L.G., et al., *Hippocampal and ventricular changes in Parkinson's disease mild cognitive impairment.* Neurobiol Aging, 2012. **33**(9): p. 2113-2124.

APPENDIX A

DERIVATION OF EQ. 2.5

With conformal parameterization, the Riemann metric is defined as:

$$[g_{ij}] = \begin{bmatrix} g_{11} & g_{12} \\ g_{21} & g_{22} \end{bmatrix} = \begin{bmatrix} \lambda & 0 \\ 0 & \lambda \end{bmatrix}$$

The inverse of $[g_{ij}]$ is:

$$[g^{ij}] = \begin{bmatrix} g^{11} & g^{12} \\ g^{21} & g^{22} \end{bmatrix} = \begin{bmatrix} 1/\lambda & 0 \\ 0 & 1/\lambda \end{bmatrix}$$

The differential operators that appear in Eq. 2.4 are expressed in general coordinates as [141, 142].

Gradient:

$$\nabla_S \varphi = g^{ij} \frac{\partial \varphi}{\partial x_j} = g^{i1} \frac{\partial \varphi}{\partial x_1} + g^{i2} \frac{\partial \varphi}{\partial x_2} = \begin{bmatrix} g^{11} \frac{\partial \varphi}{\partial x_1} + g^{12} \frac{\partial \varphi}{\partial x_2} \\ g^{21} \frac{\partial \varphi}{\partial x_1} + g^{22} \frac{\partial \varphi}{\partial x_2} \end{bmatrix}$$

Thus the gradient operator ∇_S can be written as:

$$\nabla_S = \begin{bmatrix} g^{11} \frac{\partial}{\partial x_1} + g^{12} \frac{\partial}{\partial x_2} \\ g^{21} \frac{\partial}{\partial x_1} + g^{22} \frac{\partial}{\partial x_2} \end{bmatrix}$$

Divergence:

$$\nabla_S \cdot u = \frac{1}{\sqrt{g}} \frac{\partial}{\partial x_i} \left(\sqrt{g} u_i \right) = \frac{1}{\sqrt{g}} \left(\frac{\partial}{\partial x_1} \left(\sqrt{g} u_1 \right) + \frac{\partial}{\partial x_2} \left(\sqrt{g} u_2 \right) \right)$$

where $u = \begin{bmatrix} u_1 \\ u_2 \end{bmatrix}$ and $\sqrt{g} = \sqrt{\det([g_{ij}])} = \sqrt{g_{11} g_{22} - g_{12} g_{21}}$.

The Laplacian can be computed by gradient and divergence as:

$$\Delta_S \varphi = \nabla_S \cdot (\nabla_S \varphi)$$

$$= \frac{1}{\sqrt{g}} \left(\frac{\partial}{\partial x_1} \left(\sqrt{g} g^{11} \frac{\partial \varphi}{\partial x_1} + \sqrt{g} g^{12} \frac{\partial \varphi}{\partial x_2} \right) + \frac{\partial}{\partial x_2} \left(\sqrt{g} g^{21} \frac{\partial \varphi}{\partial x_1} + \sqrt{g} g^{22} \frac{\partial \varphi}{\partial x_2} \right) \right)$$

Given conformal parameterization $\phi: S \rightarrow \mathbb{R}^2$, where $\sqrt{g} = \lambda, g^{11} = g^{22} = \frac{1}{\lambda}, g^{12} = g^{21} = 0$, we have

$$\Delta_S v = \frac{1}{\lambda} \Delta v$$

For a velocity field $v = \begin{bmatrix} v_1 \\ v_2 \end{bmatrix}$, $\nabla_S(\nabla_S \cdot v) = \nabla\left(g^{11} \frac{\partial v_1}{\partial x_1} + g^{12} \frac{\partial v_1}{\partial x_2} + g^{21} \frac{\partial v_2}{\partial x_1} + g^{22} \frac{\partial v_2}{\partial x_2}\right) = \frac{1}{\lambda} \nabla(\nabla \cdot v)$.

APPENDIX B

EXPERIMENTAL DETAILS WITH SPHARM

In details, three commands from SPHARM system were used in sequence:

(1) SegPostProcess: This command can be used to extract a single label or a label range from the input image, to resample the input image into isotropic resolution, and to ensure the spherical topology of the substructure represented by the image label. Styner et al. [161] claimed that the input to next command, GenParaMesh has to be of isotropic resolution and a relatively fine resolution is preferred and suggested an isotropic resolution of $0.5mm \times 0.5mm \times 0.5mm$ for hippocampi. However, in the experiment, if we resample the binary images obtained by FIRST with the command SegPostProcess, about 20% of the subjects will fail the following processing. As a result, before running the command, the binary images were resampled into an isotropic resolution of $1mm \times 1mm \times 1mm$ with the linear registration given by FLIRT. Thus, in the comparison experiment, the SegPostProcess command was used as a format conversion tool, i.e., to convert the binary analyze images into a format that can be read by the subsequent commands. The command was run by the following example command line on each isotropic image:

```
SegPostProcess Label.hdr –o Label_PP.hdr –label 1
```

where Label.hdr is the input and Label_PP.hdr is the output.

(2) GenParaMesh: This command extracts the surface of the input label segmentation and maps the surface to a sphere with the area-preserving, distortion-minimizing spherical mapping [161]. The command was run by the following example command line:

```
GenParaMesh Label_PP.hdr –iter 1000 –label 1
```

This command will output two surfaces: Label_PP_surf.meta is the surface and Label_PP_para.meta is the spherical parameterization.

(3) ParaToSPHARMMesh: This command computes the SPHARM-PDM representation and resolves issues of correspondence and alignment. The command was run by the following example command line:

```
ParaToSPHARMMesh Label_PP_surf.meta Label_PP_para.meta –subdivLevel 10 –
spharmDegree 12     –flipTemplate template.coef –regTemplate template.meta
```

The parameters subdivLevel and spharmDegree were set as recommended for hippocampus [161]. The flip template was chosen as the same template with the inverse consistent fluid registration and was computed by the above command without providing a flip template. The output of the command will be registered surfaces.